DESIGN OF NEW MG-BASED GLASS-FORMING COMPOSITIONS USING LIQUIDUS TEMPERATURE CALCULATIONS CORRELATED WITH AN ELASTIC STRAIN MODEL

by

ADAM GITTINS

A thesis submitted to

The University of Birmingham

for the degree of

MRes in the Science and Engineering of Materials

School of Metallurgy and Materials

University of Birmingham

Edgbaston

Birmingham B15 2TT

May 2011

SYNOPSIS

New Mg-based glass-forming compositions have been designed based upon the convergence of two existing predictive models; (1) a liquidus model developed by Cheney and Vecchio, and (2) an elastic strain model proposed by Miracle and Senkov. According to these models, alloys compositionally located near a deep eutectic, while simultaneously containing a topology that induces significant elastic strain in a developing crystalline lattice, exhibit experimentally good glass-forming ability. In light of this, the Mg-Cu-Y (MCY), Mg-Cu-Zn (MCZ) and Mg-Zn-Sm (MZS) systems were investigated as it appeared that these systems have optimised values for both liquidus profiles and elastic strains across broad compositional ranges. Three additional mathematical criteria used to evaluate other factors thought to influence glass-forming ability including concentration dependence, reduced melting temperature, and the electronegativity difference for these systems have also been examined.

A combination of scanning electron microscopy and X-ray diffractometry were used to investigate the microstructure of as-cast rapidly solidified alloys. Differential scanning calorimetry and hardness testing were used to investigate the thermal behaviour and mechanical properties of the alloys, respectively.

Of the rapidly solidified alloys, $Mg_{60}Cu_{22}Y_{18}$ was considered to have the best glass-forming ability. This alloy demonstrated values of 0.54, 42 and 0.39 for the reduced glass transition temperature, T_{rg}, undercooled liquid region, ΔT_x, and γ-parameter, respectively. However; the ability of the Mg-based alloys to form a glass on rapid solidification from the melt could not be accurately predicted by the convergence of the two existing models. Despite some alloys displaying values in excess of those stated in the literature over which good glass-formers are found, experimental results have suggested that the microstructures for these alloys are fully crystalline, indicating weakness in the models' glass-forming predictability. In contrast, it was concluded by experimental evidence that the additional mathematical criteria provide support, albeit small, for their application when seeking to design glass-forming compositions. Other observations revealed that the hardness properties of the ternary

crystalline MCY, MCZ and MZS alloys exceed those of wrought Mg alloys indicating a possibility for subsequent development of crystalline glassy alloys, which can be used for a wide range of applications.

ACKNOWLEDGEMENTS

In particular, I wish to express my sincere gratitude to Dr. Isaac Chang for his enthusiastic and patient supervision throughout the project. Encouragement, guidance and most of all invaluable ideas and criticism are gratefully acknowledged.

I would like to extend my gratitude to the following technical staff for their invaluable assistance: Mr. Jeff Sutton; Mr. John Lane; Mr. Frank Biddlestone; Mr. Jaswinder Singh; and all the staff of the Centre for Electron Microscopy. Additionally, I would like to thank my colleague Dr. Peter Squire for extremely valuable aid and insights.

Finally, I would like to thank my family for their full understanding, support and encouragement when most required.

TABLE OF CONTENTS

CHAPTER 1 INTRODUCTION

1.1 Introduction

Metallic amorphous materials have attracted extensive interest since the pioneering work done by Duwez at the end of the 1960s. This is because they exhibit many unique properties that are not shared by the corresponding crystalline solids, e.g. good soft magnetic properties (Fe-based amorphous alloys), good resistance to corrosion (e.g. Fe-Cr and Ni-P amorphous alloys) and good mechanical properties, such as those shown in Figure 1.1. These unique properties are due to the liquid-like atomic structure in the solid state of amorphous alloys, i.e. there is no long range order (periodicity) characteristic in the arrangement of atoms in metallic amorphous solid.

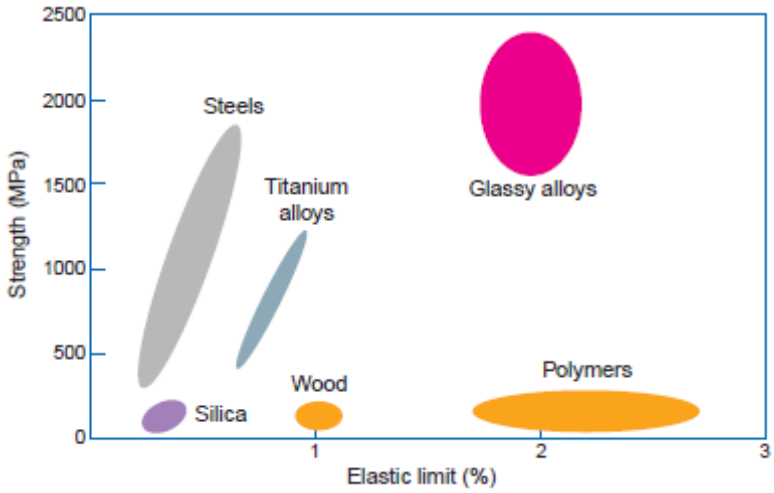

Figure 1.1 Amorphous metallic alloys combine higher strength than crystalline metal alloys with the elasticity of polymers [1].

A variety of industries including defence, electronic, aerospace, and medical are becoming increasingly aware of the benefits that can be obtained through using metallic amorphous materials. In particular, properties such as excellent low frequency damping, superior hardness and strength, increased elastic limits, and the ability to cast very complex and unique designs are very appealing for sporting applications. Sporting equipment such as golf club heads, tennis rackets, bicycle frames, and baseball and softball bats constructed from amorphous metal alloys (as

shown in Fig. 1.2) have the potential to achieve increased measurable performance compared with existing materials due to their superior mechanical properties.

Figure 1.2 Baseball bat featuring Liquidmetal Technologies 'Pure Energy Transfer' technology based on Vitreloy [1].

Traditionally, the liquid-like atomic structure can be obtained by rapidly quenching the molten alloy from the melting point to room temperature at a sufficiently high cooling rate so that the crystallisation can be completely suppressed during the solidification. However, traditional amorphous alloys made by rapid solidification processes have relatively small glass-forming ability (GFA) and thus a high cooling rate (e.g. $>10^3$ Ks^{-1}) is required to retain the non-crystalline structure after quenching from their melts.

Since the early 1990s, a series of Zr-based multicomponent amorphous alloys with large supercooled liquid regions have been developed by Zhang et al [2] and Johnson et al [3] by quenching the melt into a water cooled copper mould at cooling rates of 1-10 K/min. Recently, there have been extensive research activities on the alloy development of amorphous Mg-based multicomponent alloy systems [4]. Since Mg-based bulk metallic glass (BMG) was reported [5], it has attracted considerable attention due to its low density and elastic modulus, superior wear and corrosion resistance, and high specific strength. Furthermore, new compositions of Mg-based BMG have been reported to have unusual oxygen resistance during the preparation process, and to be a very potential candidate for a hydrogen-storage material [6]. However, finding optimum or new alloy compositions with high GFA is still a challenge, which relies on the tedious work of repeated melting/casting and thermal analysis of numerous alloy compositions. Therefore, finding a new model for predicting the alloy compositions with a greater tendency for glass formation would be beneficial for the development of new alloy systems.

1.2 Objective of the thesis

In light of the above, the research programme will concentrate on developing a combinatorial modelling approach which will be used to design a range of ternary Mg-based metallic glasses. A liquidus model, developed by Cheney and Vecchio [7], which determines and ranks the presence of deep eutectics, will be used to determine the optimal compositional region. This criterion will then be correlated with an elastic strain model proposed by Miracle and Senkov [8]. Alloys compositionally located near a deep eutectic, while simultaneously containing a topology that induces significant elastic strain in a developing crystalline lattice, exhibit experimentally good glass forming ability. Three additional mathematical criteria used to evaluate other factors thought to influence glass-forming ability including solute concentration dependence, reduced melting temperature, and the electronegativity difference for these systems have also been examined.

Based on a range of Mg-based alloy systems being developed, the Mg-Cu-Y ternary system will be investigated. This particular system has been extensively researched allowing an in-depth analysis of the correlation between theory and experiment. Subsequently, the Mg-Cu-Zn and Mg-Zn-Sm systems will be investigated as these systems have optimised values for both liquidus profiles and elastic strains across broad compositional ranges. These values were determined using equations 2.4 and 2.5 in Chapter 2, and are listed in tables 4.2 and 4.3 in Chapter 4, respectively. In addition, by replacing rare earth metals with transition metals, the cost of producing the alloy is reduced. Comparisons will then be drawn with experimental results on the same alloys. The alloys will be prepared through a combination of arc-melting, induction melting and various casting methods. The alloys will then be studied using a combination of SEM, XRD, DSC and hardness tests to characterise the microstructure, composition, crystallisation behaviour and mechanical properties of the Mg-based BMG alloys.

The ultimate goal is to have the ability to design bulk metallic glasses, before experimentation, with a known or significant understanding of the dimensions in which they can be produced with an amorphous structure.

References

[1] M. Telford, Materials Today, 3(2004)36

[2] T. Zhang, A. Inoue, and T. Masumoto, Mater. Trans., JIM, 32(1991)1005

[3] W. L. Johnson and A. Peker, Appl. Phys. Lett., 63(1993)2342

[4] Q. Zheng, S. Cheng, J. H. Strader, E. Ma, and J. Xu, Scrip. Mater., 56(2007)161

[5] A. Inoue, K. Ohtera, K. Kita, and T. Masumoto, Jpn. J. Appl. Phys., 27(1988)2248

[6] Y. X. Wei, X. K. Xi, D. Q. Zhao, M. X. Pan, and W. H. Pan, Mater. Lett., 59(2005)945

[7] J. Cheney and K. Vecchio, Mater. Sci. Eng., A471(2007)135

[8] D. B. Miracle and O. N. Senkov, Meter. Sci. Eng., A347(2003)50

CHAPTER 2 LITERATURE REVIEW

2.1 Metallic glasses

A glass is a solid in a disordered (or amorphous) state lacking the long-range periodicity present in a typical crystal. Due to continuous refinement of grains being possible, the boundary between a fully amorphous and a nanocrystalline solid is becoming indistinct. Therefore, if no long-range order can be determined at a 1 nm scale, solids have been referred to as a glass for practical purposes [1]. Traditional glasses (that is SiO_2) are commonly recognised as liquids, which form glasses easily [2, 3], which are generally covalently bonded. However, glasses exist with other types of bonding: metallic, ionic (e.g. KNO3-Ca(NO3)2), hydrogen (aqueous solutions, H2O) and van der Waals (glycerol). The current project focuses on glasses, which contain metallic bonding, and hence are metallic glasses.

2.1.1 Development of bulk amorphous alloys

Since the first success of preparing a metallic glass in the Au-Si system through the process of rapid quenching from its melt in 1960 [4], metallic glasses have been the subject of an increasing research effort, spurred by both science and technology. In 1969, Chen and Turnbull [5] formed amorphous spheres of ternary Pd-Cu-Si with a diameter of 0.5 mm, enabling the first detailed studies of crystallisation in metallic glasses. In the early 1980s, Kui et al [6] produced glassy ingots of $Pd_{40}Ni_{40}P_{20}$ with a diameter of 5 mm using surface etching followed by heating and cooling cycles. By processing in a boron oxide flux, they increased the critical casting thickness to 1 cm – the first BMG. An overview of critical casting thickness and the date of discovery is shown in Figure 2.1.

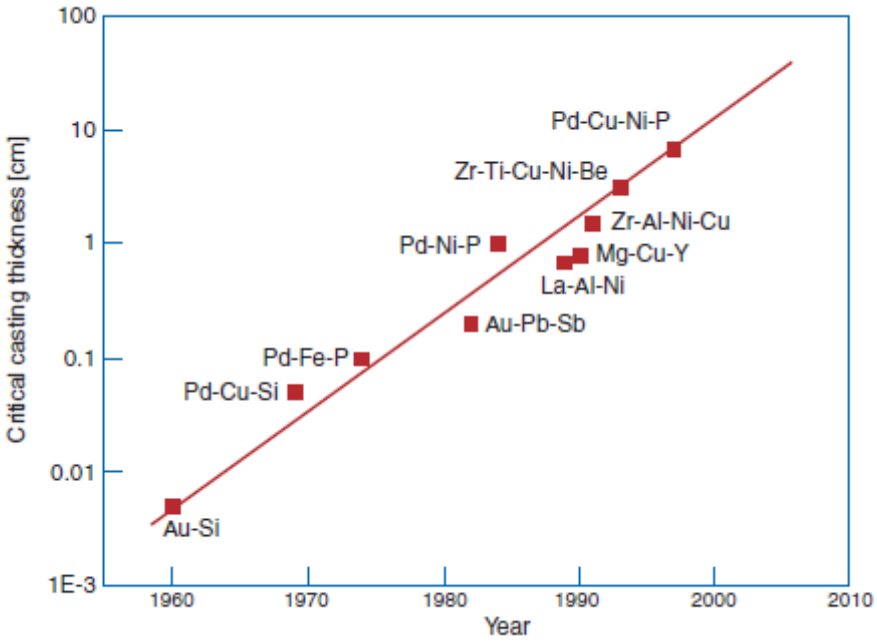

Figure 2.1 The critical casting thickness versus the year in which alloys were discovered [7].

Since the 1980s, there has been the discovery of strong glass-forming multi-component La-, Mg-, Zr-, Pd-, Fe-, Cu-, and Ti-based alloys with large undercooling and low critical cooling rates of 1 °C s^{-1} to 100 °C s^{-1}, similar to oxide glasses. These properties allow and increase in time (from milliseconds to minutes) before crystallisation, enabling a greater critical casting thickness (>1 cm) by conventional moulding.

In the late 1980s, Inoue discovered that La-Al-Ni is highly glass-forming while investigating the mixing of rare earth materials such as lanthanides with Al and ferrous metals [8]. Using Cu moulds, they cast glassy $La_{55}Al_{25}Ni_{20}$ up to 5 mm thick and, in 1991, glassy $La_{55}Al_{25}Ni_{10}Cu_{10}$ up to 9 mm thick. Mg-Cu-Y was also shown in 1991 to have high glass-forming ability in the form of $Mg_{65}Cu_{25}Y_{10}$ [9]. In 1993, Peker & Johnson [10] developed a pentary alloy $Zr_{41.2}Ti_{13.8}Cu_{12.5}Ni_{10.0}Be_{22.5}$, as part of a US Department of Energy and NASA funded project to develop new aerospace materials. With critical casting thickness of up to 10 cm possible in silica containers, the alloy became known as Vitreloy 1, the first commercial BMG.

2.1.2 Synthesis of metallic glasses

Metallic glasses can be synthesised by a variety of different techniques, which can be classified into three categories:

(1) Sputtering

Sputtering is based on atom-by-atom formation of a film on a substrate in an inert gas atmosphere. $Au_{81}Si_{19}$ has been prepared in its amorphous solid state by sputtering in an argon atmosphere [11]. Sputtering is very sensitive to the preparation conditions such as the purity of the atmosphere. This method results in very high cooling rates (over 10^8 °C s^{-1}), allowing the production of the amorphous phase for relatively poor glass formers such as $Al_{65}Ni_{15}Si_{20}$.

(2) Solid state reaction

Solid state amorphisation techniques are based on a different mechanism involving asymmetrical diffusion of atomic species in solid states. The amorphous phase is formed from solid crystalline elemental mixtures or alloys by methods such as interdiffusion of multilayers or mechanical alloying/milling (MA/MM).

(3) Solidification from the melt

A wide variety of solidification techniques from the melt have been developed such as splat quenching, melt spinning and chill block solidification. Splat quenching was perhaps the earliest melt quenching method, involving cooling liquid droplets of alloy by rapid flattening between two pistons. Very high cooling rates in the order of approximately 5×10^8 °C s^{-1} can be achieved using this method [12]. Melt spinning involves bringing a stream of molten alloy into contact with a rapidly moving substrate surface of high thermal conductivity (generally a rotating copper wheel [13]). The width (~ 3 mm [14]) and thickness (~ 30 μm [14]) of the resulting ribbon remains comparable to samples processed by splat quenching. High cooling rates of 10^6 - 10^8 °C s^{-1} [15] can be achieved using this method.

2.1.2.1 Synthesis of bulk metallic glasses

The production of samples in bulk (minimum dimension at least 1 mm), is limited to a few techniques, such as the consolidation of glassy powders [16] and cooling the alloy from the melt. The former requires the production of amorphous powders by gas atomisation, MA or MM and requires thermal exposure, which could induce crystallisation and is therefore not of interest in the current report apart from crystallisation behaviour. The latter involves quenching the molten alloy at a cooling rate sufficient to suppress crystallisation, which is higher than the critical cooling rate, R_C. R_C determines the maximum thickness of glassy structure that can be cast, which is commonly referred to as the critical casting diameter, D_{max}. Preparation of metallic glasses by cooling from the melt can be achieved by the following techniques:

(1) Water quenching

Water quenching has been successfully applied to several multicomponent metallic glasses, such as Fe- [17], Pd- [18], Y- [19] and Zr-based [20] systems. The cooling rate is dependent on numerous variables such as diameter of the sample, temperature of the melt and water, and material and thickness of container used, but is generally observed in the region of 10 [21] – 1000 [22] °C s^{-1}. In addition to reaction with the crucible, specimen geometries are limited to the shape of the container, which are generally tubular giving rod-shaped amorphous material samples.

(2) Induction melting followed by injection into a mould

A variety of shapes can be produced by induction melting the alloy within a container followed by injection into a mould (generally copper), which may be water-cooled for increased cooling rates. This technique has been used for the production of a variety of bulk metallic glass systems, such as Fe- [23], Pd- [24], Ni- [25], Ti- [26] and Zr-based [27] ones with different specimen geometries, such as rods [26, 27] and plates [28, 29]. Cooling rates obtained during casting depend mainly on the diameter of the rod / dimensions of the plate, but are generally determined as approximately 100 °Cs^{-1} [30, 31].

2.1.3 Mg-based bulk amorphous alloys

For Mg-based alloys, the bulk metallic glass route is certainly an attractive way to overcome one of their major drawbacks, i.e., their relatively low strength compared with common engineering materials such as steels and aluminium alloys. By reaching the amorphous state, one gets rid of dislocations, the carrier for yielding in crystalline alloys. This results in high strength in the low-density Mg alloys. In addition, because the Mg-based alloys have the possibility of high endurance limit against pulverisation due to the small volume expansion during hydrogen absorption, Mg-based BMGs are also potential candidates for hydrogen-storage materials. Furthermore, new compositions of Mg-based BMG have been reported to have unusual oxygen resistance during the preparation process [32], which helps to reduce impurities and consequently assist in achieving high GFA. These qualities, together with their low cost and ability to be recycled, make Mg-based alloys highly desirable for applications. Indeed, since the first Mg-based BMG, $Mg_{65}Cu_{25}Y_{10}$, was fabricated [33] extensive efforts have been devoted to locating Mg-based BMG formers in several multi-component systems [34, 35, and 36].

2.2 Crystallisation of amorphous materials

Amorphous solids are in a thermodynamically unstable state and show a tendency to crystallise to one or more metastable or stable crystalline phases. They generally crystallise by a nucleation and growth process [37] as part of primary, polymorphous or eutectic reactions [38].

2.2.1 Primary

Primary crystallisation is the initial stage of crystallisation of numerous metallic glass alloys such as Al-based [39], Zr-based [40] and Mg-based [41] systems. It is the nucleation and growth of a phase of different composition from that of the glass.

The growth of primary crystals whether they form directly from the liquid or the undercooled liquid may be rate limited by interface or diffusion processes. Interface control limits the rate of transfer of atoms across an advancing interface and diffusion control the rate of diffusion of atoms towards or away from the growing phase. When transfer of atoms across and towards or away from the interface is similar, mixed control can be observed (interface and diffusion). Evidence suggests that primary crystallisation of metallic glasses is mainly diffusion controlled [42].

2.2.2 Polymorphous

Polymorphous crystallisation is characterised by nucleation and growth of crystals of the same composition as the amorphous matrix, which does not require long-range diffusion. Due to bulk metallic glasses being multi-component alloys, an ordered single phase is expected to be complicated. The crystal growth rate is independent of time for polymorphous transformation and crystals grow until hard impingement with other crystals under isothermal conditions.

2.2.3 Eutectic

Eutectic crystallisation is the simultaneous crystallisation of two crystalline phases by a discontinuous reaction. This reaction has no concentration difference across the reaction front, but takes longer than polymorphous crystallisation to proceed because the two components have to separate by diffusion into two separate phases within the crystallised region. The modern phenomenological theory of eutectic crystallisation suggested by A. A. Bochvar [43] is based on the following provisions:

1. Eutectic crystallisation is realised by nucleation and growth of eutectic grains
2. A eutectic grain is a double-phase bicrystal with a complex system of intermittent phase branches
3. Nucleation of eutectic grains is initiated by only one of the partner phases known as the base phase
4. Eutectic crystallisation begins from the moment of contact between crystals of both phases; the phase contact occurs either due to nucleation of one phase on (near) the surface of the other or due to inoculating the second phase of the eutectic on a crystal of the base phase
5. Formation of a eutectic grain on the appearing bicrystal base occurs by joint cooperative growth of the eutectic partners, the most important feature of which is dendritic branching of both phases.

2.3 Deformation behaviour of BMGs and mechanical properties

Mechanisms dominating deformation in crystalline solids are temperature dependent. At low temperatures relative to the melting point, slip and twinning dominate deformation. Slip involves a translational shift of an atomic layer relative to another, where the crystallographic orientation is the same either side of the slip place before and after deformation. There is, however, a reorientation across the twin plane. At intermediate and high temperatures, close to the melting point of crystalline solids, other mechanisms become increasingly important. These mechanisms include stress-directed atomic diffusion, diffusion-controlled movement of dislocations or grain boundary sliding. High temperature deformation mechanisms all depend on atom or ion diffusion. Grain size, shape and crystallographic texture all influence the mechanical response of materials to applied stress. The microstructure of an alloy hence dominates its deformation behaviour.

2.3.1 Microscopic deformation mechanisms in metallic glasses

Atomic bonds in the metallic glass can be broken and reform easily compared to covalent or ionic solids due to the rigidity of angles or balance of charges in the latter two respectively. Compared to dislocation movement in crystalline solids, rearrangement of atoms in the metallic glass is a high-energy and hence high-stress process. This is reflected by their high yield stress compared to their crystalline counterparts. The exact nature of this atomic rearrangement process is still not fully understood. However, there is a general consensus that deformation proceeds via local rearrangement of atoms to accommodate applied strain. Two complementary viewpoints (by Spaepen [44] and Argon [45]) of the mechanism of rearrangement of atoms have been developed, where plastic flow is favoured at locations containing more free volume. Free volume is defined as the excess volume compared to an ideal disordered atomic configuration of maximum density [46]. The “free volume model” was originally developed by Cohen and Turnbull [47] showing a relation between diffusion and a minimum volume of a void required for atomic movement in liquids and glasses. Changes in free volume of the local structure are widely accepted to account for deformation in metallic glasses [48].

Spaepen [44] developed a model, where the macroscopic flow occurs by individual atomic jumps, by applying Cohen and Turnbull's "free-volume" model to the deformation of glasses using free volume as the order parameter. Spaepen's model involves monatomic systems and does not explicitly include chemical effects. A nearest neighbour environment, as shown in Figure 2.2, is required for this process, which is the basic microscopic mechanism for diffusion. An activation barrier must be overcome for this movement to take place. If no external force is supplied, the atomic movement takes place in both directions without any net movement of atoms. The application of an external force results in atomic movement being biased in the direction of the force. This results in a net flux of atoms and achieves metal flow. The alternative viewpoint proposed by Argon [45] considers plastic deformation to occur via formation of shear transformation zones (STZs), where a cluster of atoms experiences a shear distortion from one low-energy position to another, passing a location of elevated energy (activation energy), as shown in Figure 2.3. STZs should not be mistaken for a dislocation or a structural defect. It is a region formed by a transient process occurring over a short time period. A sample having deformed by shear transformation would not show the presence of STZs, as they are not a structural feature. Local energetics of the atomic arrangements will identify locations for STZs to occur. Locations of a higher free volume would be expected to accommodate local shear transformation more readily.

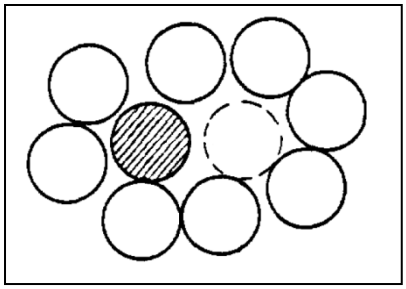

Figure 2.2 Schematic diagram of mechanism proposed by Spaepen of an individual atomic jump, the basic step for macroscopic diffusion and flow [44]

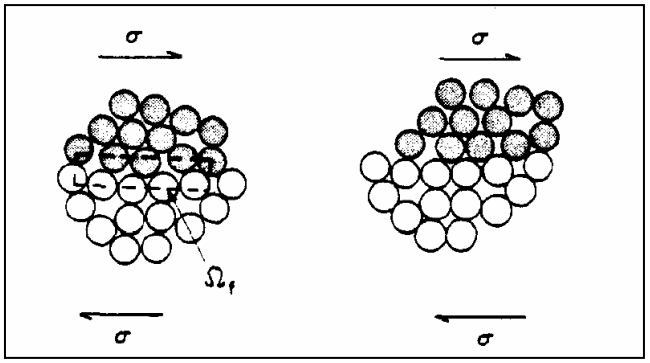

Figure 2.3 Shear transformation zone (STZ) in a metallic glass after Argon, where Ω_f is a volume consisting of a free volume site and its immediate surroundings [45]

2.3.2 Mechanical properties of Mg-based bulk amorphous alloys

The search for an amorphous alloy with both high glass-forming ability and good mechanical properties is of great importance in the research field of amorphous metallic materials. The high glass-forming ability enables us to prepare bulk glassy alloys by copper mould casting and the good mechanical properties are essential for final application as structural materials. Mg-based bulk metallic glasses are regarded as a new family of promising materials with excellent specific strength and good corrosion resistance in contrast to the Mg-based crystalline alloys, due to the different atomic configuration [49]. For example, $Mg_{65}Cu_{20}Zn_5Y_{10}$ [50] and $Mg_{65}Cu_{15}Ag_5Pd_5Y_{10}$ [51] BMG alloys exhibit compressive strengths of ~650 and ~800 MPa, respectively, which are more than twice that of ordinary crystalline Mg alloys. The excellent GFA and high strength of Mg-based BMG alloys, together with their low density, make the Mg-based BMG alloys particularly attractive for engineering applications such as weight reduction and higher fuel efficiency transportation [52].

Like other BMG alloys, Mg-based BMGs have also been found to be brittle due to their inhomogeneous deformation behaviour. They always fracture in the elastic regime without observable plastic deformation. It was reported that the notched fracture toughness, K_C, of Mg-based BMG is even as low as 2.0 MPa$\sqrt{m}$, which

approaches that of ideal brittle silicate glasses [53, 54, 55]. Therefore, the absence of distinct plasticity in Mg-based BMG alloys has become one of the challenging problems for their engineering application.

In the efforts to overcome the brittleness of BMG alloys, the preparation of BMG matrix composites by using in situ methods has been proven to be an effective way. The reinforcing phases in BMG matrix composite are expected to hinder the propagation of shear bands and promote the formation of multiple shear bands, hence retarding the emergence of catastrophic failure in BMG matrix. In this subject, the first discovered reinforcement is the ductile crystalline Ti–Zr–Nb β phase, which is formed in situ in Zr–Ti–Nb–Cu–Ni–Be bulk metallic glass matrix and results in a dramatic increase of plastic strain of ~5% in the composite [56]. To date, in situ BMG matrix composites have been prepared in Zr–Nb–Ti–Cu–Ni–Be [57], Zr–Al–Ni–Cu–Nb [58], Zr–Cu–Ni–Al–Ta [59], Cu–Zr–Ti–Ta [60], La–Al–Ni–Cu [61], Pd–Ni–Cu–P [62] and Ti–Cu–Sn–Ta [63] BMG or nanostructured matrix alloys. All of the above composites have exhibited distinct plasticity ranging from 5% to 14.5% at room temperature. However, for Mg-based BMG alloys, ideal reinforcement has not been found until recently. Ma et al. [64] synthesised $Mg_{65}Cu_{7.5}Ni_{7.5}Zn_5Ag_5Y_{10}$ BMG matrix in situ composites containing iron as second phase dispersions. The macroscopic plasticity of the composite with a 13 vol. % fraction of iron particles is only about 1%, although the fracture strength is increased to 990 MPa. The plastic strains to failure of Mg-based composites with ex situ TiB_2 particles [65] were found to reach the order of 2–3%. The reason why the Mg-based BMG composites fail to exhibit distinct plasticity may be attributed to their intrinsic brittleness and the unapt selection of the second phase.

A long-period order structure (LOS) has been found in $Mg_{91}Y_8Zn_1$ and $Mg_{88}Y_8Zn_4$ alloys processed by non-equilibrium synthesis or the cast method [66]. It has been proven that these alloys exhibit maximum tensile yield strength of 600 MPa and elongation of 5%. So it is expected that the LOS may improve the plasticity and strength of the BMG alloy if the LOS is uniformly dispersed in the amorphous matrix. To date, however, no work has been reported to introduce the LOS into the glass matrix of Mg-based BMG alloys.

2.4 Glass-forming ability

Glass-forming ability (GFA) is very crucial for understanding the origins of glass formation and also important for designing and developing new bulk metallic glasses (BMGs). The glass-forming ability of a melt is evaluated in terms of the critical cooling rate (Rc) for glass formation, which is the minimum cooling rate necessary to keep the melt amorphous without precipitation of any crystals during solidification. The smaller Rc, the higher the GFA of a system should be. However, Rc is a parameter that is difficult to measure precisely. A great deal of effort has therefore been devoted to searching for a simple and reliable gauge for quantifying GFA for metallic glasses.

2.4.1 Empirical rules for achieving bulk amorphous alloys

Early methodology for alloy design was created by Inoue [67] who stated in order to achieve a high GFA for metallic alloys, the following three empirical rules should be satisfied; glass-forming alloys must: (1) have a negative mixing enthalpy among constituent elements, (2) contain large atomic size mismatches, and (3) be a multi-component alloy of three or more elements. These rules have been applied to several sets of alloy systems, those based upon Mg, Al, Ti, Fe, Ni, Cu, and Zr, to validate their effectiveness. Table 2.1 lists the more successful compositions, in terms of glass-forming ability and the maximum producible thickness, D_{max}, described in the literature.

Base	Composition	D_{max}	Ref.
Al	$Al_{87}Ni_7Gd_6$	300 μm	[68]
	$Al_{87}Fe_7Gd_6$	20 μm	[68]
	$(Al_{75}Cu_{17}Mg_8)_{97}Ni_3$	50 μm	[69]
	$Al_{87}Ni_6FeGd_6$	250 μm	[70]
Cu	$Cu_{60}Hf_{25}Ti_{15}$	4 mm	[71]
	$Cu_{60}Zr_{30}Ti_{10}$	4 mm	[71]
Fe	$Fe_{48}Cr_{15}Mo_{14}Er_2C_{15}B_6$	12 mm	[72]
	$Fe_{50}Mn_{10}Mo_{14}Cr_4C_{16}B_6$	4 mm	[73]
	$Fe_{61}Y_2Zr_8Co_7Mo_7B_{15}$	5 mm	[74]
Mg	$Mg_{65}Cu_{25}Gd_{10}$	8 mm	[75]
	$Mg_{60}Cu_{30}Y_{10}$	2.5 mm	[76]
Ni	$Ni_{59.35}Nb_{3.4}Sn_{6.2}$	3 mm	[77]
	$Ni_{59}Zr_{16}Ti_{13}Si_2Sn_3Nb_7$	5 mm	[77]
Ti	$Ti_{50}Ni_{15}Cu_{32}Sn_3$	1 mm	[78]
	$Ti_{50}Ni_{15}Cu_{25}Sn_3Be_7$	2 mm	[78]
	$Ti_{40}Zr_{25}Ni_8Cu_9Be_{18}$	8 mm	[78]
Zr	$Zr_{41.2}Ti_{13.8}Cu_{12.5}Ni_{10}Be_{22.5}$	14 mm	[79]
	$Zr_{65}Al_{7.5}Ni_{10}Cu_{17.5}$	16 mm	[80]

Table 2.1 Critical diameters for reported glass-forming alloys of Al-, Cu-, Fe-, Mg-, Ni-, Ti-, and Zr-based compositions.

The rules for glass formation were expanded by Egami [81] who added that an attractive force between large and small sized elements coupled with repulsion between the smallest elements increases the GFA. These modelling techniques have the capability to produce glass formation ranges, the range of compositions in which glass formation is likely to occur. However, precise compositional optimisation within a proposed alloy system is difficult, increasingly so as the number of alloying elements increases.

2.4.2 GFA parameters

Several researchers have deduced some simple parameters to reflect the relative GFA for various systems. Among them, the most famous is the reduced glass transition temperature

$$T_{rg} = T_g/T_l \quad \text{(Eq. 2.1)}$$

where T_g and T_l are the glass transition temperature and the liquidus temperature, respectively, proposed by Turnbull based on the assumption that the nucleation frequency of a melt scales as $1/\eta$ (η, viscosity of the liquid) [82]. However, it was found that in many BMGs [83], T_{rg} cannot reflect the GFA effectively.

An additional empirical parameter has been developed to estimate GFA. Based on the results of thermal analysis such as differential scanning calorimetry (DSC), one can study the undercooled liquid region

$$\Delta T_x = T_x - T_g \quad \text{(Eq. 2.2)}$$

where T_x and T_g are the onset temperature of crystallisation and the glass transition temperature, respectively. The larger the supercooled liquid region, the larger the GFA and thus the lower the critical cooling rate.

More recently, a criterion, denoted as γ, has been proposed to assess GFA with considerations for both liquid phase stability and resistance to crystallisation [84], which can be expressed as

$$\gamma = T_x / (T_g + T_l) \quad \text{(Eq. 2.3)}$$

where T_x, T_g and T_l are the onset temperature of crystallisation, the glass transition temperature and the liquidus temperature, respectively. Experimental work has demonstrated that the γ parameter is a good universal indicator of GFA in various alloy systems. Figure 2.1 shows the correlation between γ and the critical cooling rate, a direct measure of GFA, for 53 metallic glasses. As can be seen from Figure 2.4, the regression coefficient R^2 value reaches as high as 0.92, indicating a strong interrelationship between γ and GFA for metallic glasses. In particular, Nascimento et al [85] investigated the accuracy of most representative GFA parameters in

stoichiometric glass-forming oxides and demonstrated that the γ parameter showed the best correlation with GFA.

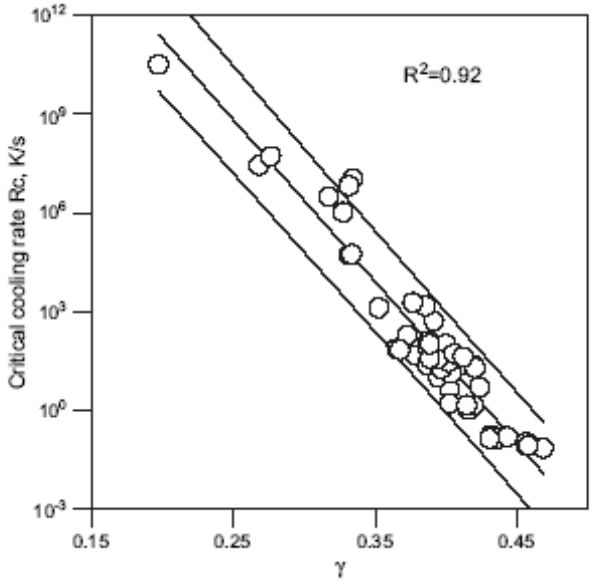

Figure 2.4 Correlation between γ and the critical cooling rates for 53 multi-component metallic glasses [84]

2.4.3 Factors influencing GFA

There are several factors that influence GFA. These factors are summarised here:

(1) Alloy compositions

It has been accepted that deep eutectics are thermodynamically favourable for glass formation for rapidly quenched alloys. The reasons are twofold. Firstly, the free energy difference G^l-G^s between the glass state or undercooled melts and the competitive crystalline phases is minimal. This implies that only small driving forces exist for the crystallisation of the equilibrium phases. Secondly, at the eutectic composition, the crystallisation process requires sharp, local composition changes and long range diffusion, both of which favour glass formation.

(2) Electronegativity difference between the alloying elements

Large electronegativity differences between the elements in a given alloy system are frequently related to strongly negative values for the enthalpy of mixing. This has a tendency to lower the eutectic temperatures. Hence, this causes an increase in T_{rg} suggesting a large GFA for rapidly quenched alloys.

(3) Atomic radii difference

Glass formation is favourable when the atomic radii difference between elements in a given alloy is more than 12% [86]. The large difference in atomic radii hinders the crystallisation kinetics by reducing the diffusion of elements in the liquid alloys. In the crystalline state, the substitution of a smaller atom with a larger atom expands the lattice. If the concentration of the substitute element is high enough, the lattice will become unstable, and such a crystal becomes unstable thermodynamically and cannot form during solidification. Hence, alloying elements with very different atomic size tend to destabilise the crystalline phase. Egami and Johnson [87] have proposed that alloying is not to stabilise the liquid state by chemical interaction but to destabilise the crystalline state by the size effect.

(4) Number of alloying components

It has been found that the GFA can be significantly extended by the addition of other elements into the currently developed ternary or quaternary amorphous alloys, known as multicomponent amorphous alloys. The choice of other components must satisfy the above-mentioned rules, i.e. the large atomic difference and large negative heat of mixing between the alloying and solvent elements. This has been described as the "confusion principle" as proposed by Greer [88], i.e. as the number of components in a liquid alloy is increased, crystallisation becomes confused or frustrated.

2.5 Predicting GFA

So far, the effect of alloy compositions on the crystallisation behaviour of amorphous phase for a certain multicomponent bulk amorphous alloy system requires further detailed investigation. Usually, the three empirical rules (i.e. large negative heat of mixing, atomic size difference and the number of components) have been applied to give an explanation of the crystallisation behaviour. However, what is the optimised atomic size difference required to construct a highly dense random packed amorphous structure? Inoue et al have deduced experimentally that the optimised atomic size ratio is between 12 and 21% [89]. Neither too small size ratios nor too big size ratios can construct a highly dense random packed atomic structure. Furthermore, Inoue et al have concluded that a significantly positive or extremely large negative heat of mixing can prevent the formation of a highly dense random packed structure with a homogeneous mixed atomic configuration. The non-uniform atomic configuration enables easy nucleation and the growth of a crystalline phase from the supercooled liquid. Therefore, there is a need for the three empirical rules to be quantified via computerised, predictive modelling.

2.5.1 The elastic strain criterion

A quantitative method to evaluate the GFA of large numbers of possible alloy combinations in a systematic and comprehensive manner has been developed. Miracle & Senkov [90] proposed a topological model which has shown that atomic size mismatches can generate elastic strains, which hinder crystallisation. The model is based on the concept described by Egami and Waseda [91], that a crystalline lattice becomes unstable once the internal strain reaches a critical value required for the local coordination number (the number of nearest neighbour atoms) to change to the nearest integer value. It is suggested in this model that the internal strain is produced by solute elements that can occupy both interstitial and substitutional sites of the reference solvent crystal lattice, and it is the sum of the strains ε_s and ε_i induced by the solute atoms in substitutional and interstitial sites, respectively. Although this model was derived for binary alloys systems, it can also be applied to multicomponent systems to verify if the composition provides a mean local strain, which is sufficient

to destabilise the crystal lattice. The mean local strain on the lattice atom in a system with n alloying elements is

$$\varepsilon_A^V = \frac{\sum_{j=1}^{n} Cj\gamma j\xi[X_{sj}(R_j^3 - 1) + X_{ij}(R_j^3 - \eta^3)]}{1 + \sum_{j=1}^{n} C_j X_{sj}(R_j^3 - 1)} \qquad \text{(Eq. 2.4)}$$

where the subscript *j* denotes a *j*th alloying element, *C* is the atomic concentration of the solute atoms, γ is close to 1 if the bulk moduli of the solute and host elements are only slightly different, ξ is the coefficient of compaction of the crystalline lattice, X_s and X_i are the fractions of the solute atoms in either substitutional or interstitial sites of the host matrix, *R* is the reduced radius, and η is the volume of an interstitial site in the matrix.

The values of ε_A^V calculated for different amorphous metallic alloys using the model developed by Miracle & Senkov are shown in Table 2.2. The elastic strain criterion states that the mean local strain must exceed 0.054 in order to destabilise the crystal lattice formation and encourage amorphisation. This value is derived from the density difference between the crystalline and amorphous states. It can be seen that for all Zr-based bulk metallic glass formers, as well as for an Mg-based alloy, the model gives positive values of ε_A^V exceeding the critical local strain $\varepsilon_{cr} = 0.054$, indicating a remarkable correlation with ease of glass formation. On the other hand, Table 2.1 also shows that the model does not work well for Al-based alloys as the volume strain ε_A^V is lower than the critical strain and in some cases it is negative. However, the low strain values predicted by the Miracle & Senkov's model for these alloys can be explained by the fact that the radii used to calculate the internal strains may not be correct.

Alloy Composition	Strain, ε
$Zr_{41.2}Ti_{13.8}Cu_{12.5}Ni_{10}Be_{22.5}$ (Vit 1)	0.094
$Zr_{47}Ti_{8}Cu_{7.5}Ni_{10}Be_{27.5}$ (Vit 4)	0.097
$Zr_{52.5}Ti_{5}Al_{10}Cu_{17.9}Ni_{14.6}$ (Vit 105)	0.073
$Zr_{57}Nb_{5}Al_{10}Cu_{15.4}Ni_{12.6}$ (Vit 106)	0.057
$Mg_{70}Ni_{20}Y_{10}$	0.087
$Al_{85}Y_{10}Fe_{5}$	0.056
$Al_{87}Y_{8}Ni_{5}$	0.043
$Al_{70}Fe_{20}Zr_{10}$	-0.022
$Al_{70}Cu_{20}Hf_{10}$	-0.019

Table 2.2 The mean local strain per lattice atom in selected metallic glass alloys [90]

2.5.2 The α-parameter criterion

The first metallic glasses were binary alloys formed along the eutectic compositions [92], and it is known that metal alloys can form glasses along eutectic compositions with relative success. Consequently, several theoretical predictions have been made examining binary phase diagrams [93] in order to produce binary metallic glasses along deep eutectics, or for use in extrapolating binary information for ternary alloy design. Experimental studies have verified that the compositional location of eutectics and good glass-forming alloys is similar, and calculating liquidus temperature profiles with the aim of searching for eutectics has been successfully used to produce novel glass-forming alloys [94]. Since solidification is initiated at much lower temperatures at a eutectic composition, crystallisation must fight against a more viscous environment of low atomic mobility, which effectively reduces the crystallisation rate, in terms of both nucleation and growth. Thus, a second quantitative method for predetermining metallic glass-forming ability has been proposed using a well known occurrence among metallic glasses, their compositional location along deep eutectics.

A parameter developed by Cheney & Vecchio [95], termed α, is a measure of the depth of a eutectic as related to a weighted liquidus temperature. The α parameter is expressed as:

$$\alpha = \frac{\sum_{i=1}^{n} x_i T_i}{T_l} \qquad \text{(Eq. 2.5)}$$

The weighted liquidus temperature is the numerator, where x_i is the atomic fraction of element i, T_i is the melting temperature of element i, and n is the number of elements in the alloy. A eutectic will generate an α value greater than 1, with deeper eutectics producing larger α values. Comparisons of this theory and experimental results given in literature from varied sources and alloy types show that compositions containing relatively high α values correspond to successfully produced bulk metallic glasses. Specifically, an α parameter value in excess of 1 suggests a slight tendency for glass formation, whiles α values greater than 1.5 suggests a very strong tendency. Thus, the α parameter can serve as a tool for quantifying potential bulk metallic glass alloys in terms of limiting their requirement for rapid quenching.

Table 2.3 presents the calculated α parameter of the best glass-forming composition reported in the literature. As shown, the alloys which are good glass-formers over a large composition range have α parameter values above or near 1.5. The aluminium based and Fe-Zr-B system glasses, which are relatively poor glass formers, have lower α values at around 1. In the case of alloy systems where a large range of compositions reside in a deep eutectic, such as the Zr-Ni-Al, La-Ni-Al, and Mg-Cu-Y systems, the model is only marginally accurate in pinpointing the optimum composition. However, in alloys where only the eutectic is compositionally narrow, the model is more accurate.

Alloy	α	D_{max} (mm)
$La_{55}Ni_{25}Al_{20}$	2.34	3
$Zr_{55}Ni_{25}Al_{20}$	1.75	3
$Ca_{54}Mg_{18}Cu_{28}$	1.71	1
$Zr_{66}Al_9Cu_{16}Ni_9$	1.57	16
$Mg_{65}Cu_{25}Y_{10}$	1.52	7
$Ca_{59.5}Mg_{16.5}Zn_{24}$	1.49	1
$Fe_{48}Cr_{15}Mo_{10}Er_2C_{15}B_6$	1.48	12
$Nd_{55}Fe_{20}Al_{10}Y_{15}$	1.18	2
$Fe_{85}Zr_7B_8$	1.15	0.02
$Al_{87}Ni_7Gd_6$	1.02	0.03
$Al_{87}Ni_5Y_8$	0.84	0.03

Table 2.3 Alloys ranked according to α parameter and maximum producible thickness, D_{max} [95].

2.5.3 The λ_n criterion

Glass formation is always a competing process between the supercooled melt and crystalline phases. As previously stated, large atomic radii differences confines the solubility of the constituent elements in the competing crystalline phases. Upon cooling, these elements have to be redistributed during the crystallisation process, which retards the nucleation process and, in turn, promotes glass formation, hence leading to an increase in glass-forming ability. In addition, large atomic radii differences in an alloy system can support a new supercooled liquid structure [96]. The new atomic configurations tighten the packed structure of the undercooled liquid and increase the packing density, which lowers the energy of the undercooled liquid and thus stabilises the supercooled liquid, leading to enhanced glass-forming ability. However, there does exist an optimum atomic size ratio/distribution in a given alloy system as far as glass formation is concerned. Therefore, a λ_n criterion has been defined to comprehensively evaluate solute concentration dependence of glass-forming ability of alloys in a system [97]. It is suggested that a glass structure with $\lambda_n \approx 0.18$ has optimum solute concentration for multicomponent systems. For a multicomponent metallic glass consisting of *n* constituent elements, the λ_n criterion is defined as

$$\lambda_n = \sum_{i=2}^{n} C_i \left[1 - \left(\frac{ri}{r1} \right)^3 \right] \qquad \text{(Eq. 2.6)}$$

where *ri* and *r*l are solvent and solute atom radius, respectively, and C_i (in atomic percent) is the solute concentration of element B.

2.5.4 Reduced melting temperature

As mentioned above, the glass-forming ability is not always enhanced with the increase in atomic radii differences among constituent elements. Excessive difference in atomic size may relax the high randomly packed structure of the undercooled liquid. However, if the relative size factor is favourable, other factors should be

considered in deciding the probable degree of glass-forming ability. Liu et al. [98] have introduced another parameter, the reduced melting temperature, T_{rm}.

$$T_{rm} = \sum_{i=1}^{n} C_i \left[1 - \frac{T_{mi}}{\overline{T}_m} \right] \qquad \overline{T}_m = \sum_{i=1}^{n} C_i T_{mi} \qquad \text{(Eq. 2.7)}$$

T_{rm} represents the fractional departure of T_{mi} from the simple rule of mixtures melting temperature T_m. C_i and T_{mi} are the mole fraction and melting point, respectively, of the ith component of an n-component alloy system.

2.5.5 Electronegativity difference and atomic size parameter

It is evident that ΔT_x can be effectively used to indicate glass-forming ability for some bulk metallic glass systems. According to experimental data found within the literature, ΔT_x has a strong correlation with two bond parameters [98]. In detail, ΔT_x increases with the increase of electronegativity difference (Δx) and the atomic size parameter (δ). These parameters are defined as

$$\Delta x = \sqrt{\sum_{i=1}^{n} C_i (x_i - \overline{x})^2} \qquad \overline{x} = \sum_{i=1}^{n} C_i x_i \qquad \text{(Eq. 2.8)}$$

$$\delta = \sqrt{\sum_{i=1}^{n} Ci \left(1 - \frac{ri}{\overline{r}}\right)^2}, \quad \overline{r} = \sum_{i=1}^{n} C_i r_i \qquad \text{(Eq. 2.9)}$$

where n is the number of components in the alloy system; C_i , x_i and r_i are the atomic percentage, Pauling electronegativity and covalent atomic radius of element i, respectively.

References

[1] X. Donghua, "Development of novel binary and multi-component bulk metallic glasses," in Division of Engineering and Applied Science Pasadena: California Institute of Technology, 2005.

[2] J. F. Loffler, Intermetallics, 11(2003)529

[3] W. H. Wang, C. Dong, and C. H. Shek, Materials Science and Engineering, 44(2004)45

[4] H. W. Klement, R. H. Willens, and P. Duwez, Nature, 187(1960)869

[5] H. S. Chen and D. Turnbull, Acta Matall., 17(1969)1021

[6] H. W. Kui, Appl. Phys. Lett., 45(1984)615

[7] M. Telford, Materials Today, 3(2004)36

[8] A. Inoue, Mater. Trans., JIM, 30(1989)965

[9] A. Inoue, Mater. Trans., JIM, 32(1991)609

[10] A. Peker and W L. Johnson, Appl. Phys. Lett., 63(1993)2342

[11] A. Schlegel, P. Wachter, K. P. Ackermann, M. Liard, and H. J. Guntherodt, Solid State Communications, 31(1979)373

[12] H. A. Davies and J. B. Hull, Scripta Metallurgica, 6(1972)241

[13] Z. Altounian, R. J. Shank, and J. O. Strom-Olsen, Journal of Applied Physics, 58(1985)1192

[14] S. O. Park, J. C. Lee, Y. C. Kim, E. Fleury, D. S. Sung, and D. H. Kim, Materials Science and Engineering: A, 449(2007)561

[15] M. H. Phan and H.X. Peng, Progress in Materials Science, 53(2008)323

[16] H. Kato, Y. Kawamura, A. Inoue, and T. Masumoto, Materials Science and Engineering a-Structural Materials Properties Microstructure and Processing, 22(1997)458

[17] C. Zhang and K. Yao, Journal of University of Science and Technology Beijing, Mineral, Metallurgy, Material, 14(2007)68

[18] N. Chen, K.F. Yao, F. Ruan, and Y.Q. Yang, Materials Science and Engineering: A, 473(2008)274

[19] G. Faqiang, S. J. Poon, and J. S. Gary, Applied Physics Letters, 83(2003)2575

[20] P. S. Frankwicz, S. Ram, and H. J. Fecht, Materials Letters, 28(1996)77

[21] M. K. Miller, Materials Science and Engineering A, 250(1998)133

[22] J. H. Kim, J. S. Park, H. T. Jeong, W. T. Kim, and D. H. Kim, Materials Science and Engineering A, 386(2004)186

[23] V. Ponnambalam, S. J. Poon, J. S. Gary, M. K. Veerle, R. Taylor, and G. Petculescu, Applied Physics Letters, 83(2003)1131.

[24] A. Inoue and N. Nishiyama, Materials Science and Engineering A, 226(1997)401

[25] H. Choi-Yim, D. H. Xu, and W. L. Johnson, Applied Physics Letters, 82(2003)1030

[26] Y. C. Kim, W. T. Kim, and D. H. Kim, Materials Science and Engineering A - Structural Materials Properties Microstructure and Processing, 375(2004)127

[27] V. R. Raju, U. Kuhn, U. Wolff, F. Schneider, J. Eckert, R. Reiche, and A. Gebert, Materials Letters, 57(2002)173

[28] C. C. Aydiner, E. Ustundag, M. B. Prime, and A. Peker, Journal of Non-Crystalline Solids, 316(2003)82

[29] S. Kagao, Y. Kawamura, and Y. Ohno, Materials Science and Engineering A, 375(2004)312

[30] Z. W. Zhu, H. F. Zhang, W. S. Sun, B. Z. Ding, and Z. Q. Hu, Scripta Materialia, 54(2006)1145

[31] D. S. Song, J. H. Kim, E. Fleury, W. T. Kim, and D. H. Kim, Journal of Alloys and Compounds, 389(2005)159

[32] F. Xu, Y. Du, P. Gao, Z. Han, G. Chen, S. Wang, and J. Jiang, Journal of Alloys and Compounds, 441(2007)76-80

[33] A. Inoue, Mater. Trans., JIM, 31(1991)425

[34] H. Men, Z. Q. Hu, and J. Xu, Scripta Materialia, 46(2002)699

[35] H. Ma, E. Ma, and J. Xu, Journal of Material Research, 18(2003)2288

[36] G. Yuan, T. Zhang, and A. Inoue, Mat. Trans., 44(2003)2271

[37] U. Koster and P. Weiss, Journal of Non-Crystalline Solids, 17(1975)359

[38] S. Banerjee, R. T. Savalia, and G. K. Dey, Materials Science and Engineering A, 304(2001)26

[39] N. Tian, M. Ohnuma, and K. Hono, Scripta Materialia, 53(2005)681

[40] H. R. Wang, Y. L. Gao, G.-H. Min, X. D. Hui, and Y.-F. Ye, Physics Letters A, 314(2003)81

[41] F. Xu, Y. Du, P. Gao, Z. Han, G. Chen, S. Wang, and J. Jiang, Journal of Alloys and Compounds, 441(2007)76

[42] M. G. Scott and F. E. Luborsky, Amorphous Metallic Alloys - Crystallisation: Butterworth Co & Ltd, 1983.

[43] V. I. Mazur and Y. N. Taran, Metal Science and Heat Treatment, 44(2002)11

[44] F. Spaepen, Acta Metallurgica, 25(1977)407

[45] A. S. Argon, Acta Metallurgica, 27(1979)47

[46] M. Bletry, P. Guyot, J. J. Blandin, and J. L. Soubeyroux, Acta Materialia, 54(2006)1257

[47] M. H. Cohen and D. Turnbull, The Journal of Chemical Physics, 31(1959)1164

[48] M. Bletry, P. Guyot, Y. Brechet, J. J. Blandin, and J. L. Soubeyroux, Materials Science and Engineering A, 387(2004)1005

[49] A. Inoue (Ed.), Bulk Amorphous Alloys, Trans Tech Publication Ltd., Switzerland, 1998.

[50] H. Men, Z. Q. Hu, and J. Xu, Scripta Mater, 46(2002)699

[51] H. Ma, E. Ma, and J. Xu, Journal Mater. Res., 18(2003)2288

[52] P. Aroule. Magnesium Demand and Supply, IMA-55, A Global Vision for Magnesium, Coronado, CA, USA. International Magnesium Association; 1998. p. 36.

[53] X. K. Xi, D. Q. Zhao, M. X. Pan, and W. H. Wang, J Non-cryst Solids 344(2004)189.

[54] P. Lowhaphandu, and J. J. Lewandowski, Scripta Mater, 38(1998)1811

[55] X. K. Xi, D. Q. Zhao, M. X. Pan, W. H. Wang, Y. Wu, and J. J Lewandowski, Phy. Rev. Lett., 94(2005)125510

[56] C. C. Hays, C. P. Kim, and W. L. Johnson, Mater. Sci. Eng., A304–306(2001)650

[57] C. C. Hays, C. P. Kim, and W. L. Johnson, Phys Rev Lett, 84(2000)2901

[58] U. Kuhn, J. Eckert, N. Mattern, and L. Schultz, Appl. Phys. Lett., 80(2002)2478

[59] G. He, Z. F. Zhang, W. Loser, J. Eckert, and L. Schultz, Acta Mater, 51(2003)2383

[60] J. C. Lee, Y. C. Kim, J. P. Ahn, and H. S. Kim, Acta Mater, 53(2005)129

[61] M. L. Lee, Y. Li, and C. A. Schuh, Acta Mater, 52(2004)4121

[62] X. Hu, Y. P. Feng, and Y. Li, Acta Mater, 51(2003)561

[63] G. He, J. Eckert, and L. Schultz, Nat Mater 2(2003)33

[64] H. Ma, J. Xu, and E. Ma, Appl. Phy. Lett., 83(2003)2793

[65] Y. K. Xu, H. Ma, J. Xu, and E. Ma, Acta Mater 53(2005)1857

[66] Y. Kawamura, K. Hayashi, A. Inoue, and T. Masumoto, Mater Trans, 42(2001)1301

[67] A. Inoue, in "Non-equilibrium Processing of Materials", ed. by C. Suryanarayana, Pergamon, 1999, p377

[68] F. Q. Guo, S. J. Poon, G. J. Shiflet, Scripta Mater., 43(2000)1089

[69] F. Q. Guo, S. J. Enouf, S. J. Poon, Philos. Mag. Lett., 81(2001)203

[70]Y. He, G. M. Dougherty, G. J. Shiflet, et al., Acta Metall. Mater., 41(1993)337

[71] A. Inoue, W. Zhang, T. Zhang, et al., Acta Mater., 49(2001)2645

[72] V. Ponnambalam, S. J. Poon, G. J. Shiflet, J. Mater. Res., 19(2004)1320

[73] V. Ponnambalam, S. J. Poon, G. J. Shiflet, et al., Appl. Phys. Lett., 83(2003)1131

[74] Z. P. Lu, C. T. Liu,W. D. Porter, Appl. Phys. Lett., 83(2003)2581

[75] G. Yuan, A. Inoue, J. Alloys Compd., 387(2005)134

[76] N. H. Pryds, Mater. Sci. Eng., A 375–377(2004)186

[77] M. H. Lee, J. Y. Lee, D. H. Bae, et al., Intermetallics, 12(2004)1133

[78] Y. C. Kim,W. T. Kim, D. H. Kim, Mater. Sci. Eng., A 375–377(2004)127

[79] A. Peker,W. L. Johnson, Appl. Phys. Lett., 63(1993)2342

[80] A. Inoue, T. Zhang, N. Nishiyama, et al., Mater. Trans. JIM, 34(1993)1234

[81] T. Egami and Y. Waseda, Journal of Non-crystalline Solids, 64(2003)113

[82] D. Turnbull, Contemp. Phys., 10(1969)473

[83] Z. P. Lu, and C. T. Liu, Acta. Mater., 50(2002)3501

[84] Z. P. Lu, and C. T. Liu, Phys. Rev. Lett., 11(2003)

[85] M. L. F. Nascimento, L. A. Souza, E. B. Ferreira, and E. D. Zanotto, Journal of Non-Crystalline Solids, 40(2005)3296

[86] A. Inoue, T. Zhang, T. Itoi, and A. Takeuchi, Mat. Trans., JIM, 38(1997)359

[87] T. Egami and W. L. Johnson, in “elements of rapid solidification, fundamentals and applications”, ed. By Monde A. Otooni, Springer-Verlag Berlin Heidelberg, 1998,

[88] A. L. Greer, Nature, 366(1993)303

[89] A. Inoue, C. Fan. And T. Masumoto, Mater. Trans., JIM, 36(1995)1411

[90] D. B. Miracle and O. N. Senkov, Mater. Sci. Eng., A347(2003)50

[91] T. Egami and Y. Waseda, Journal of Non-Crystalline Solids, 64(1984)113

[92] H. W. Klement, R. H. Willens, and P. Duwez, Nature, 187(1960)869

[93] M. Marcus and D. Turnbull, Materials Science, 23(1976)211

[94] H. Ma, L. Shi, J. Xu, Y. Li, and E. Ma, Appl. Phys. Lett., 87(2005)

[95] J. Cheney and K. Vecchio, Mater. Sci. Eng., A471(2007)135

[96] Z. P. Lu, C. T. Liu, Y. D. Dong, J. Non-Cryst. Solids, 341(2004)93

[97] Z. J. Yan, J. F. Li, S. R. He, Y. H. Zhou, Materials Research Bulletin, 38(2003)681

[98] W. Y. Liu, H. F. Zhang, A. M. Wang, H. Li, Z. Q. Hu, Materials Science and Engineering A, 459(2007)196-203

CHAPTER 3 EXPERIMENTAL METHODS

3.1 Materials processing

3.1.1 Starting materials

The form, purity and suppliers of the elemental materials used in this project are listed in Table 3.1.

Element	Form	Purity (%)	Supplier
Copper	Shots Ø1-10mm	99.9	Alfa Aesar
Magnesium	Rods Ø35mm	99.99	Sigma-Aldrich
Samarium	Pieces <12mm	99.9	Alfa Aesar
Yttrium	Ingots	99.9	Sigma-Aldrich
Zinc	Sticks Ø6-8mm	99.99	Sigma-Aldrich

Table 3.1 The form, purity (by metal basis) and suppliers of the elements used in making the alloys studied in this project.

The nominal alloy compositions chosen for the present study are listed in Table 3.2. The compositions are stated in atomic percentages.

Identification	Composition (at. %)
MCY1	$Mg_{60}Cu_{22}Y_{18}$
MCY2	$Mg_{60}Cu_{17}Y_{23}$
MCY3	$Mg_{60}Cu_{27}Y_{13}$
MCY4	$Mg_{65}Cu_{22}Y_{13}$
MCY5	$Mg_{55}Cu_{22}Y_{23}$
MCY6	$Mg_{65}Cu_{17}Y_{18}$
MCY7	$Mg_{55}Cu_{27}Y_{18}$
MCZ1	$Mg_{78}Cu_{14}Zn_{8}$
MCZ2	$Mg_{78}Cu_{19}Zn_{3}$
MCZ3	$Mg_{78}Cu_{9}Zn_{13}$
MCZ4	$Mg_{73}Cu_{14}Zn_{13}$
MCZ5	$Mg_{83}Cu_{14}Zn_{3}$
MCZ6	$Mg_{83}Cu_{9}Zn_{8}$

MCZ7	$Mg_{73}Cu_{19}Zn_8$
MZS1	$Mg_{74}Zn_{22}Sm_4$
MZS2	$Mg_{69}Zn_{27}Sm_4$
MZS3	$Mg_{79}Zn_{17}Sm_4$
MZS4	$Mg_{74}Zn_{17}Sm_9$
MZS5	$Mg_{69}Zn_{22}Sm_9$

Table 3.2 A list of given compositions for the alloys studied in this subject.

The first metallic glasses were binary alloys formed along the eutectic compositions [1], and it is well known that metal alloys can form glasses along eutectic compositions with relative success. Consequently, the ternary eutectic alloys for the Mg-Cu-Y, Mg-Cu-Zn, and Mg-Zn-Sm systems will be studied. In addition, experimental studies have verified that alloys have improved glass-forming ability located slightly off-eutectic composition due to competition between the growth of crystalline phases (i.e. eutectic and dendritic phases) and the formation of the amorphous phase [2]. In light of this, alloys located 5 at. % off-eutectic composition will also be studied for all three systems. Ternary phase diagrams of the Mg-Cu-Y, Mg-Cu-Zn, and Mg-Zn-Sm systems indicating equilibrium phases and compositions of the alloys studied in this subject are provided in Figures 3.1, 3.2, and 3.3, respectively.

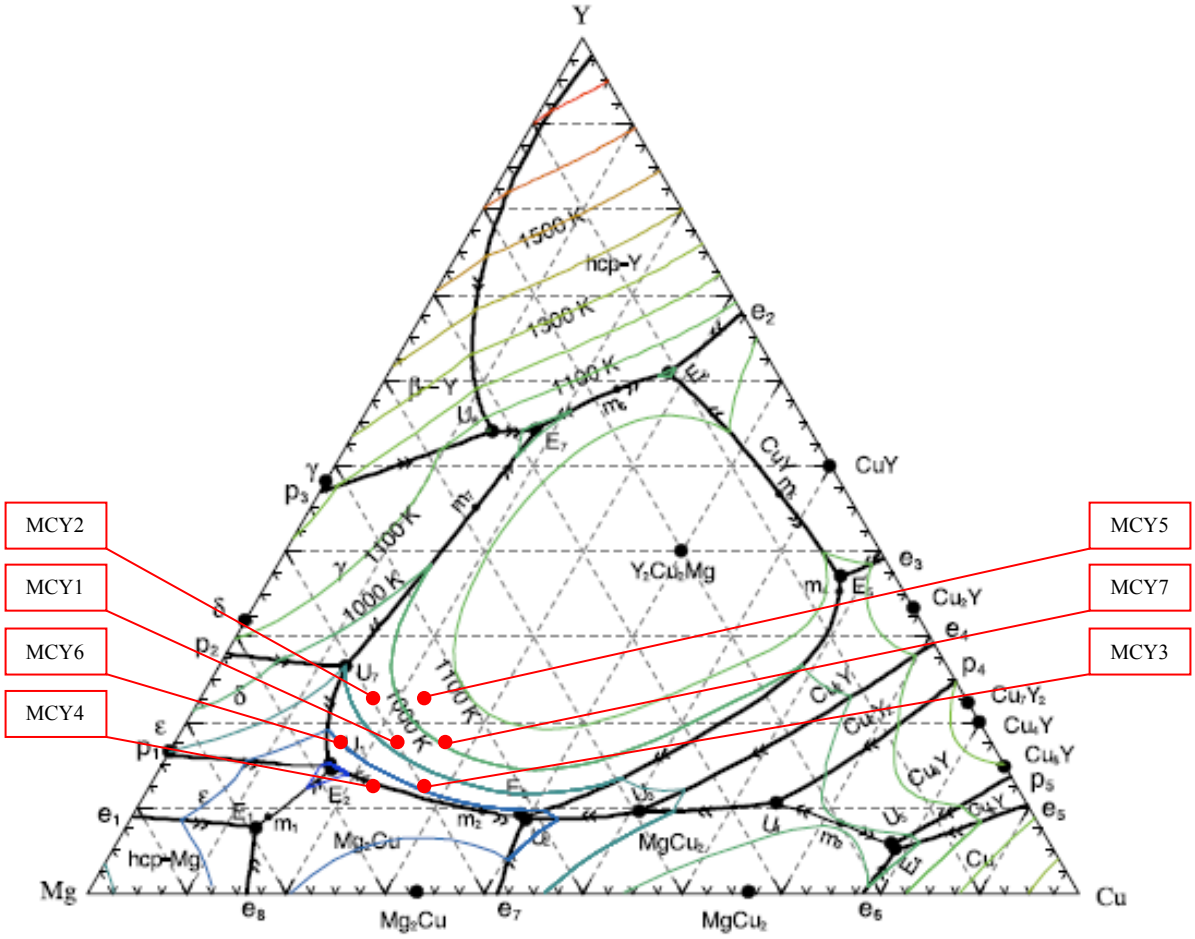

Figure 3.1 Selected Mg-Cu-Y alloys studied in this subject.

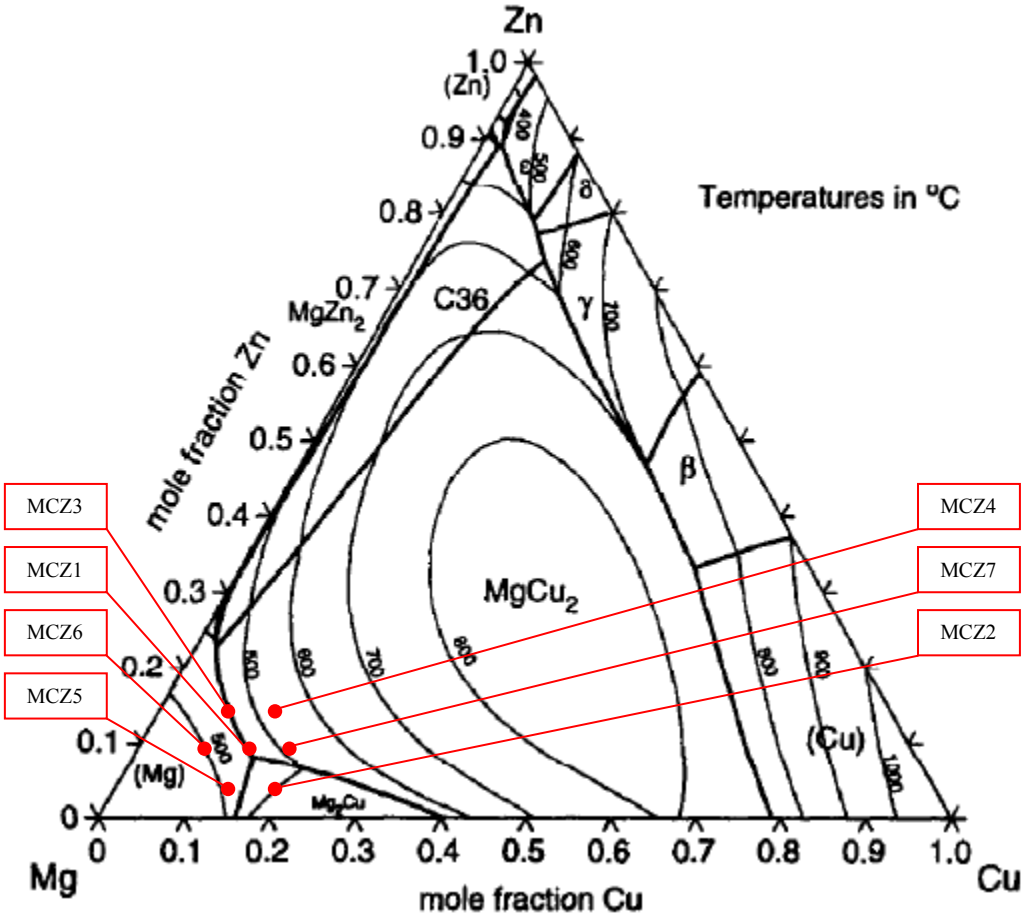

Figure 3.2 Selected Mg-Cu-Zn alloys studied in this subject.

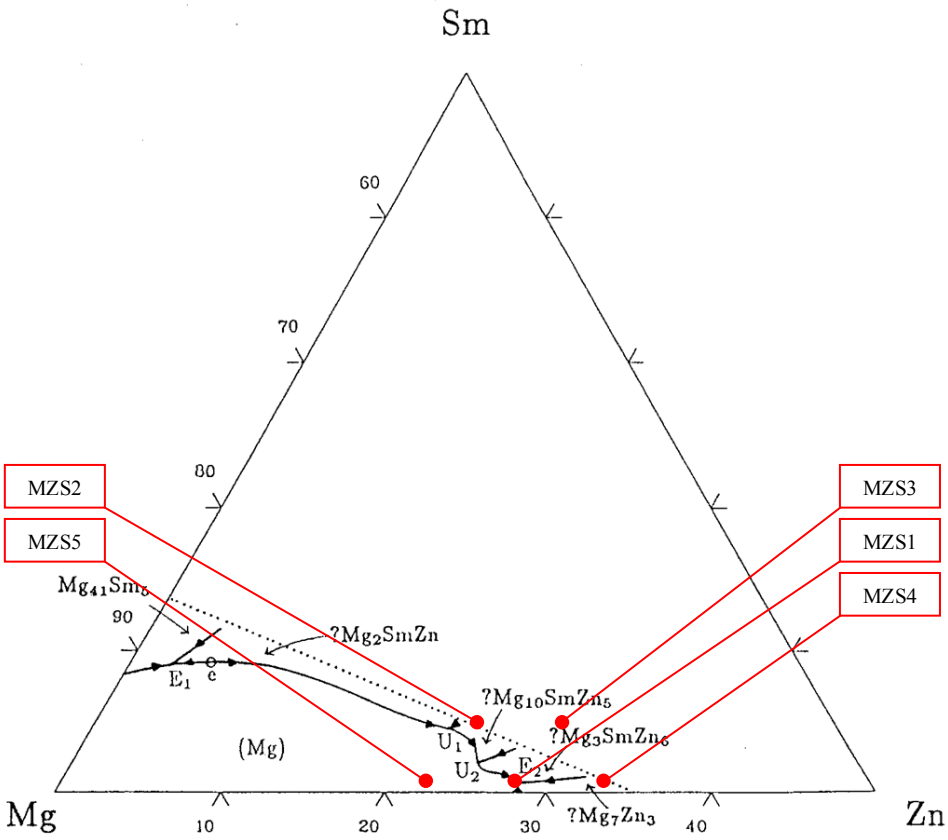

Figure 3.3 Selected Mg-Zn-Sm alloys studied in this subject.

3.1.2 Processing conditions

Table 3.3 indicates the physical properties of Cu, Mg, Sm, Y, and Zn. Since the boiling point of Mg is close to the melting points of Cu and Sm, and lower than the melting point of Y, binary master ingots were first prepared in order to prevent the evaporation of Mg. For the ternary Mg-Cu-Y alloys, $Y_{67}Cu_{33}$ (at. %) master ingots with compositions near to the eutectic reaction shown in Figure 3.4 were first prepared by arc melting under a Ti-gettered argon atmosphere in a water-cooled copper crucible. For the ternary Mg-Cu-Zn alloys, $Mg_{58}Cu_{42}$ (at. %) master ingots, with compositions near to the eutectic reaction shown in Figure 3.5, were prepared by melting appropriate elemental proportions in a tube furnace under inert argon atmosphere. For the ternary Mg-Zn-Sm alloys, $Mg_{92}Sm_8$ and $Mg_{72}Zn_{28}$ (at. %) master ingots, with compositions near to the eutectic reactions shown in Figures 3.6 and 3.7, respectively, were also prepared in a tube furnace under the same conditions.

Element	Boiling Point (°C)	Melting Point (°C)	Vapour Pressure (Pa)
Copper, Cu	2567	1083	0.0505@1083°C
Magnesium, Mg	1090	649	361@649°C
Samarium, Sm	1803	1072	563@1072°C
Yttrium, Y	3338	1526	5.31@1526°C
Zinc, Zn	907	420	19.2@420°C

Table 3.3 Physical properties of Cu, Mg, Sm, Y, and Zn.

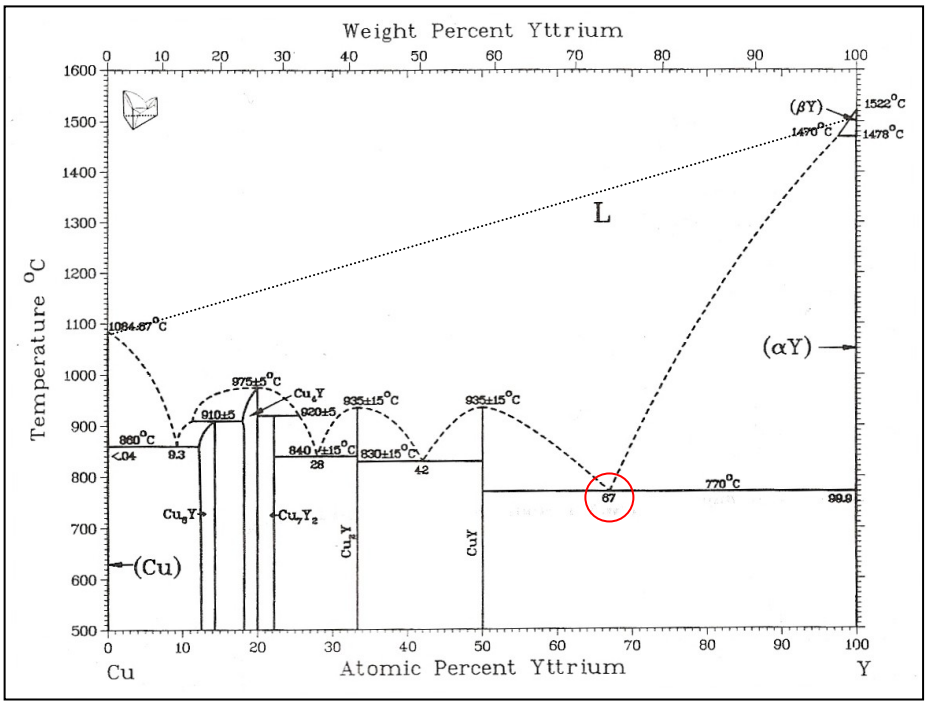

Figure 3.4 Y-Cu phase diagram highlighting eutectic reaction $Y_{67}Cu_{33}$ [3].

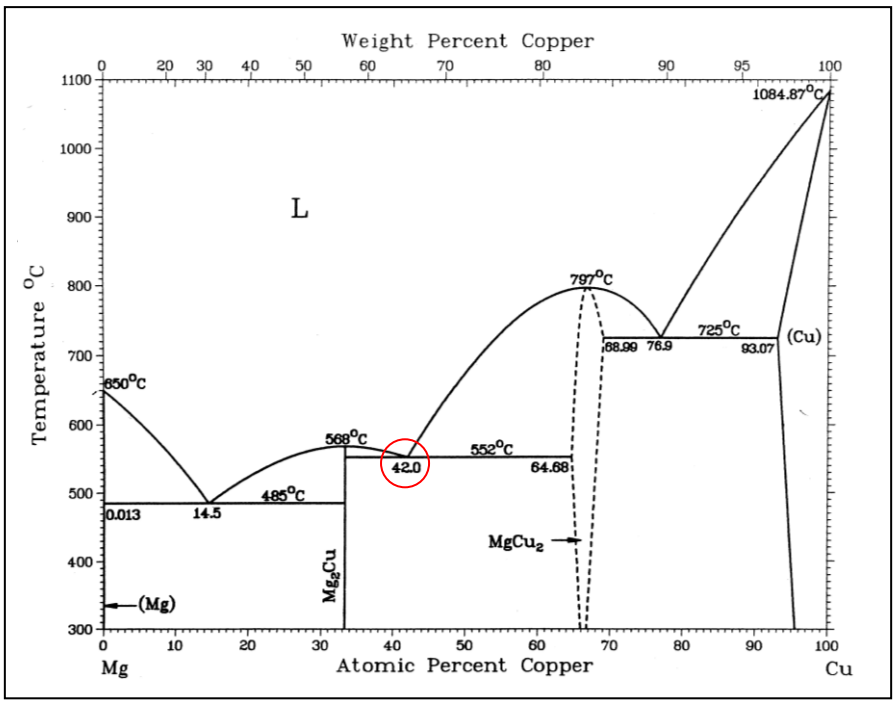

Figure 3.5 Mg-Cu phase diagram highlighting eutectic reaction $Mg_{58}Cu_{42}$ [3].

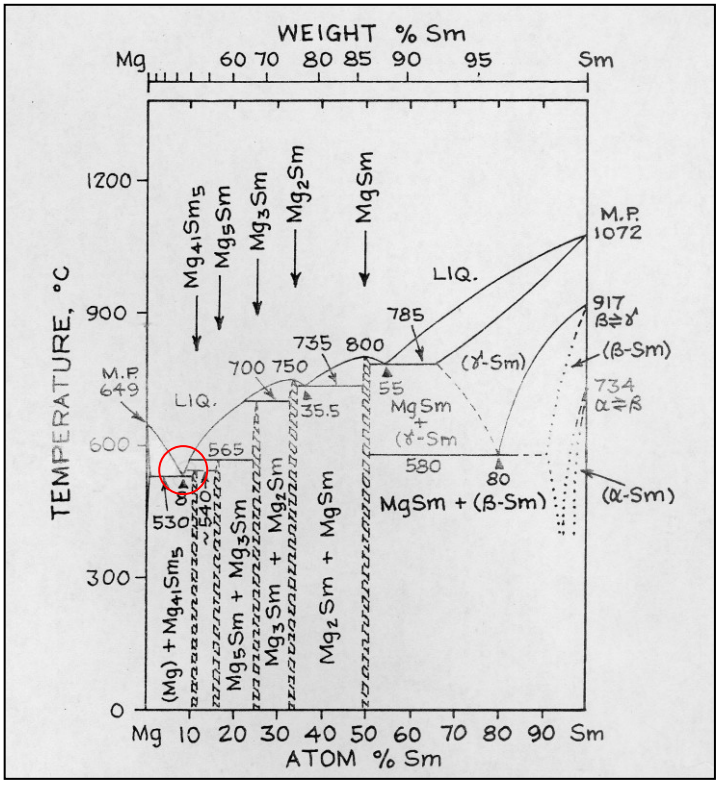

Figure 3.6 Mg-Sm phase diagram highlighting eutectic reaction $Mg_{92}Sm_8$ [3].

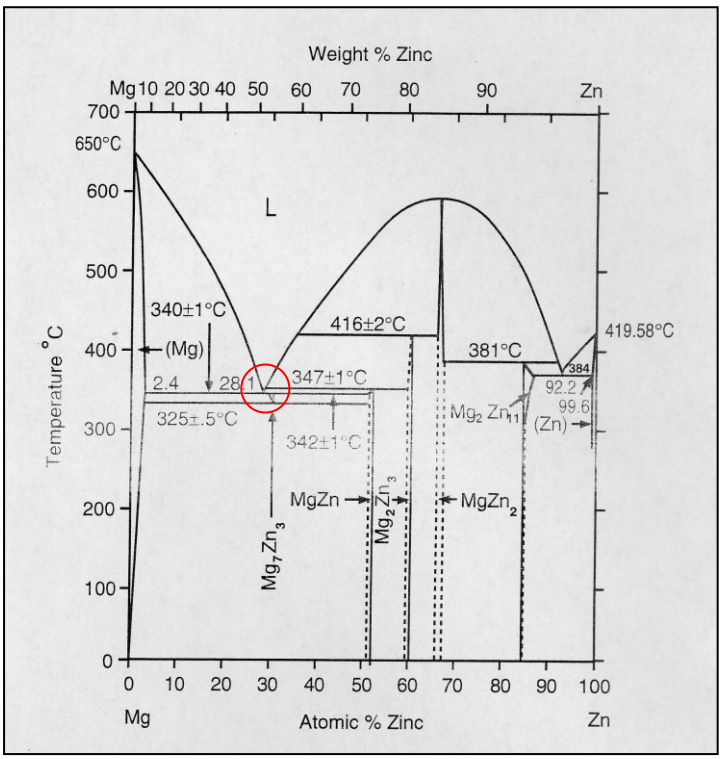

Figure 3.7 Mg-Zn phase diagram highlighting eutectic reaction $Mg_{72}Zn_{28}$ [3].

3.1.2.1 Arc melting

Arc melting was performed by loading the components into a hearth set in a water-cooled copper plate set inside the arc-melting chamber. The chamber was flushed with argon three times. Before melting was initiated, the chamber was evacuated to 8×10^{-2} Torr and then back filled with argon to a pressure of 500mB. A titanium getter was melted for two minutes to minimise the oxygen content remaining. The components were heated using an arc with a 330 amp current at 32 Volts. The resulting ingot was turned and re-melted three times allowing for a more homogenous composition in the ingot. The turning of the ingot was carried out inside the arc-melting chamber, by use of the electrode tip (with the current turned off), when the resulting ingot had cooled to a 'red' heat.

3.1.2.2 Tube furnace

The master ingots were melted several times in a steel boat to ensure compositional homogeneity, and were then re-melted together with appropriate elemental proportions according to Table 3.4 in a tube furnace under inert argon atmosphere in order to obtain final alloys with the desired compositions for the study of GFA and mechanical properties in Mg-based systems.

ID.	Composition (at. %)	$Mg_{58}Cu_{42}$ (g)	$Mg_{92}Sm_8$ (g)	$Mg_{72}Zn_{28}$ (g)	$Y_{67}Cu_{33}$ (g)	Cu (g)	Mg (g)	Sm (g)	Zn (g)	Total (g)
MCY1	$Mg_{60}Cu_{22}Y_{18}$	-	-	-	3.713	2.285	4.002	-	-	10
MCY2	$Mg_{60}Cu_{17}Y_{23}$	-	-	-	4.882	1.004	4.114	-	-	10
MCY3	$Mg_{60}Cu_{27}Y_{13}$	-	-	-	2.622	3.481	3.897	-	-	10
MCY4	$Mg_{65}Cu_{22}Y_{13}$	-	-	-	2.767	2.778	4.455	-	-	10
MCY5	$Mg_{55}Cu_{22}Y_{23}$	-	-	-	4.626	1.801	3.573	-	-	10
MCY6	$Mg_{65}Cu_{17}Y_{18}$	-	-	-	3.925	1.493	4.582	-	-	10
MCY7	$Mg_{55}Cu_{27}Y_{18}$	-	-	-	3.524	2.995	3.481	-	-	10
MCZ1	$Mg_{78}Cu_{14}Zn_8$	4.116	-	-	-	-	4.303	-	1.581	10
MCZ2	$Mg_{78}Cu_{19}Zn_3$	5.598	-	-	-	-	3.807	-	0.595	10
MCZ3	$Mg_{78}Cu_9Zn_{13}$	2.642	-	-	-	-	4.797	-	2.561	10
MCZ4	$Mg_{73}Cu_{14}Zn_{13}$	3.876	-	-	-	-	3.706	-	2.418	10
MCZ5	$Mg_{83}Cu_{14}Zn_3$	4.388	-	-	-	-	4.98	-	0.632	10
MCZ6	$Mg_{83}Cu_9Zn_8$	2.816	-	-	-	-	5.504	-	1.68	10
MCZ7	$Mg_{73}Cu_{19}Zn_8$	5.262	-	-	-	-	3.246	-	1.492	10
MZS1	$Mg_{74}Zn_{22}Sm_4$	-	4.479	-	-	-	1.773	-	3.748	10
MZS2	$Mg_{69}Zn_{27}Sm_4$	-	4.248	-	-	-	1.382	-	4.37	10
MZS3	$Mg_{79}Zn_{17}Sm_4$	-	4.732	-	-	-	2.208	-	3.06	10
MZS4	$Mg_{74}Zn_{17}Sm_9$	-	-	5.106	-	-	1.721	3.173	-	10
MZS5	$Mg_{69}Zn_{22}Sm_9$	-	-	6.298	-	-	0.674	3.028	-	10

Table 3.4 Proportion in weight of starting material required to make up the ternary Mg-Cu-Y, Mg-Cu-Zn and Mg-Zn-Sm alloys.

3.1.2.3 RF induction furnace

Figure 3.8 shows a schematic illustration of the apparatus used to cast the ternary alloys. The 10g alloys were placed into a mild steel crucible, which was suspended in the centre of an induction coil. A power output of 4kV was supplied through the coil, and after completely melting, the liquid alloys were injected into a water-cooled Cu mould, positioned directly beneath the crucible, using a 1bar overpressure of Ar gas. Rapidly solidified wedge-shaped specimens, with dimensions shown in Figure 3.9, were obtained. Prior to the melting, the chamber was placed under high vacuum maintained at 2×10^{-5} mbar using an oil diffusion pump.

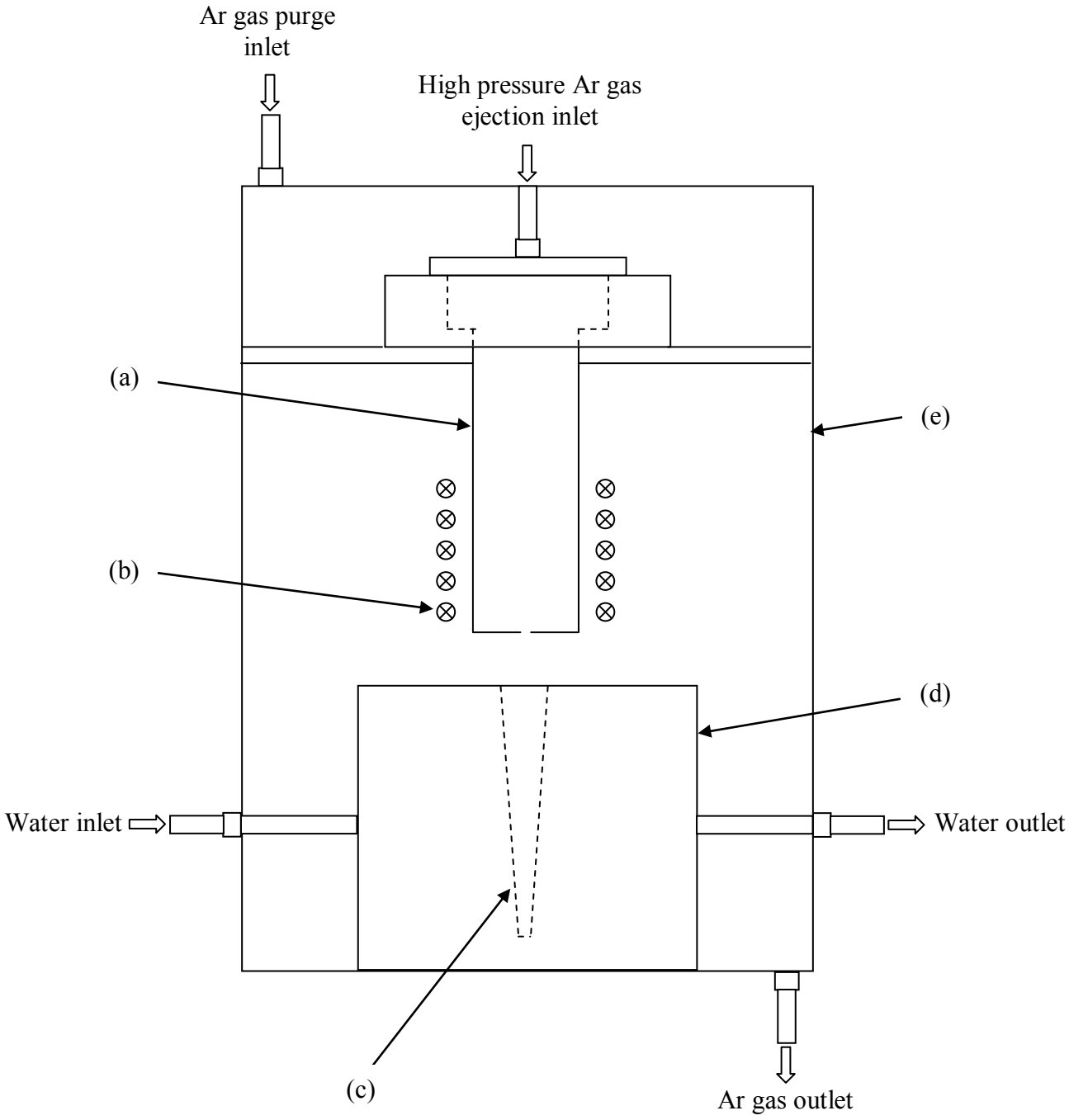

Figure 3.8 Schematic diagram of casting apparatus: (a) mild steel crucible, (b) induction coil, (c) wedge-shaped cavity, (d) water cooled Cu-mould and (e) chamber wall.

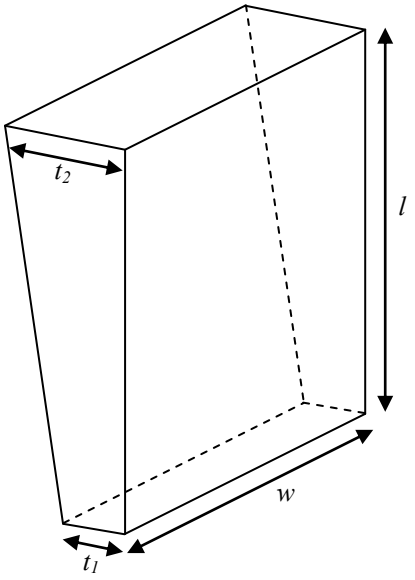

Figure 3.9 Schematic diagram of wedge-shaped specimen obtained through injection casting: l = 50mm, w = 30mm, t_1 = 5mm, and t_2 = 10mm.

3.2 Materials characterisation

3.2.1 Sample preparation of metallography

The alloys were sectioned with a Buehler Isomet 4000 linear precision saw using a silicon-carbide blade before being mounted in conductive Bakelite using an Opal 400 mounting press. All samples were ground to 1200 fine paper and polished to 1 μm diamond suspension paste prior to undergoing any microstructural and chemical analysis. For optical metallography, some of the samples were etched in nital (2% nitric acid, 98% ethanol).

3.2.2 Microstructure

3.2.2.1 Optical microscopy

The alloys were investigated using an optical light microscope operated at magnifications up to x500 to determine the microstructures of the alloys.

3.2.2.2 SEM microscopy

The alloys were examined in a Jeol JSM 6060LV scanning electron microscope (SEM). The secondary electron imaging mode was used to reveal the surface topography of the alloys, while the backscattered electron imaging mode was used to identify the different phases present in the alloys. The compositions of these phases were quantified using energy dispersive spectroscopy (EDS) analysis. In both imaging modes, the accelerating voltage varied from 15 to 25 kV depending upon sample conditions. The electron spot size varied from 8 to 14 nm. The working distance was approximately 20 mm in the secondary electron imaging mode and 10 mm in the backscattered electron imaging mode. A range of magnifications from 100 to 3,000 times was used to view the samples in the SEM.

3.2.3 X-ray diffraction

XRD experiments were carried out in this work in order to obtain the following information:

(a) characterisation of crystalline phases present in the alloys
(b) characterisation of important microstructural features, e.g. changes in grain size and lattice strain.

The cross-sectional surfaces of the alloys of approximately 15 mg were mounted on a sample holder using plasticene. The samples were analysed at room temperature using x-ray diffraction in a Philips X'pert diffractometer. The detector was rotated from 20° to 100° at a rate of 1.5°/min. A Ni-filtered Cu Kα x-ray radiation source with an average wavelength of 0.154056 nm was used.

3.2.4 Thermal analysis

Differential scanning calorimetry (DSC) is a well established method by which the thermodynamic and kinetic data of a phase transition or chemical reaction can be obtained. In this work, a Netzsch differential scanning calorimeter (DSC 404 C) under flowing purified argon (99.998%) was used to study the glass transition, crystallisation, and melting behaviours of the rapidly solidified alloys. Samples of 50mg mass were used for constant dynamic heating experiments. The samples were contained in alumina pans. A heating rate of 10 K/min was employed from temperatures of 50 ºC to 550 ºC. Onset temperature of crystallisation, T_x, glass transition temperature, T_g, and peak crystallisation temperatures, T_p, were determined from the dynamic heating DSC traces. Thus the supercooled liquid region, ΔT_x, defined as the difference between T_g and T_x, was obtained.

3.2.5 Mechanical properties

3.2.5.1 Hardness

Using a Mitutoyo MVK-H1 hardness testing machine, a load of 1Kg was applied by the diamond indenter to the rapidly solidified alloys. A total of 7 measurements were

taken approximately 500μm apart from the edge of the alloy to the centre. An average value was then calculated.

References

[1] W. Klement, R. H. Willens, P. Duwex, Nature, 187(1960)869

[2] H. Tan, Y. Zhang, D. Ma, Y. P. Feng, Y. Li, Acta Materialia, 51(2003)4551

[3] T. B. Massalski, J. L. Murray, L. H. Bennett and H. Baker, "Binary Alloy Phase Diagrams", published by Metals Park, Ohio: American Society for Metals, 1986.

CHAPTER 4 RESULTS

4.1 The design of amorphous alloy compositions using GFA parameters

4.1.1 The relationship between α and ε for amorphous alloys

The liquidus model, given by the parameter α, developed by Cheney and Vecchio [1], which determines and ranks the presence of deep eutectics, has been correlated with the elastic strain model, ε, proposed by Miracle and Senkov [2]. Table 4.1 presents calculated values for these parameters for a range of Mg-, Zr-, Nd-, Ca-, La-, Pd-, Cu-, Gd-, Ti-, and Ni-based amorphous alloys published in the literature.

Composition (at. %)	α	ε
$Mg_{65.5}Cu_{25.5}Gd_9$	1.61	0.021
$Mg_{63.5}Cu_{27.5}Gd_9$	1.55	0.026
$Mg_{61.5}Cu_{29.5}Gd_9$	1.56	0.031
$Mg_{63}Cu_{27}Gd_{10}$	1.57	0.020
$Mg_{61}Cu_{29}Gd_{10}$	1.57	0.025
$Mg_{59}Cu_{31}Gd_{10}$	1.59	0.030
$Mg_{64.5}Cu_{24.5}Gd_{11}$	1.59	0.008
$Mg_{62.5}Cu_{26.5}Gd_{11}$	1.58	0.013
$Mg_{60.5}Cu_{28.5}Gd_{11}$	1.57	0.018
$Mg_{58.5}Cu_{30.5}Gd_{11}$	1.59	0.023
$Mg_{58.5}Cu_{30.5}Gd_9Y_2$	1.59	0.023
$Mg_{58.5}Cu_{30.5}Gd_7Y_4$	1.58	0.023
$Mg_{58.5}Cu_{30.5}Gd_5Y_6$	1.58	0.023
$Mg_{58.5}Cu_{30.5}Gd_3Y_8$	1.57	0.022
$Mg_{58.5}Cu_{30.5}Gd_1Y_{10}$	1.56	0.022
$Mg_{48}Ni_{31}Pr_{21}$	1.66	0.029
$Mg_{63}Ni_{22}Pr_{15}$	1.52	0.021
$Mg_{65}Ni_{21}Pr_{14}$	1.51	0.019
$Mg_{65}Ni_{21}Pr_{14}$ (in air)	1.5	0.019
$Mg_{65}Cu_{7.5}Ni_{7.5}Zn_5Ag_5Y_{10}$	1.45	0.011
$Mg_{65}Cu_{25}Tb_9Y_1$ (vacuum)	1.55	0.023
$Mg_{65}Cu_{25}Tb_8Y_2$ (vacuum)	1.55	0.022
$Mg_{65}Cu_{25}Tb_7Y_3$ (vacuum)	1.54	0.020
$Mg_{65}Cu_{25}Y_{10}$ (vacuum)	1.52	0.013
$Mg_{65}Cu_{25}Tb_{10}$	1.55	0.024
$Mg_{65}Cu_{25}Sm_{10}$	1.51	0.004
$Mg_{65}Cu_{25}Gd_{10}$	1.53	0.014
$Mg_{65}Cu_{25}Dy_{10}$	1.51	0.023
$Mg_{65}Cu_{25}Pr_{10}$	1.46	0.010
$Mg_{65}Cu_{25}Nd_{10}$	1.47	0.008
$Mg_{65}Cu_{25}Ho_{10}$	1.51	0.023
$Mg_{61}Cu_{28}Gd_{11}$	1.62	0.029
$Mg_{77}(Cu_{0.66}Y_{0.34})_{18}Zn_5$	1.45	0.010

$Mg_{83}(Cu_{0.66}Y_{0.34})_{12}Zn_5$	1.39	0.011
$Mg_{85}(Cu_{0.66}Y_{0.34})_{10}Zn_5$	1.38	0.011
$Mg_{87}(Cu_{0.66}Y_{0.34})_8Zn_5$	1.38	0.011
$Mg_{89}(Cu_{0.66}Y_{0.34})_6Zn_5$	1.34	0.011
$Mg_{63}Ni_{22}Pr_{15}$	1.54	0.021
$Mg_{70}Ni_{15}Nd_{15}$	1.3	0.041
$Mg_{65}Ni_{20}Nd_{15}$	1.41	0.030
$Mg_{75}Ni_{15}Nd_{10}$	1.37	0.016
$Mg_{77}Ni_{18}Nd_5$	1.22	0.020
$Mg_{90}Ni_5Nd_5$	1.07	0.015
$Mg_{80}Ni_{10}Nd_{10}$	1.18	0.028
$Mg_{65}Cu_{25}Y_{10}$	1.52	0.013
$Zr_{62.5}Al_{12.1}Cu_{7.95}Ni_{17.45}$	1.58	0.050
$Zr_{63}Al_{11.4}Cu_{9.3}Ni_{16.3}$	1.59	0.052
$Zr_{63.5}Al_{10.7}Cu_{10.7}Ni_{15.1}$	1.6	0.054
$Zr_{64}Al_{10.1}Cu_{11.7}Ni_{14.2}$	1.6	0.056
$Zr_{65}Al_{8.7}Cu_{14.4}Ni_{11.9}$	1.6	0.060
$Zr_{66}Al_8Ni_{26}$	1.55	0.064
$Zr_{66}Al_8Cu_7Ni_{19}$	1.67	0.062
$Zr_{66}Al_8Cu_{12}Ni_{14}$	1.61	0.062
$Zr_{66}Al_9Cu_{16}Ni_9$	1.58	0.055
$Zr_{65}Al_{7.5}Cu_{17.5}Ni_{10}$	1.6	0.067
$Zr_{57}Ti_5Al_{10}Cu_{20}Ni_8$	1.09	0.074
$Zr_{65}Al_{7.5}Cu_{17.5}Ni_{10}$	1.11	0.067
$Zr_{41.2}Ti_{13.8}Cu_{12.5}Ni_{10}Be_{22.5}$	1.09	0.055
$Zr_{38.5}Ti_{16.5}Ni_{9.75}Cu_{15.25}Be_{20}$	1.12	0.114
$Zr_{39.88}Ti_{15.12}Ni_{9.58}Cu_{13.77}Be_{21.25}$	1.09	0.064
$Zr_{42.63}Ti_{12.37}Ni_{10}Cu_{11.25}Be_{23.75}$	1.09	0.045
$Zr_{44}Ti_{11}Ni_{10}Cu_{10}Be_{25}$	1.09	0.035
$Zr_{45.38}Ti_{9.62}Ni_{10}Cu_{8.75}Be_{26.25}$	1.08	0.025
$Zr_{46.25}Ti_{8.25}Ni_{10}Cu_{7.5}Be_{27.5}$	1.08	0.015
$Zr_{55}Ni_{25}Al_{20}$	1.75	0.029
$Nd_{67}Fe_{20}Al_{10}Y_3$	1.15	0.101
$Nd_{65}Fe_{20}Al_{10}Y_5$	1.13	0.100
$Nd_{60}Fe_{20}Al_{10}Y_{10}$	1.14	0.097
$Nd_{55}Fe_{20}Al_{10}Y_{15}$	1.18	0.095
$Ca_{65}Mg_{15}Zn_{20}$	1.6	0.017
$Ca_{60}Mg_{25}Ni_{15}$	1.69	0.039
$Ca_{60}Al_{30}Mg_{10}$	1.47	0.047
$Ca_{60}Al_{30}Ag_{10}$	1.33	0.052
$Ca_{54}Mg_{18}Cu_{28}$	1.71	0.043
$Ca_{59.5}Mg_{16.5}Zn_{24}$	1.49	0.027
$La_{55}Ni_{25}Al_{20}$	1.34	0.112
$La_{55}Al_{25}Ni_{20}$	1.29	0.107
$La_{55}Al_{25}Ni_{10}Cu_{10}$	1.42	0.106
$La_{55}Al_{25}Cu_{20}$	1.26	0.105
$La_{55}Al_{25}Ni_5Cu_{10}Co_5$	1.28	0.105
$La_{55}Al_{25}Ni_{15}Cu_5$	1.28	0.106
$La_{55}Al_{25}Ni_5Cu_{15}$	1.27	0.106
$Pd_{77.5}Cu_6Si_{16.5}$	1.16	0.041
$Pd_{77}Cu_6Si_{17}$	1.16	0.043
$Pd_{79.5}Cu_4Si_{16.5}$	1.18	0.042
$Cu_{60}Zr_{30}Ti_{10}$	1.43	0.090
$Cu_{60}Zr_{20}Ti_{20}$	1.45	0.071

$Cu_{60}Hf_{30}Ti_{10}$	1.5	0.097
$Cu_{60}Hf_{25}Ti_{15}$	1.49	0.087
$Cu_{47}Zr_{11}Ni_{8}Ti_{34}$	1.44	0.057
$Cu_{48}Zr_{48}Al_{4}$	1.4	0.122
$Cu_{45}Zr_{45}Al_{10}$	1.43	0.110
$Gd_{60}Cu_{20}Ni_{10}Al_{10}$	1.69	0.140
$Gd_{56}Al_{24}Co_{20}$	1.5	0.139
$Gd_{36}Y_{20}Al_{24}Co_{20}$	1.44	0.139
$Gd_{40}Y_{16}Al_{24}Co_{20}$	1.51	0.139
$Gd_{50}Y_{6}Al_{24}Co_{20}$	1.51	0.139
$Gd_{36}Nd_{20}Al_{24}Co_{20}$	1.53	0.115
$Gd_{60}Co_{25}Al_{15}$	1.61	0.136
$Gd_{60}Ni_{15}Al_{25}$	1.43	0.122
$Gd_{60}Co_{30}Al_{10}$	1.7	0.143
$Gd_{60}Co_{20}Al_{20}$	1.56	0.129
$Gd_{60}Co_{15}Al_{25}$	1.52	0.122
$Gd_{60}Ni_{25}Al_{15}$	1.67	0.136
$Gd_{60}Ni_{20}Al_{20}$	1.6	0.129
$Gd_{60}Ni_{10}Al_{30}$	1.51	0.114
$Ti_{50}Ni_{15}Cu_{32}Sn_{3}$	1.31	0.040
$Ti_{50}Ni_{15}Cu_{25}Sn_{3}Be_{7}$	1.4	0.013
$Ti_{45}Ni_{15}Cu_{25}Sn_{3}Be_{7}Zr_{5}$	1.49	0.000
$Ti_{49}Ni_{15}Cu_{25}Sn_{3}Be_{7}Zr_{1}$	1.4	0.011
$Ti_{47}Ni_{15}Cu_{25}Sn_{3}Be_{7}Zr_{3}$	1.46	0.005
$Ti_{43}Ni_{15}Cu_{25}Sn_{3}Be_{7}Zr_{7}$	1.49	0.005
$Ni_{59}Zr_{20}Ti_{16}Si_{5}$	1.41	0.057
$Ni_{59}Zr_{20}Ti_{16}Si_{2}Sn_{3}$	1.32	0.064
$Ni_{59}Zr_{20}Ti_{16}Sn_{5}$	1.38	0.066
$Ni_{57}Zr_{20}Ti_{18}Al_{5}$	1.38	0.059
$Ni_{57}Zr_{20}Ti_{17}Al_{5}Sn_{1}$	1.34	0.059

Table 4.1 The α and ε values for amorphous alloys.

The relationships between these distinct modelling techniques, for the amorphous alloys listed in Table 4.1 are graphically illustrated in Figure 4.1. Solid lines indicate the critical values for both the parameter α (>1.5) and elastic strain (>0.054), which must be exceeded in order for the alloys to be considered good glass-formers.

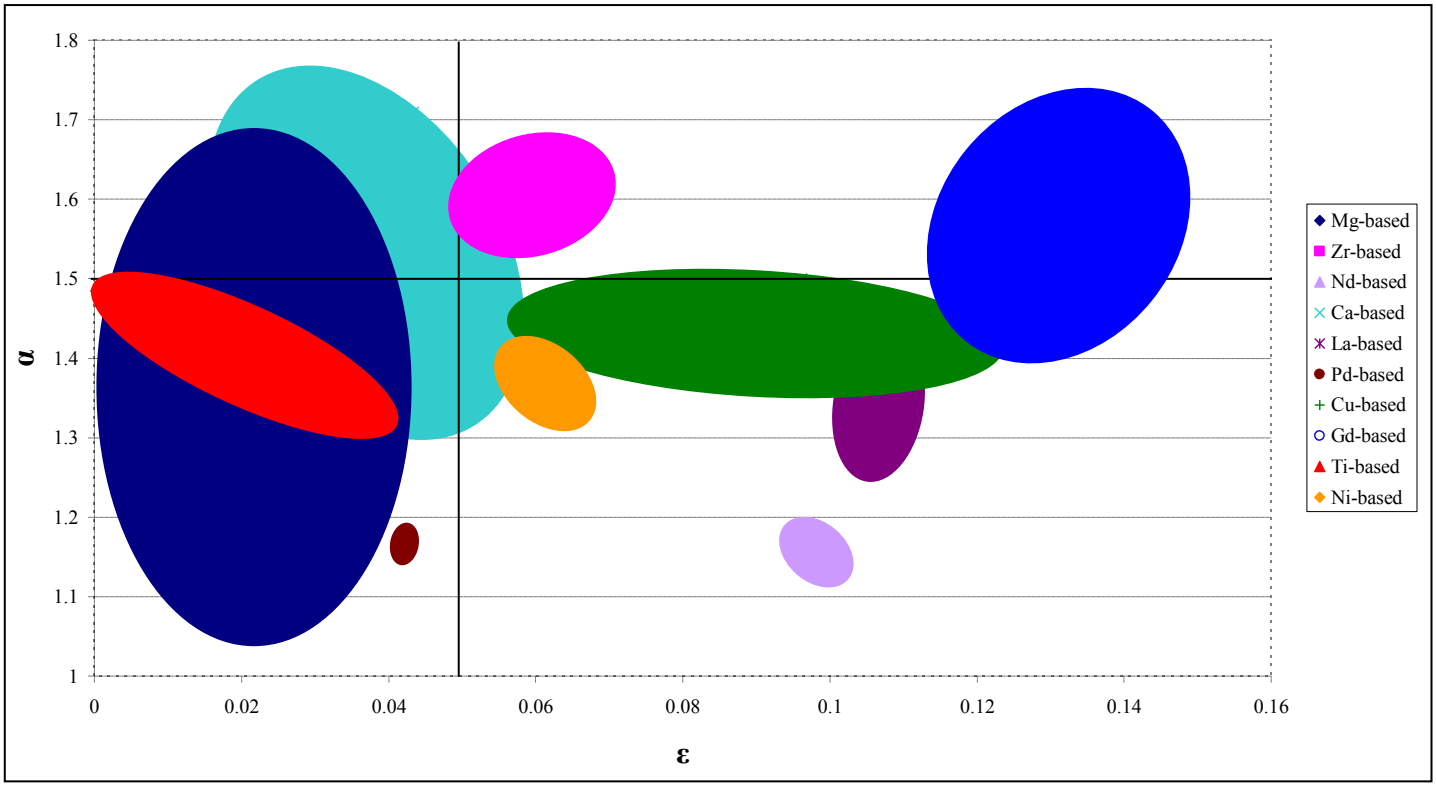

Figure 4.1 The relationship between α and ε for amorphous alloys.

As shown in Figure 4.1, the alloys remarkably group together according to the base metal. Of particular note are the correlations between α and ε for all of the Zr-based and the majority of the Gd-based amorphous alloys. Although α is not directly proportional to D_{max} [3], the graphical representation indicates that these alloy systems will have good GFA, as the values for both α and ε exceed the critical values. In addition, Figure 4.1 also shows that the calculated elastic strain is above the critical value, 0.054, for the Nd-, Ni-, La-, and Cu-based glass-forming compositions. However, the calculated α values for these compositions are <1.5, indicating lower glass-forming ability.

The Ti-, Pd-, and a proportion of the Mg- and Ca-based amorphous alloys are of significant interest. According to Figure 4.1, these alloys should be poor glass-formers as neither the α or the ε values are above the critical values; however, experimental data provides conflicting results, which suggests the liquidus and elastic strain models cannot be applied to these particular alloy systems. Conversely, the remaining Mg- and Ca-based amorphous alloys appear to have high α values of >1.5, suggesting a

strong tendency of glass-formation; however, these alloys do not fit with the elastic strain model of what constitutes a good glass-forming system as the ε values are <0.054.

4.1.2 The relationship between GFA parameters and composition

4.1.2.1 Mg-Cu-Y system

The calculated results of the GFA predictive models for a large part of the compositional range of the Mg-Cu-Y ternary system are graphically presented in Figure 4.2. Remarkably, all of the GFA predictive models, with the exception of the reduced melting temperature (T_{rm}), show an extremely similar trend. According to the ternary diagrams, the alloy compositions with theoretical high GFA are located towards the midpoint of the Y-Cu binary line.

Table 4.2 displays the calculated numerical values of the GFA predictive models for a large part of the compositional range of the Mg-Cu-Y system. In addition to the values calculated from a systematic scan of the ternary system, Table 4.2 also displays the values for the specifically selected alloy compositions MCY1 to MCY7. It is evident that the highest α value can be observed for the ternary eutectic alloy MCY1, indicating high GFA. However, the local elastic strain of this particular alloy composition is below the critical value for glass-formation, according to Miracle and Senkov [2]. Of particular note are alloys MCY2, MCY5, and MCY6 as these alloys display values above the specified critical levels for all GFA model parameters.

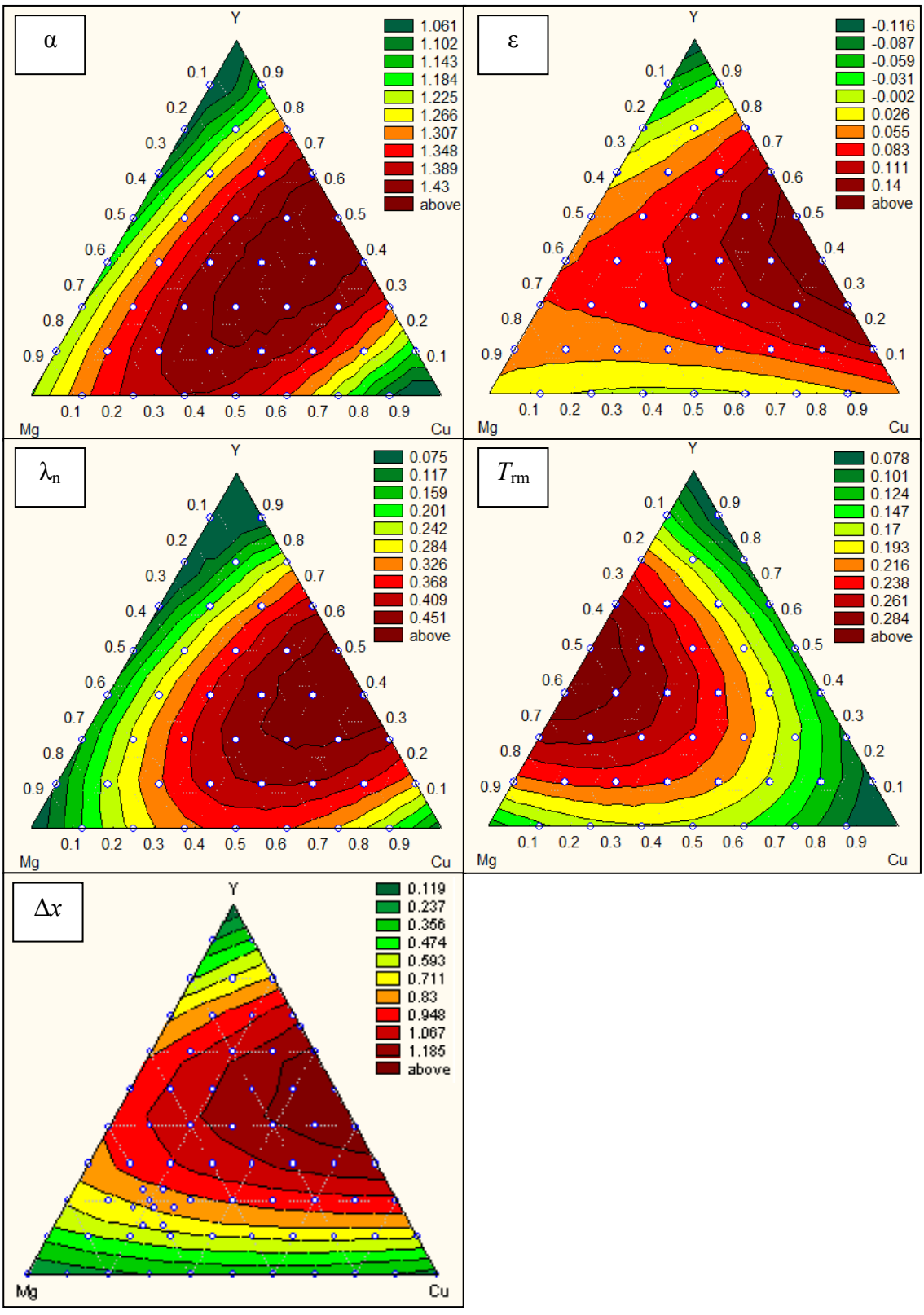

Figure 4.2 The Mg-Cu-Y ternary system showing α-parameter, local strain (ε), λ_n criteria, reduced melting temperature (T_{rm}) and electronegativity difference (Δx) values at different compositions.

ID.	Composition (at. %)	Estimated T_L (K)	α	ε	λ_n	T_{rm}	Δx
-	$Y_{87.5}Mg_{12.5}$	1650	1.02	0.04	0.03	0.11	0.28746
-	$Y_{87.5}Cu_{12.5}$	1550	1.12	0.05	0.08	0.06	0.32569
-	$Y_{75}Mg_{25}$	1550	1.02	0.09	0.07	0.21	0.33419
-	$Y_{75}Cu_{12.5}Mg_{12.5}$	1450	1.13	0.01	0.11	0.15	0.35952
-	$Y_{75}Cu_{25}$	1250	1.35	0.10	0.16	0.10	0.38037
-	$Y_{62.5}Mg_{37.5}$	1400	1.05	0.14	0.10	0.28	0.35920
-	$Y_{62.5}Mg_{25}Cu_{12.5}$	1250	1.22	0.04	0.15	0.22	0.37896
-	$Y_{62.5}Cu_{25}Mg_{12.5}$	1150	1.37	0.06	0.19	0.17	0.39594
-	$Y_{62.5}Cu_{37.5}$	1100	1.48	0.14	0.24	0.13	0.41086
-	$Mg_{50}Y_{50}$	1250	1.09	0.19	0.14	0.32	0.37127
-	$Y_{50}Mg_{37.5}Cu_{12.5}$	1100	1.28	0.09	0.18	0.27	0.38787
-	$Y_{50}Mg_{25}Cu_{25}$	950	1.54	0.02	0.22	0.22	0.40240
-	$Y_{50}Cu_{37.5}Mg_{12.5}$	1050	1.45	0.14	0.27	0.18	0.41532
-	$Cu_{50}Y_{50}$	1150	1.37	0.17	0.31	0.14	0.42696
-	$Mg_{62.5}Y_{37.5}$	1100	1.14	0.15	0.14	0.33	0.37179
-	$Mg_{50}Y_{37.5}Cu_{12.5}$	1050	1.24	0.13	0.20	0.29	0.38638
-	$Mg_{37.5}Y_{37.5}Cu_{25}$	900	1.51	0.11	0.26	0.24	0.39919
-	$Cu_{37.5}Y_{37.5}Mg_{25}$	950	1.37	0.16	0.87	0.20	0.41058
-	$Cu_{50}Y_{37.5}Mg_{12.5}$	1050	1.40	0.15	0.75	0.17	0.42080
-	$Cu_{62.5}Y_{37.5}$	1100	1.38	0.14	0.63	0.14	0.43004
-	$Mg_{75}Y_{25}$	1050	1.09	0.11	0.09	0.29	0.35807
-	$Mg_{62.5}Y_{25}Cu_{12.5}$	950	1.26	0.09	0.15	0.29	0.37141
-	$Mg_{50}Y_{25}Cu_{25}$	850	1.47	0.06	0.21	0.26	0.38297
-	$Cu_{37.5}Mg_{37.5}Y_{25}$	850	1.53	0.14	0.78	0.22	0.39308
-	$Cu_{50}Mg_{25}Y_{25}$	950	1.43	0.13	0.66	0.16	0.40199
-	$Cu_{62.5}Y_{25}Mg_{12.5}$	1000	1.41	0.12	0.54	0.14	0.40985
-	$Cu_{75}Y_{25}$	1150	1.28	0.11	0.42	0.11	0.41677
-	$Mg_{87.5}Y_{12.5}$	850	1.21	0.06	0.05	0.19	0.31889
-	$Mg_{75}Cu_{12.5}Y_{12.5}$	800	1.36	0.03	0.11	0.23	0.33214
-	$Mg_{62.5}Cu_{25}Y_{12.5}$	750	1.52	0.00	0.17	0.24	0.34302
-	$Mg_{50}Cu_{37.5}Y_{12.5}$	750	1.59	0.03	0.23	0.23	0.35203
-	$Cu_{50}Mg_{37.5}Y_{12.5}$	850	1.47	0.10	0.57	0.20	0.35944
-	$Cu_{62.5}Mg_{25}Y_{12.5}$	950	1.37	0.09	0.45	0.15	0.36546
-	$Cu_{75}Mg_{12.5}Y_{12.5}$	1050	1.29	0.08	0.33	0.08	0.37020
-	$Cu_{87.5}Y_{12.5}$	1150	1.23	0.06	0.21	0.07	0.37372
-	$Mg_{87.5}Cu_{12.5}$	750	1.30	0.03	0.61	0.10	0.17076
-	$Mg_{75}Cu_{25}$	750	1.37	0.07	0.12	0.16	0.19648
-	$Mg_{62.5}Cu_{37.5}$	800	1.36	0.11	0.18	0.19	0.20892

-	$Cu_{50}Mg_{50}$	950	1.20	0.07	0.24	0.19	0.21352
-	$Cu_{62.5}Mg_{37.5}$	1050	1.14	0.05	0.36	0.17	0.21131
-	$Cu_{75}Mg_{25}$	1050	1.19	0.04	0.24	0.13	0.20101
-	$Cu_{87.5}Mg_{12.5}$	1150	1.13	0.02	0.12	0.07	0.17670
MCY1	$Mg_{60}Cu_{22}Y_{18}$	670	1.77	0.03	0.19	0.26	0.36244
MCY2	$Mg_{60}Cu_{17}Y_{23}$	750	1.50	0.07	0.21	0.28	0.37155
MCY3	$Mg_{60}Cu_{27}Y_{13}$	740	1.50	0.00	0.17	0.24	0.34697
MCY4	$Mg_{65}Cu_{22}Y_{13}$	750	1.55	0.01	0.15	0.24	0.34298
MCY5	$Mg_{55}Cu_{22}Y_{23}$	750	1.68	0.06	0.23	0.27	0.37607
MCY6	$Mg_{65}Cu_{17}Y_{18}$	800	1.61	0.05	0.18	0.26	0.35806
MCY7	$Mg_{55}Cu_{27}Y_{18}$	800	1.61	0.02	0.20	0.25	0.36655

Table 4.2 GFA predictive parameter values for different compositions in the Mg-Cu-Y ternary system.

4.1.2.2 Mg-Cu-Zn system

The calculated results of the GFA predictive models for a large part of the compositional range of the Mg-Cu-Zn ternary system are graphically presented in Figure 4.3. In contrast to the Mg-Cu-Y system, the GFA models show no relationship, indicating a degree of difficulty in predicting GFA for this particular ternary system.

Table 4.3 displays the calculated numerical values of the GFA predictive models for a large part of the compositional range of the Mg-Cu-Zn system. Again, values for the specifically selected alloys are also provided. It is apparent that α values range from 0.83 to 1.33, suggesting only limited glass-forming ability, since only α values greater than 1.5 suggests a very strong tendency for glass formation. Similar conclusions regarding the GFA of the Mg-Cu-Zn system may be drawn with reference to the values calculated using the λ_n criteria and the reduced melting temperature since these values also fall below the critical levels required for glass-formation. However, in contrast, the calculated elastic strain is above the critical value, 0.054, for some of the compositions and for all of the specifically selected alloys (with the exception of MCZ6), indicating possible good glass-forming ability for these particular alloys.

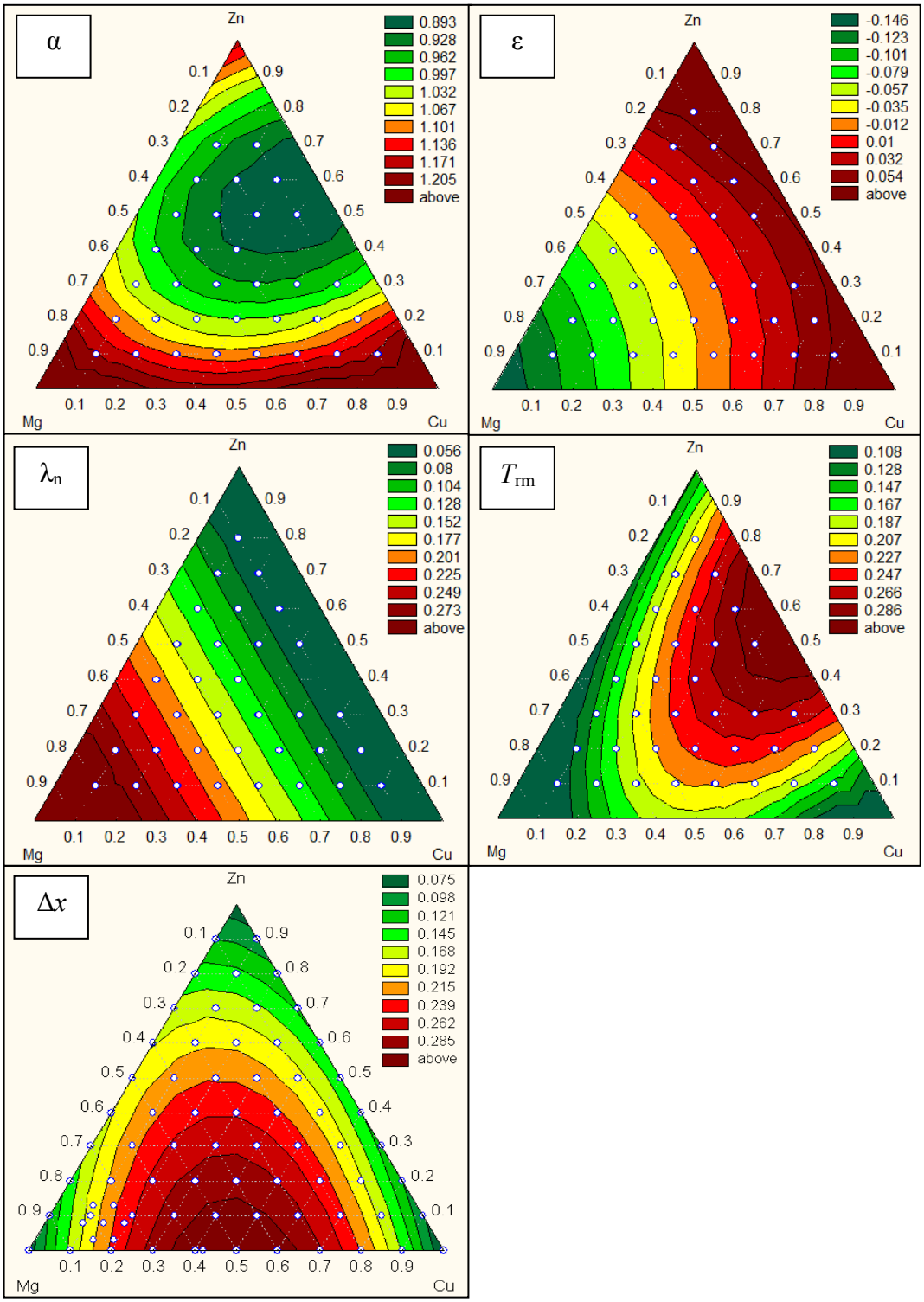

Figure 4.3 The Mg-Cu-Zn ternary system showing alpha (α), local strain (ε), λ_n, reduced melting temperature (T_{rm}) and electronegativity difference (Δx) values at different compositions.

ID.	Composition (at. %)	Estimated T_L (K)	α	ε	λ_n	T_{rm}	Δx
-	$Zn_{80}Cu_{10}Mg_{10}$	773	1.01	0.02	0.04	0.18	0.3923
-	$Zn_{70}Mg_{20}Cu_{10}$	923	0.87	0.04	0.07	0.20	0.4405
-	$Zn_{70}Cu_{20}Mg_{10}$	923	0.92	0.02	0.04	0.26	0.3947
-	$Zn_{60}Mg_{30}Cu_{10}$	993	0.83	0.06	0.11	0.20	0.4696
-	$Zn_{60}Cu_{20}Mg_{20}$	993	0.88	0.04	0.07	0.25	0.4372
-	$Zn_{60}Cu_{30}Mg_{10}$	973	0.94	0.02	0.04	0.29	0.3929
-	$Zn_{50}Mg_{40}Cu_{10}$	993	0.86	0.08	0.15	0.19	0.4835
-	$Zn_{50}Mg_{30}Cu_{20}$	1073	0.83	0.06	0.11	0.23	0.4657
-	$Zn_{50}Cu_{30}Mg_{20}$	1053	0.89	0.04	0.07	0.27	0.4339
-	$Zn_{50}Cu_{40}Mg_{10}$	993	0.99	0.02	0.03	0.31	0.3867
-	$Mg_{50}Zn_{40}Cu_{10}$	973	0.90	0.14	0.19	0.17	0.4862
-	$Mg_{40}Zn_{40}Cu_{20}$	1073	0.85	0.17	0.15	0.20	0.4788
-	$Zn_{40}Cu_{30}Mg_{30}$	1073	0.90	0.06	0.11	0.25	0.4616
-	$Cu_{40}Zn_{40}Mg_{20}$	1073	0.94	0.03	0.07	0.28	0.4305
-	$Cu_{50}Zn_{40}Mg_{10}$	1023	1.02	0.02	0.04	0.29	0.3755
-	$Mg_{60}Zn_{30}Cu_{10}$	898	1.00	0.11	0.22	0.14	0.4785
-	$Mg_{50}Zn_{30}Cu_{20}$	1023	0.92	0.14	0.19	0.18	0.4804
-	$Mg_{40}Cu_{30}Zn_{30}$	1073	0.92	0.17	0.15	0.23	0.4739
-	$Cu_{40}Mg_{30}Zn_{30}$	1073	0.96	0.04	0.11	0.26	0.4575
-	$Cu_{50}Zn_{30}Mg_{20}$	1073	1.00	0.03	0.07	0.27	0.4270
-	$Cu_{60}Zn_{30}Mg_{10}$	1073	1.04	0.02	0.04	0.26	0.3697
-	$Mg_{70}Zn_{20}Cu_{10}$	823	1.12	0.08	0.26	0.10	0.4593
-	$Mg_{60}Cu_{20}Zn_{20}$	973	0.99	0.11	0.22	0.16	0.4714
-	$Mg_{50}Cu_{30}Zn_{20}$	1048	0.96	0.14	0.19	0.21	0.4745
-	$Cu_{40}Mg_{40}Zn_{20}$	1073	0.98	0.06	0.15	0.23	0.4689
-	$Cu_{50}Mg_{30}Zn_{20}$	1073	1.02	0.04	0.11	0.24	0.4532
-	$Cu_{60}Mg_{20}Zn_{20}$	1023	1.11	0.03	0.07	0.23	0.4235
-	$Cu_{70}Zn_{20}Mg_{10}$	1123	1.05	0.02	0.04	0.21	0.3670
-	$Mg_{80}Cu_{10}Zn_{10}$	773	1.22	0.05	0.30	0.09	0.4238
-	$Mg_{70}Cu_{20}Zn_{10}$	823	1.20	0.08	0.26	0.15	0.4501
-	$Mg_{60}Cu_{30}Zn_{10}$	948	1.09	0.11	0.22	0.19	0.4641
-	$Mg_{50}Cu_{40}Zn_{10}$	1023	1.05	0.15	0.19	0.21	0.4684
-	$Cu_{50}Mg_{40}Zn_{10}$	1073	1.04	0.06	0.15	0.22	0.4637
-	$Cu_{60}Mg_{30}Zn_{10}$	1073	1.08	0.04	0.11	0.20	0.4489
-	$Cu_{70}Mg_{20}Zn_{10}$	973	1.24	0.03	0.07	0.18	0.4199
-	$Cu_{80}Mg_{10}Zn_{10}$	1173	1.06	0.02	0.04	0.14	0.3641
MCZ1	$Mg_{78}Cu_{14}Zn_8$		1.33	0.06	0.06	0.11	0.4279
MCZ2	$Mg_{78}Cu_{19}Zn_3$		1.33	0.06	0.06	0.14	0.4218

MCZ3	$Mg_{78}Cu_9Zn_{13}$	1.19	0.06	0.06	0.08	0.4339
MCZ4	$Mg_{73}Cu_{14}Zn_{13}$	1.23	0.07	0.07	0.12	0.4468
MCZ5	$Mg_{83}Cu_{14}Zn_3$	1.30	0.05	0.05	0.11	0.4022
MCZ6	$Mg_{83}Cu_9Zn_8$	1.24	0.04	0.05	0.08	0.4097
MCZ7	$Mg_{73}Cu_{19}Zn_8$	1.28	0.07	0.07	0.14	0.4417

Table 4.3 GFA predictive parameter values for different compositions in the Mg-Cu-Zn ternary system.

4.1.2.3 Mg-Zn-Sm system

The calculated results of the GFA predictive models for a large part of the compositional range of the Mg-Zn-Sm ternary system are graphically presented in Figure 4.4. It should be noted that the α values have not been plotted. This is because these values cannot be calculated without liquidus temperatures, and this information is not available from the ternary phase diagram. Interestingly, this system is comparable to the Mg-Cu-Y system, as the GFA predictive models, with the exception of the λ_n criteria, show a similar trend. According to the ternary diagrams, the alloy compositions with theoretical high GFA are located around the midpoint of the Sm-Zn binary line.

Table 4.4 displays the calculated numerical values of the GFA predictive models for a large part of the compositional range of the Mg-Zn-Sm system. In addition to the values calculated from a systematic scan of the ternary system, this table also displays the values for the specifically selected alloy compositions MZS1 to MZS5. It is noticeable that the local strain values range quite considerably from 0.00 to 0.22, suggesting variation in the GFA across the compositional range of the Mg-Zn-Sm system. Additionally, it should be noted that the local strain for all of the selected alloys falls below the critical value of 0.054. Again, similar conclusions regarding the GFA of the Mg-Zn-Sm system may be drawn with reference to the values calculated using the λ_n criteria and the reduced melting temperature since these values also fall below the critical levels required for glass-formation.

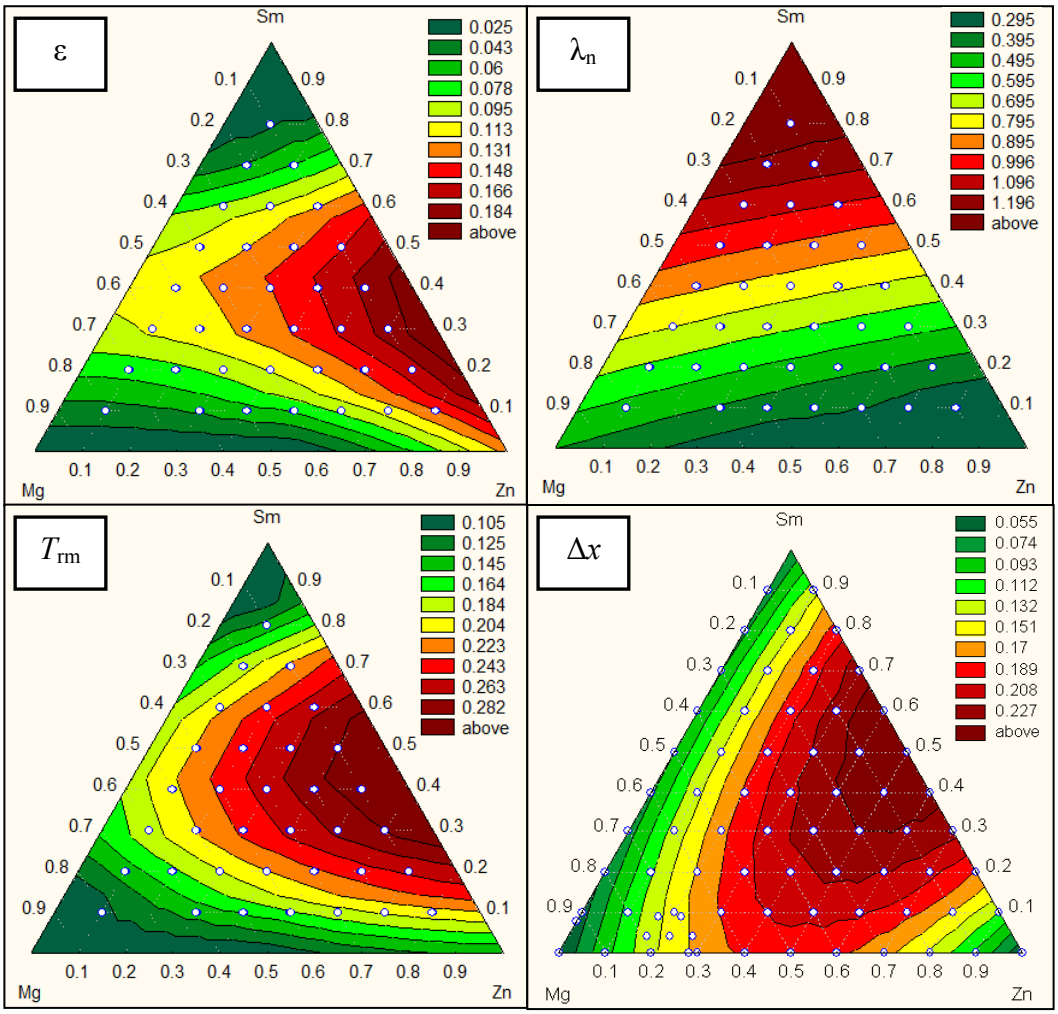

Figure 4.4 The Mg-Zn-Sm ternary system showing strain (ε), λ_n, reduced melting temperature (T_{rm}) and electronegativity difference (Δx) values at different compositions. Note that the α values have not been plotted. This is because these values cannot be calculated without liquidus temperatures, and this information is not available from the ternary phase diagram.

ID.	Composition (at. %)	ε	λ_n	T_{rm}	Δx
-	$Sm_{80}Zn_{10}Mg_{10}$	0.04	1.30	0.14	0.40250
-	$Sm_{70}Mg_{20}Zn_{10}$	0.05	1.18	0.18	0.43170
-	$Sm_{70}Zn_{20}Mg_{10}$	0.07	1.14	0.21	0.44778
-	$Sm_{60}Mg_{30}Zn_{10}$	0.06	1.06	0.20	0.45116
-	$Sm_{60}Zn_{20}Mg_{20}$	0.08	1.02	0.23	0.46500
-	$Sm_{60}Zn_{30}Mg_{10}$	0.10	0.98	0.26	0.47776
-	$Sm_{50}Mg_{40}Zn_{10}$	0.07	0.94	0.21	0.46263
-	$Sm_{50}Mg_{30}Zn_{20}$	0.09	0.90	0.24	0.47495
-	$Sm_{50}Zn_{30}Mg_{20}$	0.11	0.86	0.26	0.48641
-	$Sm_{50}Zn_{40}Mg_{10}$	0.13	0.82	0.29	0.49714
-	$Mg_{50}Sm_{40}Zn_{10}$	0.17	0.82	0.21	0.46609
-	$Mg_{40}Sm_{40}Zn_{20}$	0.15	0.78	0.23	0.47730
-	$Sm_{40}Zn_{30}Mg_{30}$	0.12	0.74	0.25	0.48776
-	$Zn_{40}Sm_{40}Mg_{20}$	0.14	0.70	0.28	0.49757
-	$Zn_{50}Sm_{40}Mg_{10}$	0.22	0.67	0.30	0.50680
-	$Mg_{60}Sm_{30}Zn_{10}$	0.13	0.70	0.19	0.45984
-	$Mg_{50}Sm_{30}Zn_{20}$	0.11	0.66	0.20	0.47022
-	$Mg_{40}Zn_{30}Sm_{30}$	0.10	0.62	0.22	0.47986
-	$Zn_{40}Mg_{30}Sm_{30}$	0.20	0.58	0.24	0.48887
-	$Zn_{50}Sm_{30}Mg_{20}$	0.19	0.55	0.26	0.49731
-	$Zn_{60}Sm_{30}Mg_{10}$	0.18	0.61	0.29	0.50523
-	$Mg_{70}Sm_{20}Zn_{10}$	0.09	0.57	0.15	0.43933
-	$Mg_{60}Zn_{20}Sm_{20}$	0.07	0.54	0.16	0.44908
-	$Mg_{50}Zn_{30}Sm_{20}$	0.05	0.50	0.17	0.45803
-	$Zn_{40}Mg_{40}Sm_{20}$	0.03	0.46	0.19	0.46627
-	$Zn_{50}Mg_{30}Sm_{20}$	0.16	0.43	0.22	0.47387
-	$Zn_{60}Mg_{20}Sm_{20}$	0.15	0.39	0.24	0.48089
-	$Zn_{70}Sm_{20}Mg_{10}$	0.14	0.35	0.25	0.48737
-	$Mg_{80}Zn_{10}Sm_{10}$	0.04	0.45	0.09	0.39094
-	$Mg_{70}Zn_{20}Sm_{10}$	0.01	0.42	0.10	0.40050
-	$Mg_{60}Zn_{30}Sm_{10}$	.01	0.38	0.14	0.40891
-	$Mg_{50}Zn_{40}Sm_{10}$	0.03	0.34	0.16	0.41632
-	$Mg_{50}Zn_{40}Sm_{10}$	0.13	0.31	0.18	0.42282
-	$Zn_{60}Mg_{30}Sm_{10}$	0.12	0.27	0.19	0.42849
-	$Zn_70Mg_{20}Sm_{10}$	0.10	0.23	0.19	0.43337
-	$Zn_{80}Mg_{10}Sm_{10}$	0.09	0.19	0.18	0.43750
MZS1	$Mg_{74}Zn_{22}Sm_4$	0.03	0.09	0.10	0.33771
MZS2	$Mg_{69}Zn_{27}Sm_4$	0.04	0.11	0.11	0.34211
MZS3	$Mg_{79}Zn_{17}Sm_4$	0.01	0.08	0.08	0.33282

MZS4	$Mg_{74}Zn_{17}Sm_9$	0.02	0.12	0.08	0.38999
MZS5	$Mg_{69}Zn_{22}Sm_9$	0.00	0.14	0.10	0.39450

Table 4.4 GFA predictive parameter values for different compositions in the Mg-Zn-Sm ternary system.

4.2 As-cast alloys

4.2.1 Microstructure

4.2.1.1 Mg-Cu-Y alloys

Figure 4.5 shows typical backscattered electron (BSE) micrographs of the Mg-Cu-Y as-cast alloys. In BSE imaging mode, heavy elements appear bright and lighter elements appear dark. The multiphase appearance is typical of alloys cooled naturally from the melt. Observations of the micrographs reveal that all of the alloys contain three phases. However, some phases exist in some of the alloys but are not present in the microstructures of others.

According to the EDS analysis (data listed in Table 4.5) and with reference to the ternary phase diagram of the Mg-Cu-Y system, it is believed the solidification reaction process for alloys MCY1, MCY2, MCY3, MCY5, MCY6, and MCY7 is the following:

Liquid → Y_2Cu_2Mg + liquid → δ + $CuMg_2$ + Y_2Cu_2Mg.

According to the EDS analysis, it can be assumed that the light and light-grey phases observed in the as-cast images for these alloys are Y_2Cu_2Mg and δ, respectively. In addition, $CuMg_2$ may be attributed to the dark phase, which is consistent with observations made by other authors for a similar alloy [4].

Alloy MCY4 is located closer to the Mg_2Cu phase field on the ternary phase diagram. Therefore, in accordance with the EDS analysis, it has been deduced that the solidification reaction process for this particular alloy is the following:

Liquid → Mg_2Cu + liquid → hcp Mg + ε + Mg_2Cu.

The dark phase present in this alloy is Mg-rich with Mg content exceeding 65 at. %. This correlates with the hcp Mg phase in the ternary Mg-Cu-Y phase diagram. This

phase contains no Y content, which explains why it appears dark in BSE imaging mode. The light-grey and grey phases are assumed to be ε and Mg_2Cu, respectively.

Following observations of the as-cast microstructures displayed in Figure 4.4, it is evident that alloys MCY1 and MCY2 contain lath-like light phases. In contrast, despite alloy MCY3 containing the same content of Mg (60 at. %), the Y content is decreased, which dramatically reduces the lath-like light phase. Observations of alloys MCY4 and MCY6 indicate that despite these alloys containing a Mg content of 65 at. %, the reduction of Y content in alloy MCY4 results in an increase in the amount of light phase present in the microstructure of this alloy. In contrast to the other Mg-Cu-Y alloys studied within this subject, alloys MCY5 and MCY7 both contain dark needle-like features. These alloys have the same low Mg content of 55 at. %. However, the Y content is higher in MCY5 compared to MCY7 resulting in a larger light phase being present in alloy MCY5.

In summary, a decrease in Y content reduces the lath-like light phase. By increasing the Cu content, the grey and dark phases appear to increase. Furthermore, by reducing the Mg content, the fine needle-like dark phase appears to increase. In addition to quantifying the proportion of individual elements within the different phases of the alloy microstructures, EDS analysis indicates that the overall chemical composition is nearly identical to the designed nominal composition of the alloys.

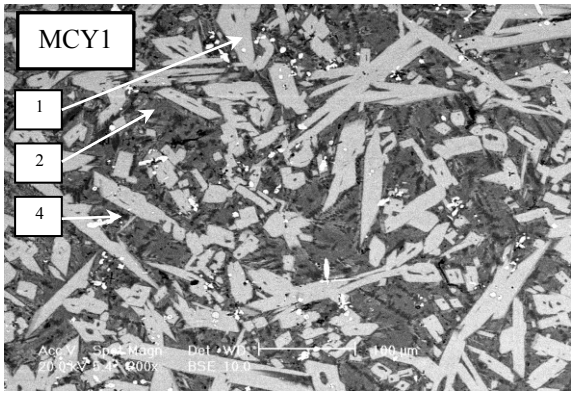

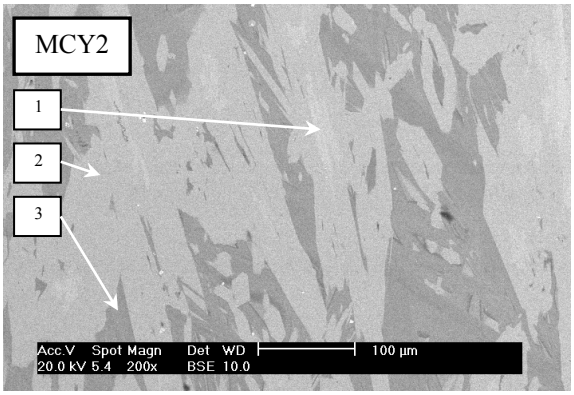

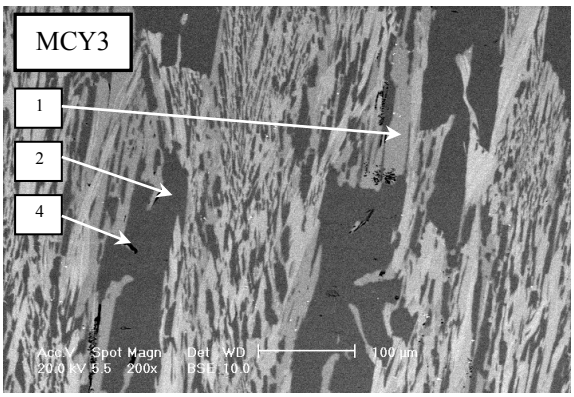

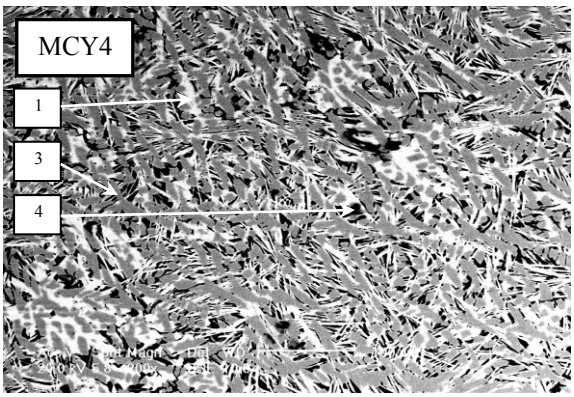

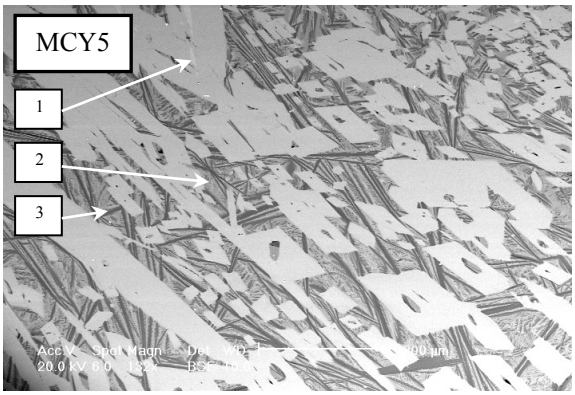

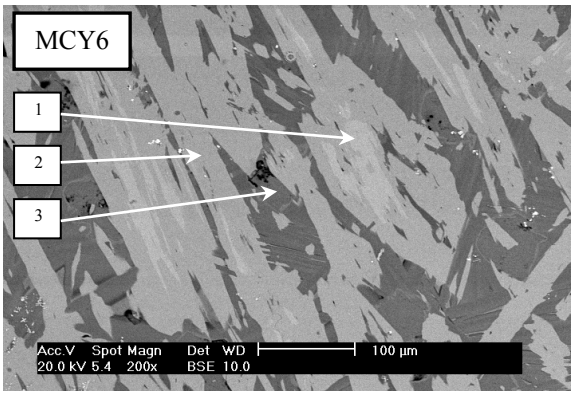

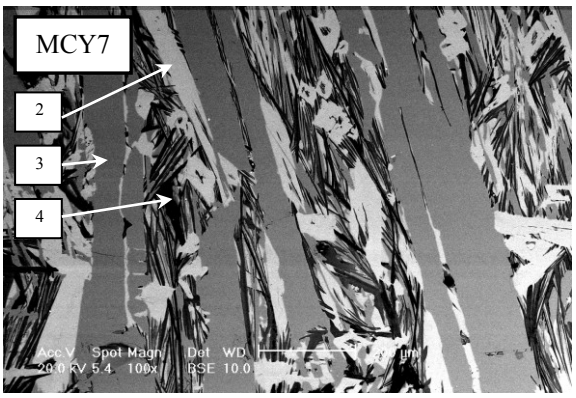

Phase description:

1. Light
2. Light-grey
3. Grey
4. Dark

Figure 4.5 SEM backscattered electron images showing the microstructures of Mg-Cu-Y as-cast alloys at magnification x200.

ID.	Composition (at. %)	Element	Light phase	Light-grey phase	Grey phase	Dark phase
MCY1	$Mg_{60}Cu_{22}Y_{18}$	Mg	36.83 (15.00)	54.97 (28.22)	-	64.74 (41.27)
		Cu	21.37 (22.74)	23.86 (32.02)	-	35.26 (58.73)
		Y	41.80 (62.26)	21.17 (39.76)	-	0 (0)
MCY2	$Mg_{60}Cu_{17}Y_{23}$	Mg	60.68 (32.96)	64.40 (36.56)	81.97 (58.05)	-
		Cu	19.51 (27.70)	17.64 (26.16)	8.53 (15.89)	-
		Y	19.81 (39.34)	17.96 (37.28)	10.00 (26.06)	-
MCY3	$Mg_{60}Cu_{27}Y_{13}$	Mg	59.74 (32.48)	63.32 (35.62)	-	64.65 (41.17)
		Cu	22.07 (31.36)	18.84 (27.70)	-	35.35 (58.83)
		Y	18.19 (36.17)	17.83 (36.68)	-	0 (0)
MCY4	$Mg_{65}Cu_{22}Y_{13}$	Mg	-	66.18 (38.84)	64.98 (37.72)	65.30 (41.86)
		Cu	-	18.63 (28.58)	19.94 (30.26)	34.70 (58.14)
		Y	-	15.18 (32.58)	15.08 (32.02)	0 (0)
MCY5	$Mg_{55}Cu_{22}Y_{23}$	Mg	59.08 (31.59)	63.98 (36.20)	87.75 (69.51)	-
		Cu	20.80 (29.06)	18.19 (26.90)	6.04 (12.51)	-
		Y	20.12 (39.34)	17.83 (36.90)	6.21 (17.98)	-
MCY6	$Mg_{65}Cu_{17}Y_{18}$	Mg	59.82 (32.18)	64.45 (36.55)	79.40 (55.00)	-
		Cu	19.97 (28.08)	17.40 (25.79)	9.92 (17.95)	-
		Y	20.20 (39.74)	18.16 (37.66)	10.68 (27.05)	-
MCY7	$Mg_{55}Cu_{27}Y_{18}$	Mg	-	65.91 (38.39)	72.03 (47.42)	63.64 (40.11)
		Cu	-	18.14 (27.62)	21.48 (36.96)	36.36 (59.89)
		Y	-	15.95 (33.98)	6.49 (15.62)	0 (0)

Table 4.5 EDS analysis revealing the atomic and (weight) percentages of elements present in the different phases of the as-cast Mg-Cu-Y alloy microstructures.

4.2.1.2 Mg-Cu-Zn alloys

Figure 4.6 shows typical backscattered electron (BSE) micrographs of the Mg-Cu-Zn as-cast alloys. Examination of the microstructures reveals that multiple phases coexist in these alloys. However, some phases exist in some of the alloys but are not present in the microstructures of others.

According to the EDS analysis (data listed in Table 4.6) and with reference to the ternary phase diagram of the Mg-Cu-Zn system, it is believed the solidification reaction process for alloys MCZ1, MCZ3, MCZ4, and MCZ7 is the following:

Liquid → $MgCu_2$ + liquid → Mg + Mg_2Cu + $MgCu_2$.

According to the EDS analysis, it can be assumed that the blocky light phase observed in the as-cast images for these alloys is $MgCu_2$. In addition, Mg_2Cu and Mg may be attributed to the grey and dark phases, respectively.

Alloys MCZ2 and MCZ5 are located closer to the Mg_2Cu phase field on the ternary phase diagram. Therefore, in accordance with the EDS analysis, it has been deduced that the solidification reaction process for this particular alloy is the following:

Liquid → Mg_2Cu + liquid → Mg_2Cu + Mg + ?$MgCu_2$.

Since alloy MCZ6 is compositionally located close to the Mg phase field on the ternary phase diagram and with reference to the EDS analysis, it is thought that the solidification reaction process is the following for this alloy:

Liquid → Mg + Liquid → Mg_2Cu + Mg + $MgCu_2$.

Following observations of the as-cast microstructures displayed in Figure 4.5, it is evident that the blocky light phase present in the microstructure of alloy MCZ1 is lower than in MCZ2, despite these alloys containing the same Mg content of 78 at. %. It can be assumed that the decrease in Cu and increase in Zn contents for alloy MCZ1

compared with MCZ2 results in a reduction of the light phase. Moreover, alloy MCZ3 also contains a Mg content of 78 at. % but with a high Zn content of 13 at. %. This results in an additional reduction in the amount of light phase present in the microstructure. Further still, if one compares the microstructures of alloys MCZ4 and MCZ7, it is apparent that regardless of these alloys containing the same Mg content of 73 at. %, the higher Zn content found in alloy MCZ4 reduces the amount of light phase. Following observations of the as-cast images, it is clear that the microstructures of alloys MCZ5 and MCZ6 contain a higher amount of dark phase compared with the other alloys. This may be explained by the high Mg content of 83 at. % found within these alloys.

In summary, a higher amount of Mg content increases the amount of dark phase present within the microstructure of these alloys. By reducing the Zn content in the alloy, the light phase with a blocky and dendritic morphology appears to increase. In addition to quantifying the proportion of individual elements within the different phases of the alloy microstructures, EDS analysis indicates that the overall chemical composition is nearly identical to the designed nominal composition of the alloys.

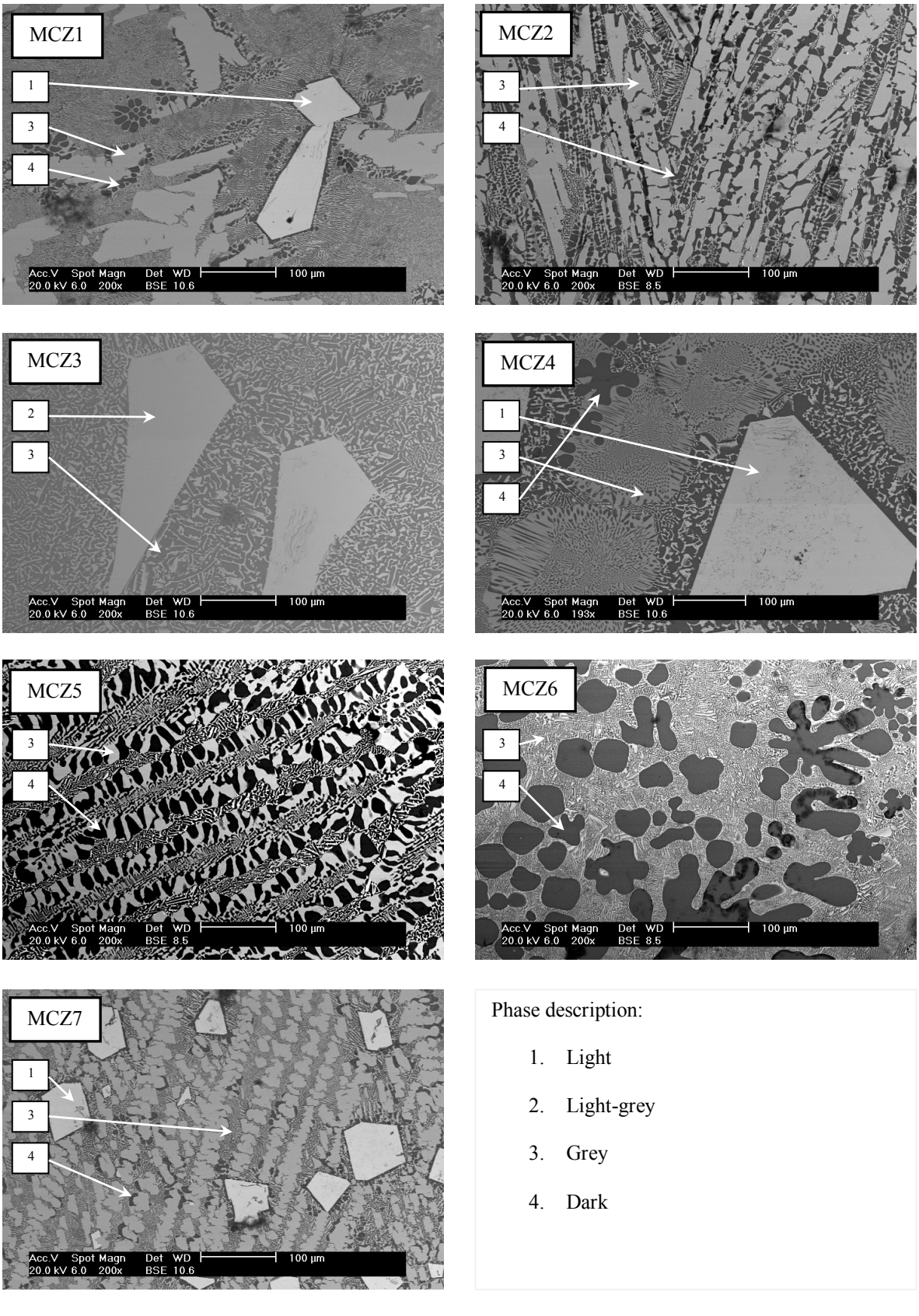

Figure 4.6 SEM backscattered electron images showing the microstructures of Mg-Cu-Zn as-cast final alloys at magnification x200.

ID.	Composition (at. %)	Element	Light phase	Light-grey phase	Grey phase	Dark phase
MCZ1	$Mg_{78}Cu_{14}Zn_8$	Mg	36.51 (17.85)	-	64.13 (40.56)	98.26 (95.50)
		Cu	34.88 (44.55)	-	32.72 (54.08)	0.53 (1.36)
		Zn	28.61 (37.60)	-	3.15 (5.35)	1.20 (3.14)
MCZ2	$Mg_{78}Cu_{19}Zn_3$	Mg	-	-	64.88 (41.37)	98.34 (95.72)
		Cu	-	-	33.29 (55.49)	0.93 (2.37)
		Zn	-	-	1.83 (3.13)	0.73 (1.90)
MCZ3	$Mg_{78}Cu_9Zn_{13}$	Mg	-	0 (0)	-	97.30 (93.15)
		Cu	-	47.81 (47.10)	-	1.25 (3.12)
		Zn	-	52.19 (52.90)	-	1.45 (3.73)
MCZ4	$Mg_{73}Cu_{14}Zn_{13}$	Mg	36.00 (17.52)	-	69.67 (46.56)	98.62 (96.38)
		Cu	33.59 (42.71)	-	20.91 (36.52)	0 (0)
		Zn	30.40 (39.77)	-	9.42 (16.92)	1.38 (3.62)
MCZ5	$Mg_{83}Cu_{14}Zn_3$	Mg	-	-	63. 98 (40.40)	99.32 (98.18)
		Cu	-	-	32.33 (53.35)	0 (0)
		Zn	-	-	3.68 (6.25)	0.68 (1.82)
MCZ6	$Mg_{83}Cu_9Zn_8$	Mg	-	-	66.75 (43.35)	98.51 (96.12)
		Cu	-	-	28.77 (48.83)	0.37 (0.94)
		Zn	-	-	4.48 (7.82)	1.12 (2.93)
MCZ7	$Mg_{73}Cu_{19}Zn_8$	Mg	40.45 (20.45)	-	65.11 (41.59)	98.10 (95.11)
		Cu	36.64 (48.41)	-	31.58 (52.72)	0.80 (2.02)
		Zn	22.91 (31.14)	-	3.31 (5.69)	1.10 (2.87)

Table 4.6 EDS analysis revealing the atomic and (weight) percentages of elements present in the different phases of the as-cast Mg-Cu-Zn alloy microstructures.

4.2.1.3 Mg-Zn-Sm alloys

Figure 4.7 shows typical backscattered electron (BSE) micrographs of the Mg-Zn-Sm as-cast alloys. Observation of the microstructures reveals that multiple phases coexist in these alloys. However, some phases exist in some of the alloys but are not present in the microstructures of others.

According to the EDS analysis (data listed in Table 4.7) and with reference to the ternary phase diagram of the Mg-Zn-Sm system, it is believed the solidification reaction process for alloys MZS1 and MZS3 is the following:

Liquid → Mg + liquid → Mg + Mg_7Zn_3 + $Mg_{10}SmZn_5$.

According to the EDS analysis, it can be assumed that the light-grey phase observed in the as-cast images for these alloys is $Mg_{10}SmZn_5$. In addition, Mg_7Zn_3 and Mg may be attributed to the grey and dark phases, respectively.

As alloy MZS2 is located within a different phase field on the ternary phase diagram, following interpretation of the EDS analysis, it has been deduced that the solidification reaction process for this particular alloy is the following:

Liquid → $Mg_{10}SmZn_5$ + liquid → Mg + Mg_7Zn_3 + $Mg_{10}SmZn_5$.

Further interpretation of the EDS analysis and with reference to the ternary phase diagram of the Mg-Zn-Sm system, it is believed the solidification reaction process for the remaining MZS4 and MZS5 alloys is the following:

Liquid → Mg_3SmZn_6 + liquid → Mg + Mg_7Zn_3 + $Mg_{10}SmZn_5$.

Inspection of the microstructures reveals that a dark phase is present in all of the alloys. According to the EDS analysis, this phase is Mg-rich with Mg content exceeding 96 at. %. This phase contains no Sm content, which explains why it appears dark in BSE imaging mode. Interestingly, despite alloys MZS2 and MZS5

having the same Mg content of 69 at. %, the higher Sm content and reduced Zn content in alloy MZS5 produces a larger amount of the light phase present in the microstructure. Similarly, MZS1 and MZS4 have the same Mg content of 74 at. %. However, MZS4 has a lower Zn content again producing an increase in the amount of light phase present in the microstructure. Continued observation identifies a dark dentritic phase present in the microstructures of alloys MZS1 and MZS3. Although these alloys contain the same Sm content of 4 at. %, the higher Mg content present in alloy MZS3 produces a larger quantity of the dark phase.

In summary, an increase in Mg content increases the dendritic dark phase present in the microstructures of these alloys. Furthermore, a reduction in Zn content appears to increase the large dendritic light phase. What's more, the reduction in Sm content appears to increase the percentage of grey phase present within the microstructure. In addition to quantifying the proportion of individual elements within the different phases of the alloy microstructures, EDS analysis indicates that the overall chemical composition is nearly identical to the designed nominal composition of the alloys.

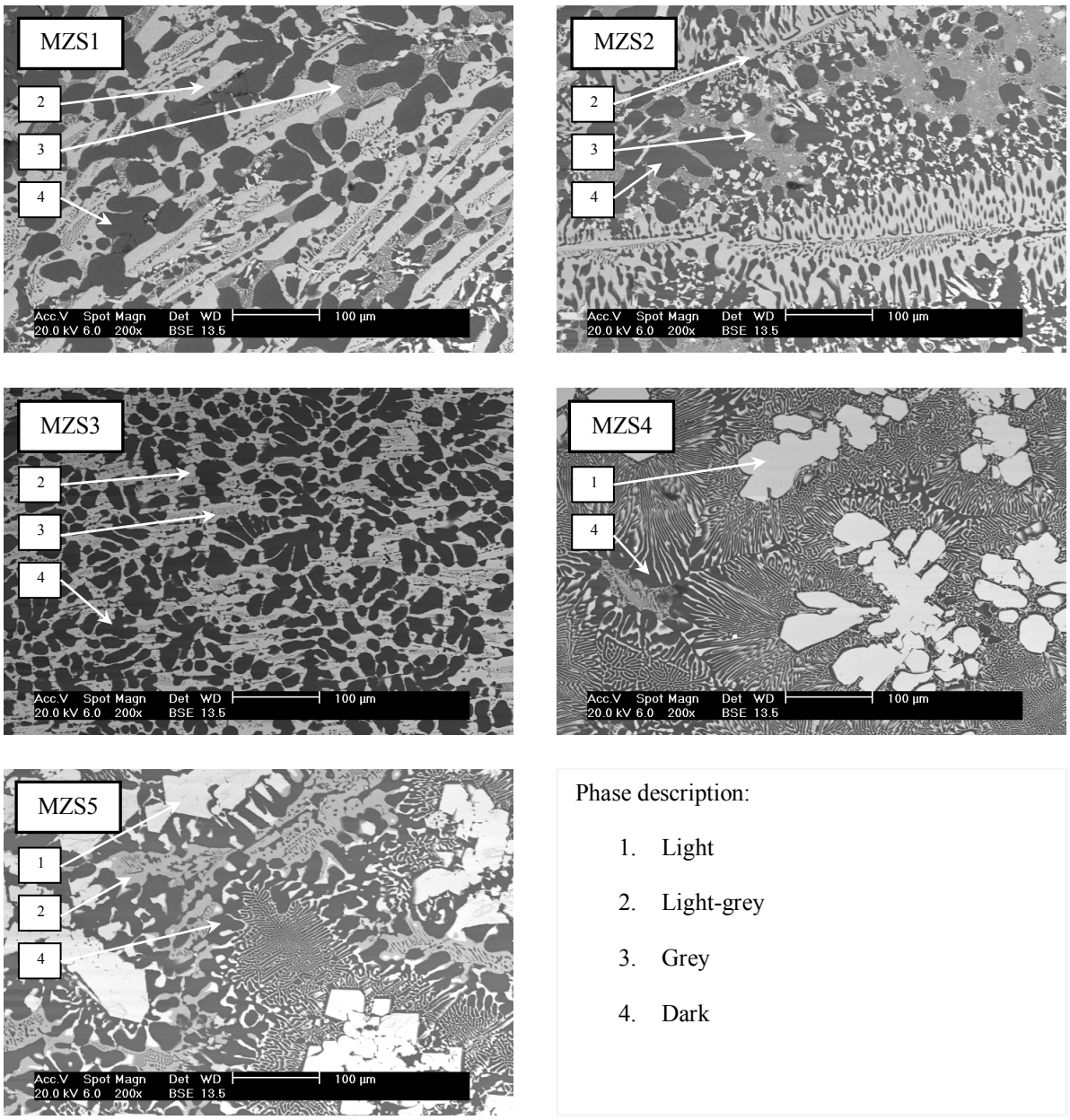

Figure 4.7 SEM backscattered electron images showing the microstructures of Mg-Zn-Sm as-cast final alloys at magnification x200.

ID.	Composition (at. %)	Element	Light phase	Light-grey phase	Grey phase	Dark phase
MZS1	$Mg_{74}Zn_{22}Sm_4$	Mg	-	60.44 (32.19)	73.79 (50.96)	97.10 (92.57)
		Zn	-	33.58 (48.09)	26.06 (48.39)	2.90 (7.43)
		Sm	-	5.98 (19.71)	0.15 (0.65)	0 (0)
MZS2	$Mg_{69}Zn_{27}Sm_4$	Mg	-	57.69 (30.10)	70.16 (46.65)	96.63 (91.43)
		Zn	-	36.51 (51.21)	29.84 (53.35)	3.37 (8.57)
		Sm	-	5.79 (18.69)	0 (0)	0 (0)
MZS3	$Mg_{79}Zn_{17}Sm_4$	Mg	-	62.08 (33.74)	72.01 (44.41)	97.44 (93.41)
		Zn	-	32.22 (47.08)	23.72 (39.34)	2.56 (6.59)
		Sm	-	5.71 (19.18)	4.26 (16.26)	0 (0)
MZS4	$Mg_{74}Zn_{17}Sm_9$	Mg	31.96 (10.68)	-	-	97.50 (93.56)
		Zn	43.92 (39.46)	-	-	2.50 (6.44)
		Sm	24.13 (49.86)	-	-	0 (0)
MZS5	$Mg_{69}Zn_{22}Sm_9$	Mg	28.72 (9.39)	60.54 (32.26)	-	97.45 (93.42)
		Zn	46.88 (41.23)	33.46 (47.94)	-	2.55 (6.58)
		Sm	24.41 (49.38	6.01 (19.80)	-	0 (0)

Table 4.7 EDS analysis revealing the atomic and (weight) percentages of elements present in the different phases of the as-cast Mg-Zn-Sm alloy microstructures.

4.3 Rapidly solidified alloys

4.3.1 Microstructure

The considerably higher cooling rate of water-cooled Cu mould casting can produce microstructure different from the structure of the as-cast alloys under slow-cooling solidification conditions. Figure 4.8 shows the outer surface appearance and the cross-sectional surface used for characterisation of a typical cast alloy. The appearance of the casting indicates that the melt was not uniformly injected into the Cu-mould. This may be a result of poor mould design leading to the melt solidifying in the centre of the cavity. Nevertheless, a wedge-shaped cross-section could still be obtained for characterisation.

Figure 4.8 Outer surface appearance of a typical cast alloy. The cross-sectional surface used for characterisation of the alloy is shown.

Since the narrow section of the wedge was exposed to a higher cooling rate, it was decided to use this particular part of the cast alloy for XRD and DSC characterisation.

4.3.1.1 Mg-Cu-Y alloys

Figure 4.9 shows typical BSE micrographs of the Mg-Cu-Y rapidly solidified alloys. Observations reveal the microstructure of the alloys MCY1, MCY2, MCY3, MCY4, and MCY7 display featureless matrices with crystallite traces. The size and volume fraction of the primary phases are small. The effects of water-cooled casting on the phase selection and microstructure refinement are not surprising. The high cooling rate can retard the nucleation and growth of crystallite phase. These small crystallites may be formed on cooling of the highly quenched amorphous matrix.

In contrast, the entire cross-section of alloys MCY5 and MCY6 are fully crystalline. Agglomerates of dendrites approximately 50-75 μm in size are dispersed in the microstructures.

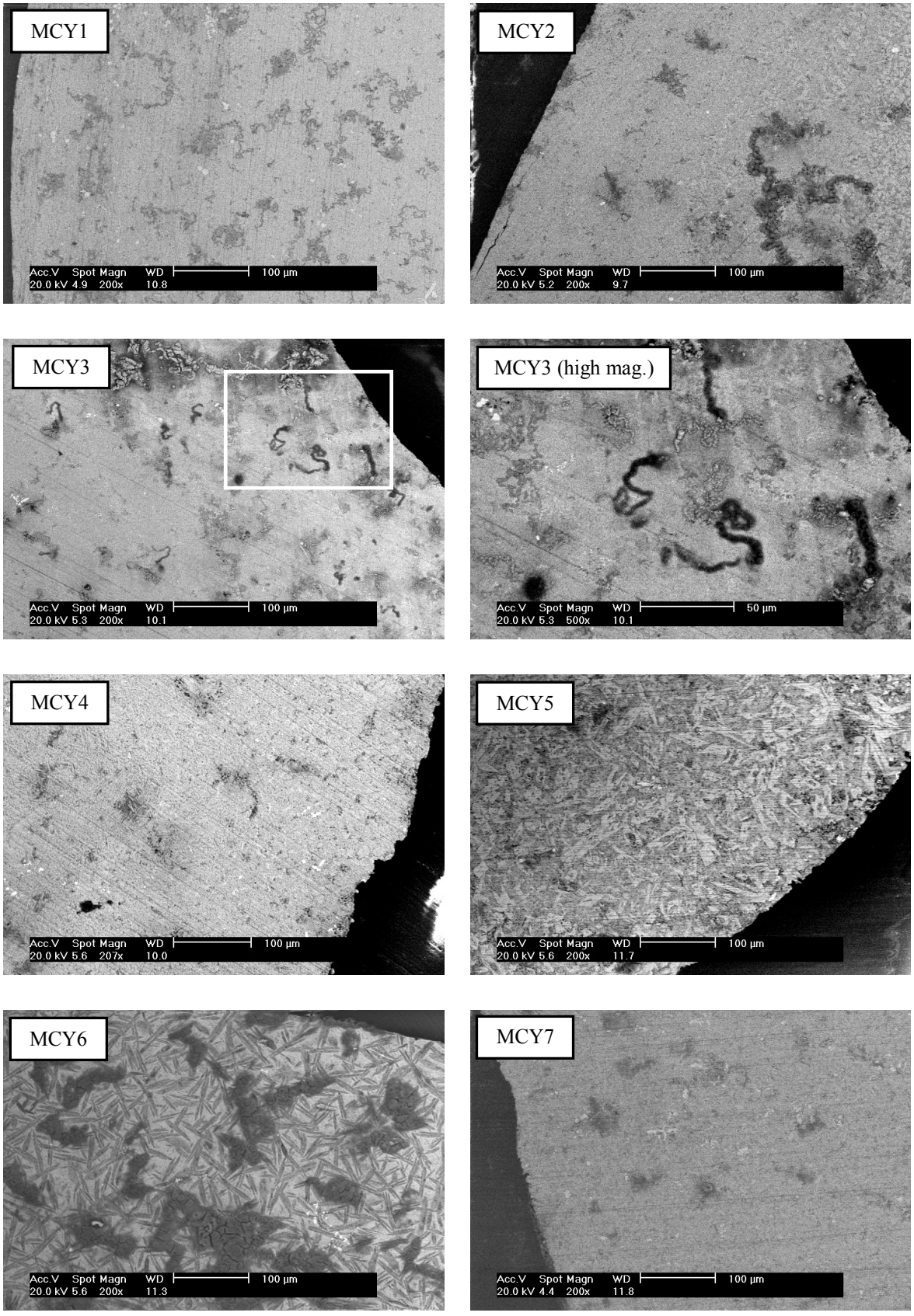

Figure 4.9 SEM backscattered images of rapidly solidified Mg-Cu-Y alloys.

4.3.1.2 Mg-Cu-Zn alloys

Figure 4.10 shows the typical BSE micrographs of the Mg-Cu-Zn rapidly solidified alloys. Observations reveal similarities in the microstructures between particular alloys within this ternary system. The microstructure of alloys MCZ1, MCZ2, MCZ4, and MCZ5 are closely related.

Of particular interest is alloy MCZ3. The observed microstructural features suggest a predominantly featureless glassy phase embedded in a crystalline matrix. Closure inspection reveals small crystalline particles (approx. 5 μm) dispersed within the glassy phase. In contrast, the entire cross-section of alloys MCZ6 and MCZ7 are fully crystalline.

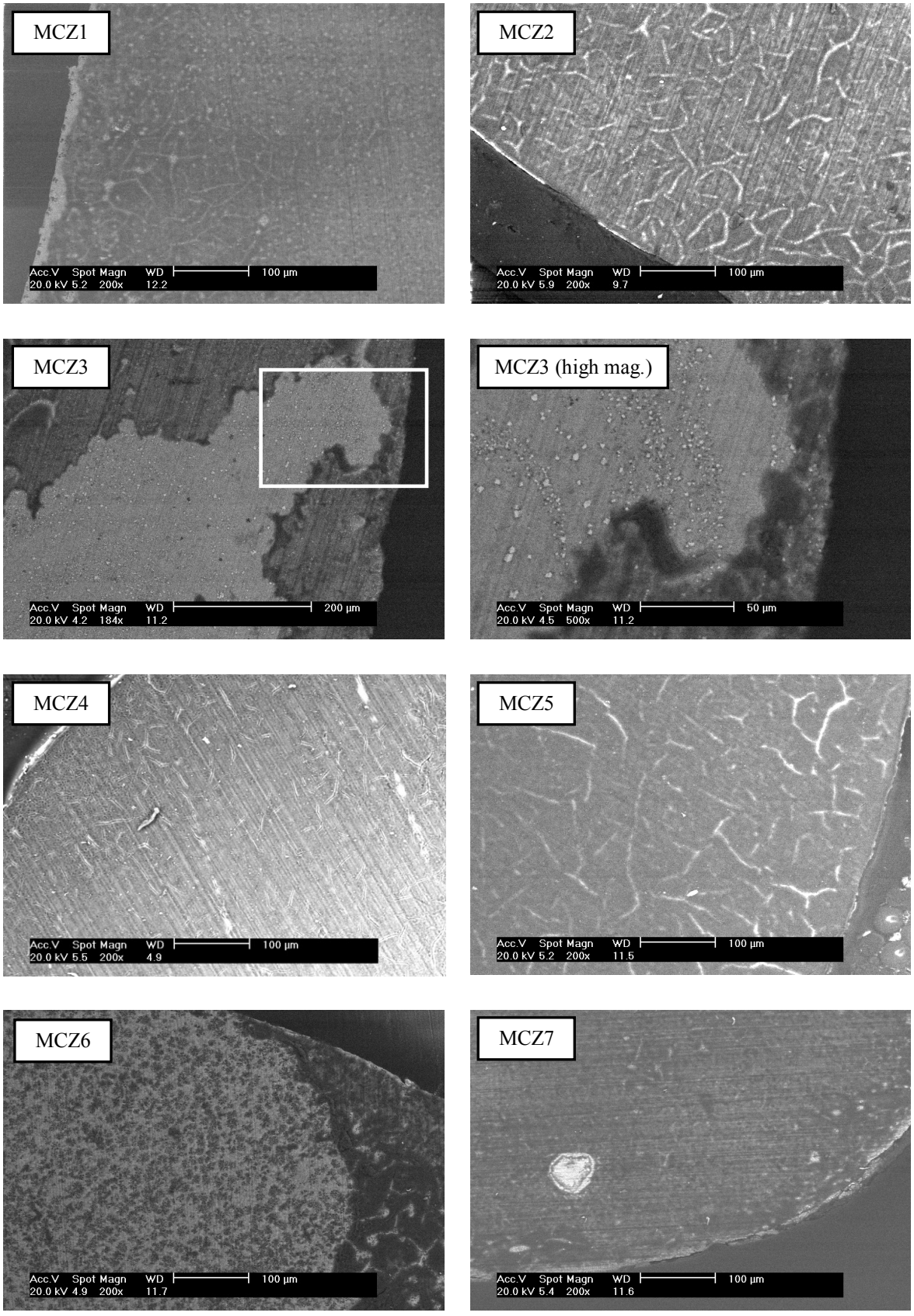

Figure 4.10 SEM backscattered images of rapidly solidified Mg-Cu-Zn alloys.

4.3.1.3 Mg-Zn-Sm alloys

The cross-sectional microstructures of the Mg-Zn-Sm rapidly solidified alloys are shown in Figure 4.11. Of particular interest are alloys MZS1, MZS4, and MZS5. It is well known that the cooling rate decreases from the surface towards the centre of the cast alloy. That is to say, a mostly glassy structure is expected to form near the Cu mould surface due to the higher cooling rate realised close to the mould, and crystalline phases should appear towards the centre of the specimen. High magnification of microstructural features suggests predominantly featureless glassy microstructures at the surfaces with crystalline particles towards the centre of the cast alloys, which is what one should expect. In contrast, observation of the cross-sections of alloys MZS2 and MZS3 indicate crystalline phases are present with no differences found in the overall microstructures.

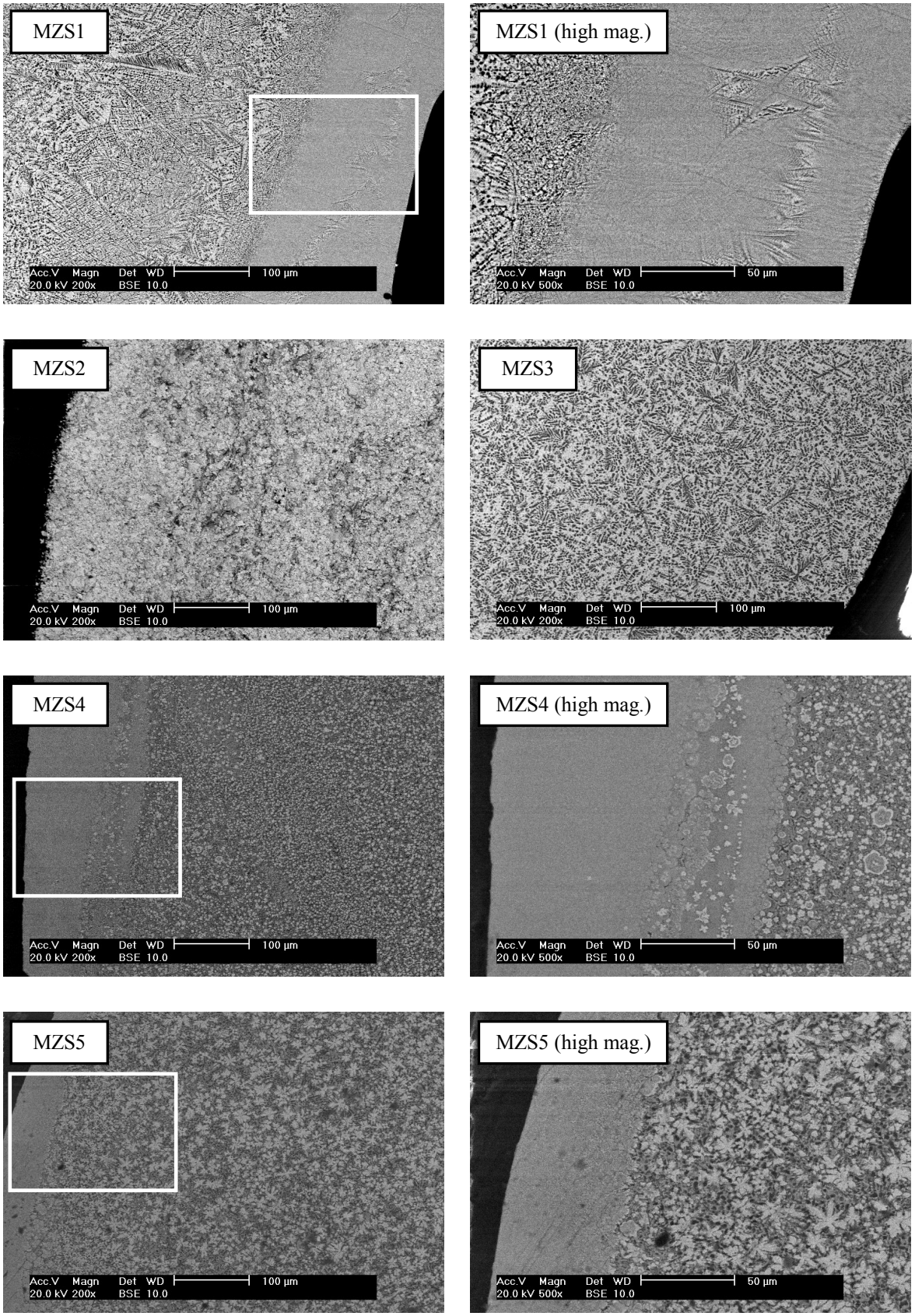

Figure 4.11 SEM backscattered images of rapidly solidified Mg-Zn-Sm alloys.

4.3.2 X-ray diffraction

Due to time constraints, the decision was taken to perform XRD on a select number of alloys. Based on evidence obtained through SEM characterisation, the alloys that displayed a clear indication of an amorphous phase present in the microstructure were characterised using XRD. In addition, some alloys that contained crystalline phases were also characterised in order to help identify these phases. Consequently, the alloys characterised using XRD included:

- MCY1
- MCY2
- MCY3
- MCY6
- MCY7
- MCZ3
- MCZ4
- MCZ7
- MZS1
- MZS2
- MZS4

4.3.2.1 Mg-Cu-Y alloys

Figure 4.12 displays the XRD traces for a selection of the MCY alloys. As the samples were mounted in resin prior to analysis, a reference pattern is also displayed (blue trace) to identify any peaks corresponding to this resin material. The trace of the MCY1 alloy shows a broad peak in the 2θ range of 30-40º characteristic of an amorphous phase, with no crystalline phases detected within the sensitivity limits of XRD. This indicates that this alloy has a larger glass-forming ability than the other compositions. When the alloy composition fluctuates away from the eutectic, however, crystalline phases are observed in all cases.

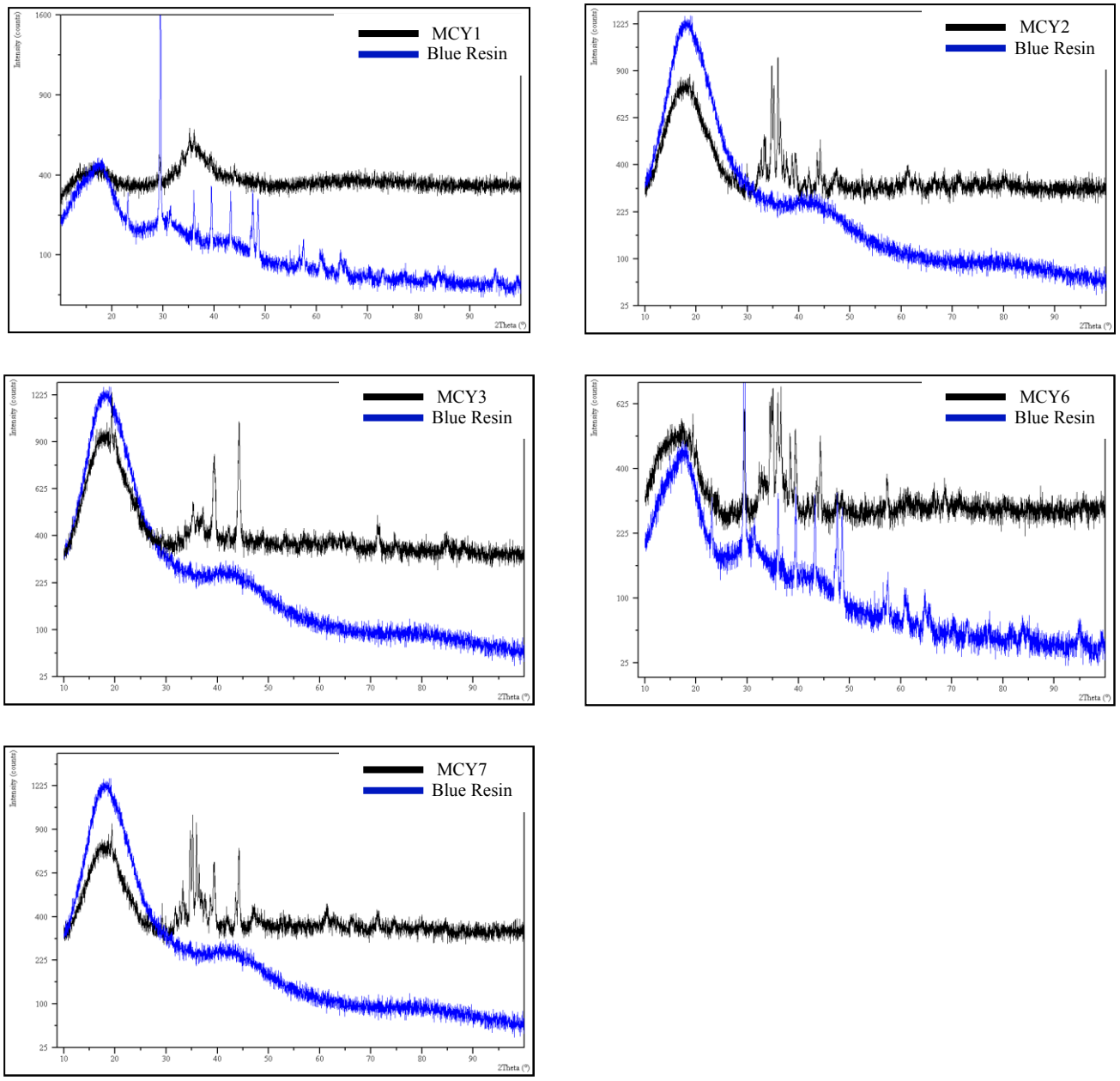

Figure 4.12 XRD traces showing a broad peak for the MCY1 alloy, indicating the presence of an amorphous phase. The remaining MCY alloys appear to show varying degrees of crystallinity.

4.3.2.2 Mg-Cu-Zn alloys

Figure 4.13 displays the XRD traces for a selection of the MCZ alloys. Again, a reference pattern is also displayed (blue trace) to identify any peaks corresponding to the mounting resin. It is obvious that all of the rapidly solidified alloys exhibit crystalline phases in their corresponding microstructures. Thus, it can be concluded that amorphisation seems to be impossible under the present processing conditions.

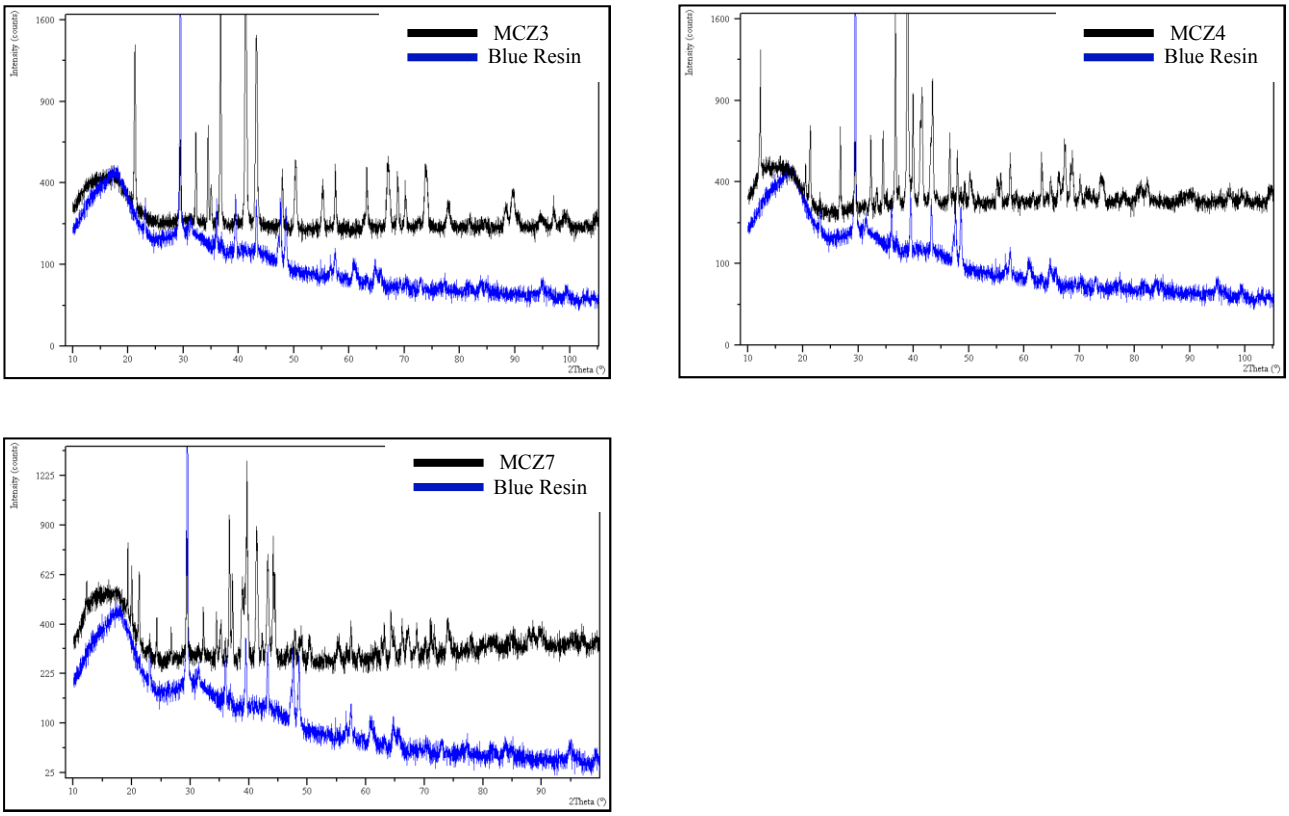

Figure 4.13 XRD traces of the MCZ alloys.

4.3.2.3 Mg-Zn-Sm alloys

Figure 4.14 displays the XRD traces for a selection of the MZS alloys along with a reference pattern (blue trace) to identify any peaks corresponding to the mounting resin. As can be seen, sharp crystalline peaks are visible in the XRD traces. Despite

rapid cooling, this evidence suggests that these alloys have poor glass-forming ability and that varying the composition has little effect on reducing the presence of crystals in the microstructures. However, since observations of the SEM backscattered images, shown in section 4.3.1.3, identify an amorphous phase present in the microstructures of alloys MZS1 and MZS4, this indicates a noticeable discrepancy in the results. It could be suggested that this inconsistency in the results might be because the amorphous phase is too small to identify using XRD, thus not showing on any of the traces.

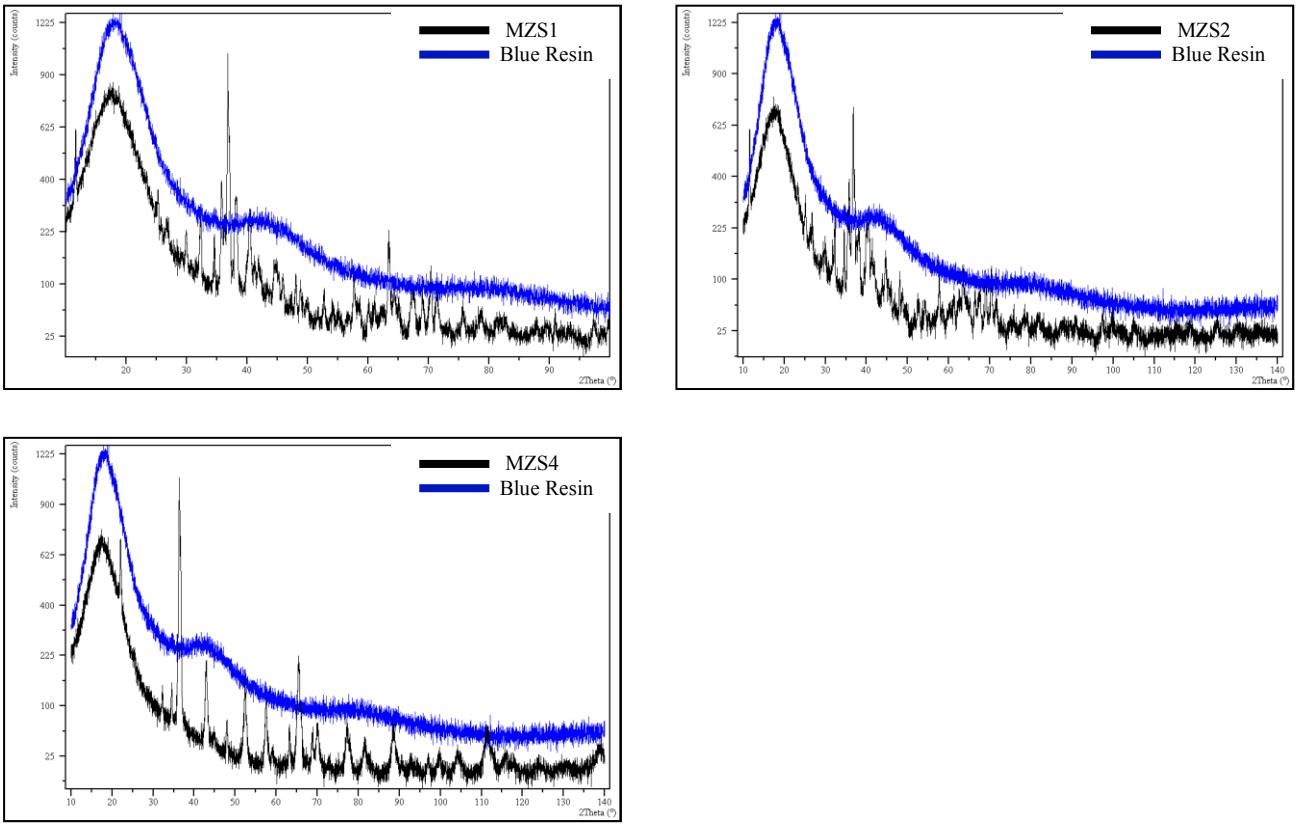

Figure 4.14 XRD traces of the MZS alloys.

4.3.3 Thermal analysis

Again, due to time constraints, the decision was taken to perform thermal analysis on a select number of alloys. This decision was based on evidence obtained through SEM and XRD characterisation. The alloys that displayed an indication of an amorphous phase present in the microstructure were characterised using DSC. These included:

- MCY1
- MCY3
- MCZ1
- MZS1
- MZS4
- MZS5

4.3.3.1 Mg-Cu-Y alloys

Figure 4.15 shows the DSC traces of the rapidly solidified alloys MCY1 and MCY3. Observation of these traces reveals remarkably similar features. The traces express a clear endothermic event associated with glass transition and a distinct super-cooled liquid region, followed by an exothermic event (characteristic of crystallisation process), which is split into two peaks.

Table 4.8 summarises the thermal stability of all the alloys analysed using DSC. It is obvious that the glass transition temperature, T_g, onset crystallisation temperature, T_x, and liquidus temperature, T_l, raise with increasing Y content. Furthermore, the total enthalpy of the crystallisation, ΔH_x, obtained by integrating the areas under all the exothermic peaks, was also significantly higher for alloy MCY1.

Table 4.8 also lists the values of some additional thermodynamic parameters used to quantify glass-forming ability. Both alloys display remarkably similar values for the reduced glass-transition temperature, T_{rg}, and γ parameter. However, the width of the super-cooled liquid region is considerably improved for MCY1.

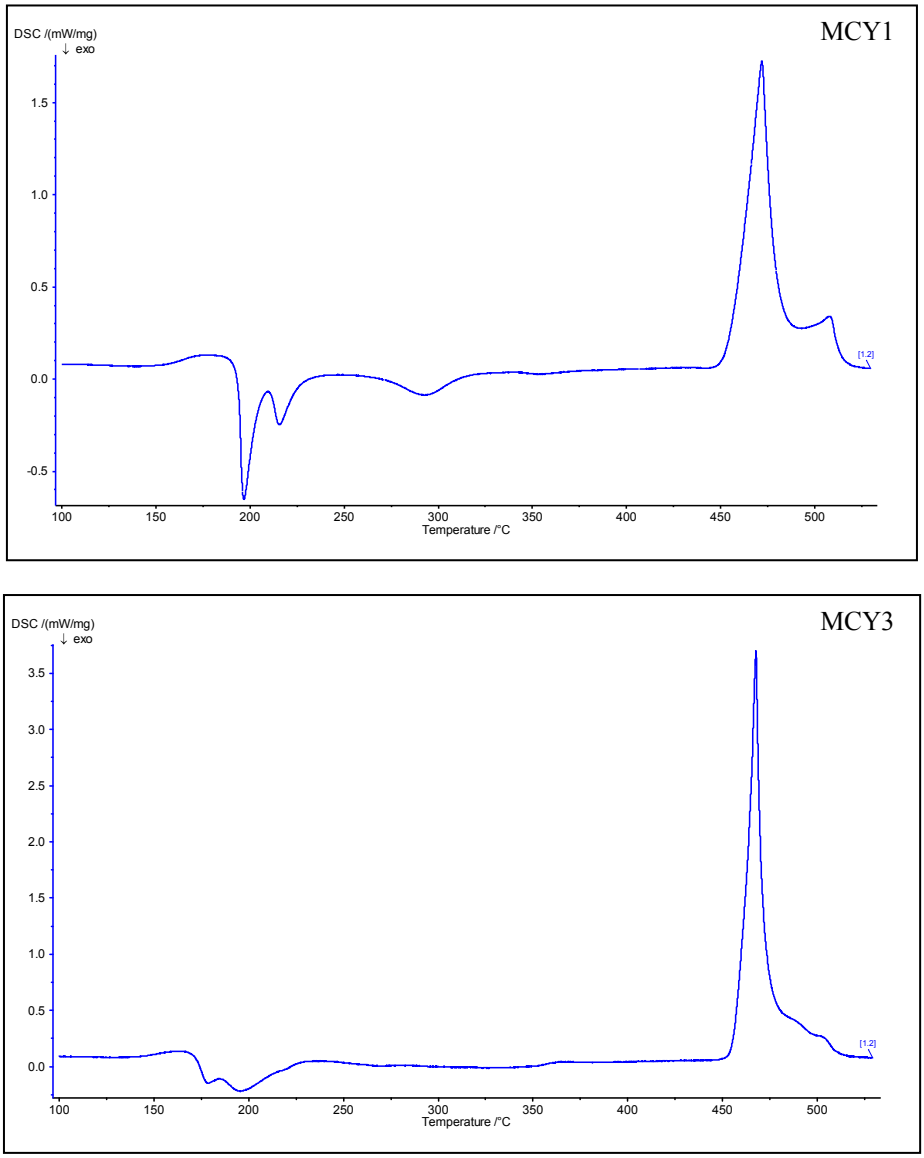

Figure 4.15 DSC traces of the rapidly solidified alloy MCY1 and MCY3.

4.3.3.2 Mg-Cu-Zn alloys

Examination of the DSC trace of the MCZ1 alloy (shown in Figure 4.16) revealed no glass transition. One can deduce from the endothermic peak due to melting that the MCZ1 alloy is very close to the eutectic temperature. The onset melting temperature, T_m, and liquidus temperature, T_l, were determined to be 455 and 498 °C, respectively.

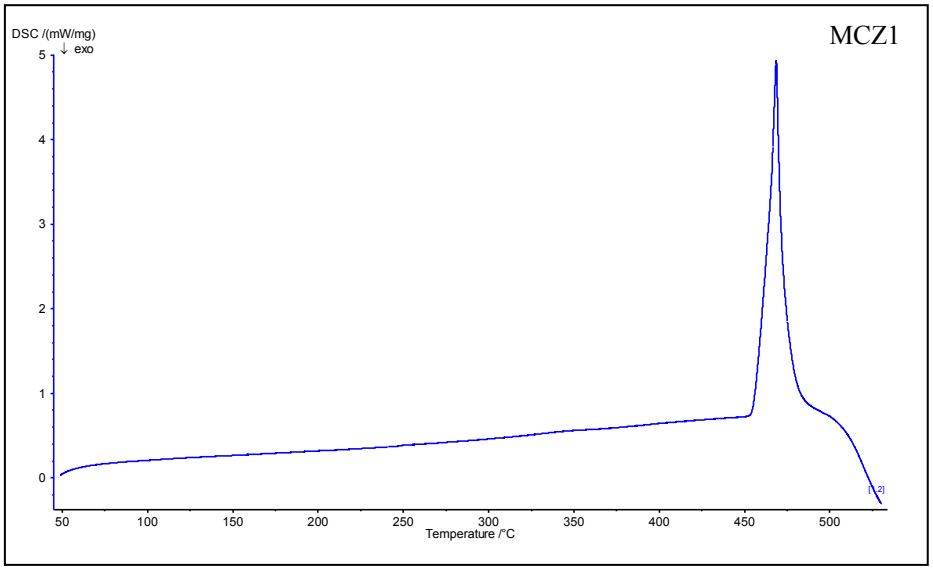

Figure 4.16 DSC traces of the rapidly solidified alloy MCZ1.

4.3.3.3 Mg-Zn-Sm alloys

The thermal stability of the selected MZS alloys was examined by differential scanning calorimetry and the results are displayed in Figure 4.17. Endothermic peaks due to melting are seen for all alloys. The DSC trace of MZS1 consists of small and large endothermic peaks at temperatures of 344 °C and 443 °C, respectively. The small endothermic peak may be due to dissolution of the solid phase and the large endothermic peak a result of the melting of the eutectic mixture. However, the DSC trace of MZS5 consists of two endothermic peaks at temperatures of 446 °C and 510 °C indicating the initial melting of the eutectic mixture and subsequent melting of the primary phase.

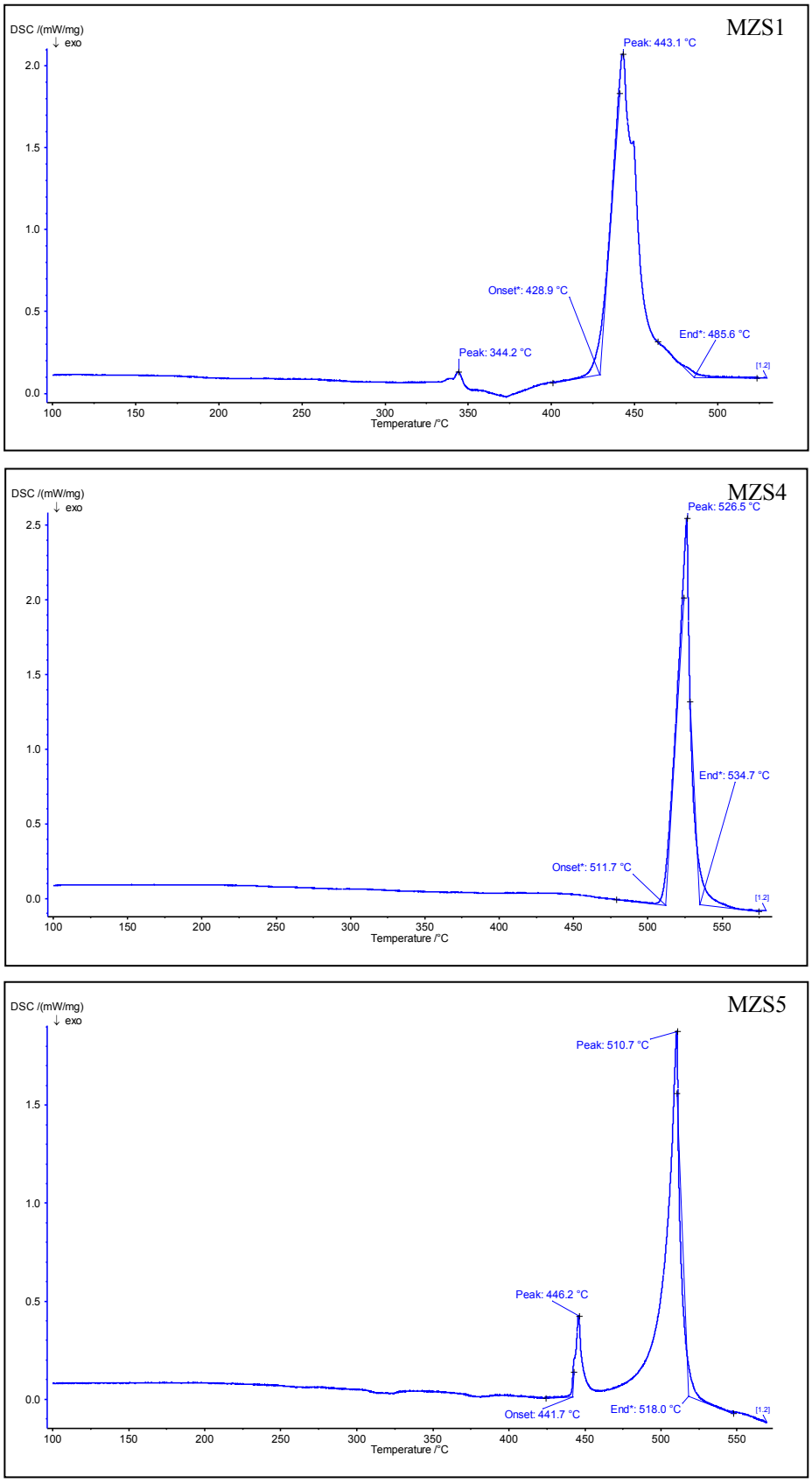

Figure 4.17 DSC traces of the rapidly solidified alloys MZS1, MZS4, and MZS5.

ID.	Composition (at. %)	T_g °C (K)	T_x °C (K)	T_m °C (K)	T_l °C (K)	T_{rg}	ΔT_x	γ	ΔH_1 (J/g)	ΔH_2 (J/g)	ΔH_3 (J/g)	Total ΔH
MCY1	$Mg_{60}Cu_{22}Y_{18}$	152 (425)	194 (467)	456 (729)	514 (787)	0.54	42	0.39	39.56	17.12	20.45	77.13
MCY3	$Mg_{60}Cu_{27}Y_{13}$	141 (414)	165 (438)	461 (734)	511 (784)	0.53	24	0.37	15.93	38.41	-	54.34
MCZ1	$Mg_{78}Cu_{14}Zn_8$	-	-	455 (728)	498 (771)	-	-	-	-	-	-	
MZS1	$Mg_{74}Zn_{22}Sm_4$	-	-	429 (702)	486 (759)	-	-	-	-	-	-	
MZS4	$Mg_{74}Zn_{17}Sm_9$	-	-	512 (785)	535 (808)	-	-	-	-	-	-	
MZS5	$Mg_{69}Zn_{22}Sm_9$	-	-	442 (715)	518 (791)	-	-	-	-	-	-	

Table 4.8 Thermal stability of rapidly solidified alloys (heating rate: 10 K/min).

4.4 Mechanical properties

4.4.1 Hardness

4.4.1.1 Rapidly solidified alloys

Table 4.9 displays the hardness values of the Mg-Cu-Y, Mg-Cu-Zn, and Mg-Zn-Sm alloys. Measurements were taken from the edge towards the centre of the alloys to investigate whether any differences in mechanical properties occur throughout the microstructures of the rapidly solidified alloys. The results are graphically presented for the rapidly solidified MCY, MCZ, and MZS alloys in Figures 4.18, 4.19 and 4.20, respectively.

The hardness values for the Mg-Cu-Y alloys vary quite considerably. The MCY1 alloy recorded the highest average hardness value of 495.3 HV_{1KG}. In contrast, alloy MCY6 attained the lowest average with a value of 229.6 HV_{1KG}. However, the graphical representation of the hardness values for the MCY alloys suggests that the mechanical properties are inconsistent throughout the related microstructures. This supports the SEM characterisation, which indicated a clear difference in microstructure for at least some of the alloys. One might expect to observe higher hardness near the edge of the specimen, as this may indicate an amorphous phase present in the microstructure. However, despite some of the MCY alloys having higher hardness values towards the edge of the specimen compared with the values recorded at the centre of the sample, the difference is negligible and, therefore, cannot be confirmed as being an improvement in mechanical hardness. Nevertheless, the lack of confirmation may be attributed to the fact that the diameter of the diamond indenter was larger than any apparent glassy phase located at the edge of some of the samples.

The MCZ plot highlights the significant variation in mechanical hardness between each of the alloys, which is quite remarkable considering only slight compositional change. The MCZ4 alloy recorded the highest average hardness value of 345.2 HV_{1KG}. In contrast, alloy MCZ5 attained the lowest average with a value of 170.6 HV_{1KG}. In the same way, the MZS plot also identifies the dissimilarity between each of the alloys in terms of mechanical hardness. However, there will always be

inaccuracies in hardness measurement. The hardness at the edge may be less accurate if the distance from the edge of the sample to where the indentation is made is less than the thickness of the sample. This is because in these circumstances, the sample could deform plastically as there may be insufficient material to constrain the indentation.

ID.	Composition (at. %)	Hardness (HV_{1KG}) Edge → Centre							Average (HV_{1KG})
MCY1	$Mg_{60}Cu_{22}Y_{18}$	437.1	549.6	545.6	464.6	490.3	483.0	497.2	495.3
MCY2	$Mg_{60}Cu_{17}Y_{23}$	301.2	466.1	499.6	435.9	449.9	466.7	427.8	435.3
MCY3	$Mg_{60}Cu_{27}Y_{13}$	394.8	284.9	385.0	402.6	396.4	480.1	335.1	382.7
MCY4	$Mg_{65}Cu_{22}Y_{13}$	512.5	522.3	307.5	442.5	498.1	376.8	463.2	389.0
MCY5	$Mg_{55}Cu_{22}Y_{23}$	389.2	393.9	472.1	421.7	451.0	398.7	404.2	418.7
MCY6	$Mg_{65}Cu_{17}Y_{18}$	218.8	192.6	219.4	243.4	212.9	232.6	287.4	229.6
MCY7	$Mg_{55}Cu_{27}Y_{18}$	421.9	371.6	437.9	365.7	448.8	377.5	401.3	403.5
MCZ1	$Mg_{78}Cu_{14}Zn_{8}$	384.6	297.9	250.7	287.5	297.4	308.4	376.9	314.8
MCZ2	$Mg_{78}Cu_{19}Zn_{3}$	266.0	238.8	182.4	173.2	217.1	239.7	194.3	215.9
MCZ3	$Mg_{78}Cu_{9}Zn_{13}$	209.9	197.0	209.1	184.2	211.1	227.4	193.6	204.6
MCZ4	$Mg_{73}Cu_{14}Zn_{13}$	306.1	298.3	380.1	357.8	394.2	330.1	349.9	345.2
MCZ5	$Mg_{83}Cu_{14}Zn_{3}$	173.4	101.0	214.7	180.6	130.8	203.7	190.3	170.6
MCZ6	$Mg_{83}Cu_{9}Zn_{8}$	241.3	200.8	215.9	221.8	208.7	219.4	252.7	222.9
MCZ7	$Mg_{73}Cu_{19}Zn_{8}$	265.6	268.0	345.1	242.1	289.5	278.7	313.6	286.1
MZS1	$Mg_{74}Zn_{22}Sm_{4}$	239.9	222.9	221.4	246.7	234.6	246.8	253.8	238.0
MZS2	$Mg_{69}Zn_{27}Sm_{4}$	336.9	300.3	337.0	339.4	331.1	294.3	294.3	319.0
MZS3	$Mg_{79}Zn_{17}Sm_{4}$	191.7	194.9	201.7	191.7	198.4	191.8	191.8	194.6
MZS4	$Mg_{74}Zn_{17}Sm_{9}$	191.8	205.5	227.0	251.4	217.7	252.8	219.4	223.7
MZS5	$Mg_{69}Zn_{22}Sm_{9}$	233.6	256.7	243.9	287.5	264.3	262.5	277.4	260.8

Table 4.9 The hardness values of the Mg-Cu-Y, Mg-Cu-Zn, and Mg-Zn-Sm alloys from the edge to the centre of the alloy.

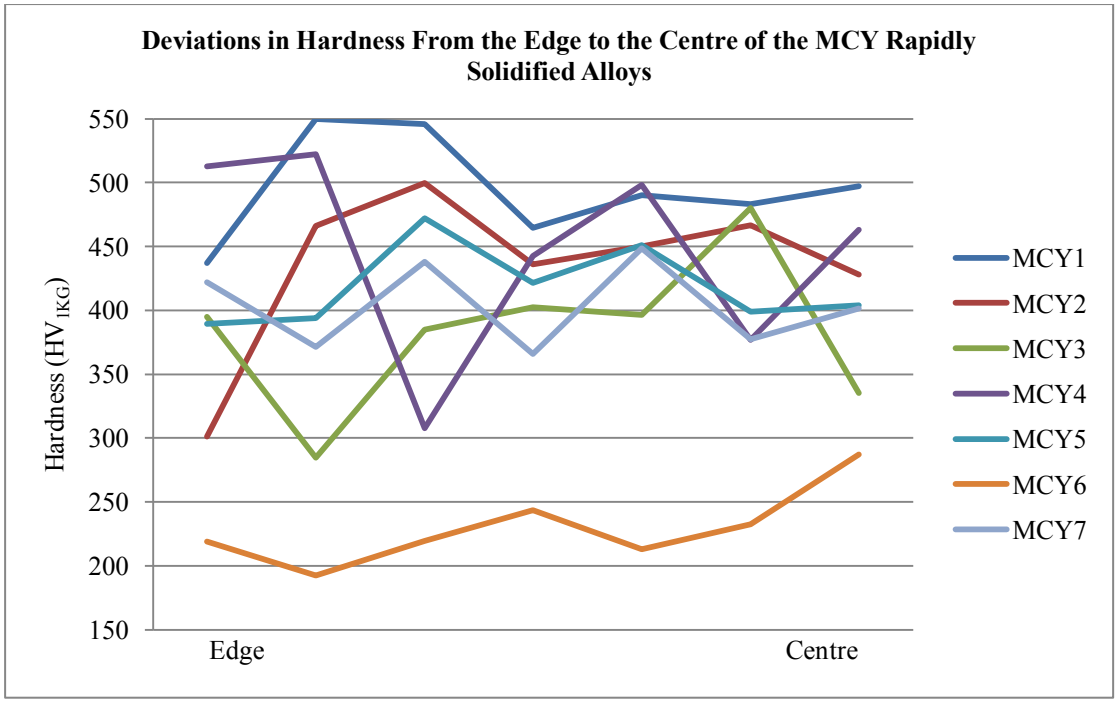

Figure 4.18 Deviations in hardness values across the surface of the MCY rapidly solidified alloys.

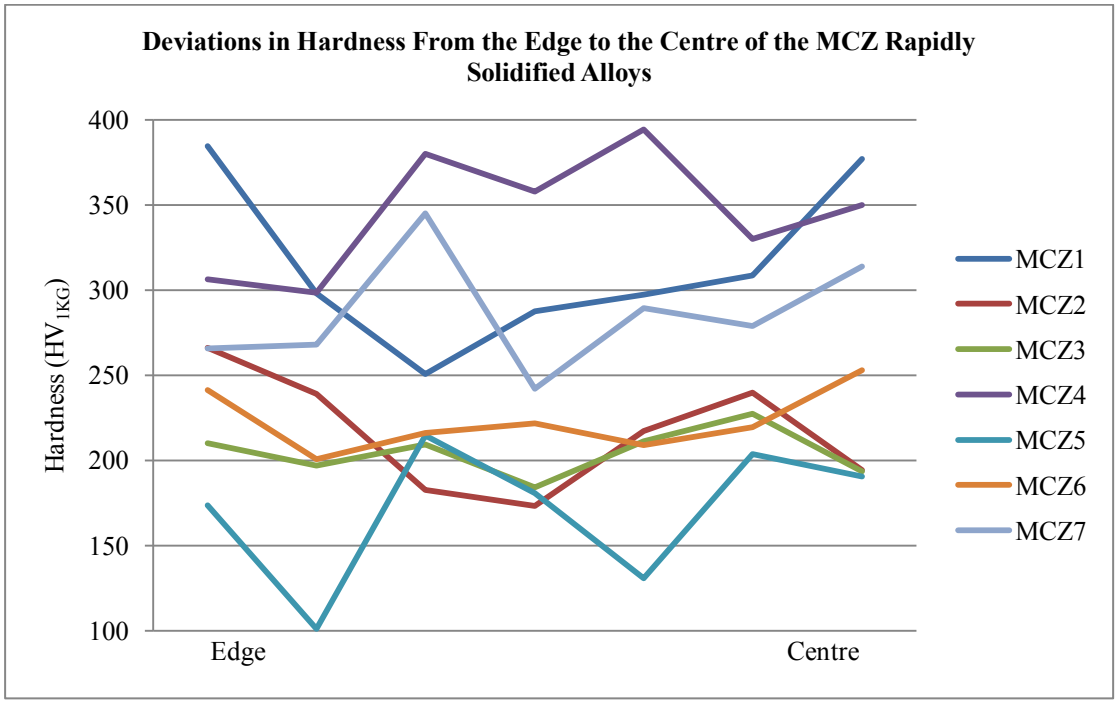

Figure 4.19 Deviations in hardness values across the surface of the MCZ rapidly solidified alloys.

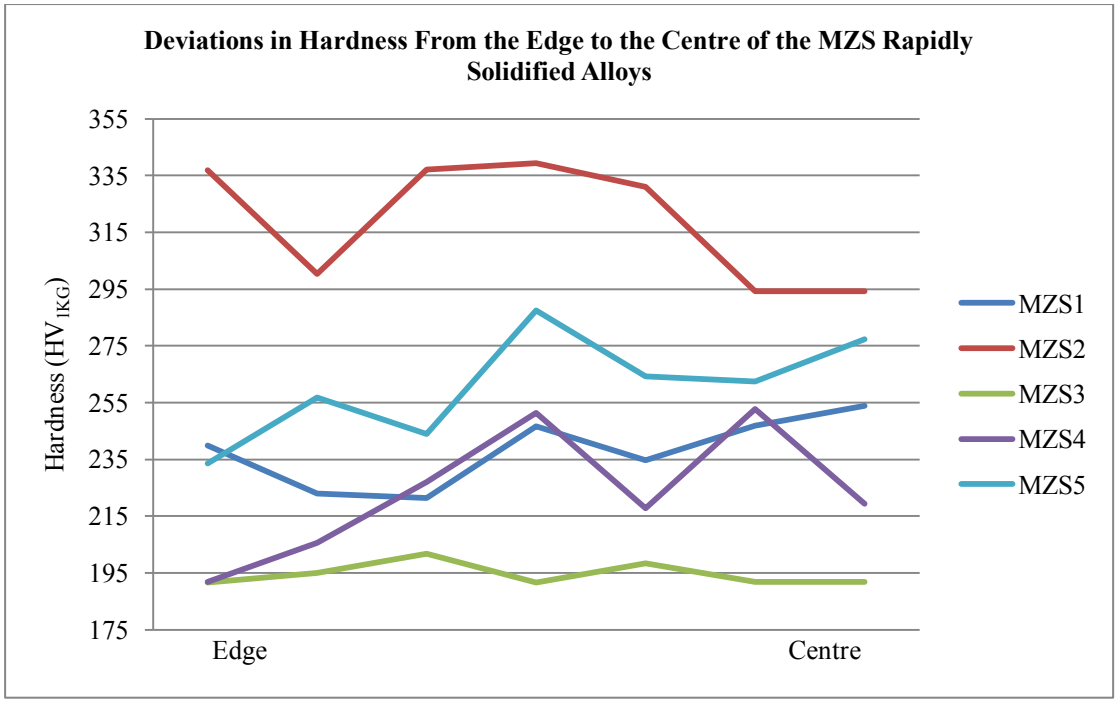

Figure 4.20 Deviations in hardness values across the surface of the MZS rapidly solidified alloys.

The mechanical testing provides evidence of the superior properties of this alloy compared to other Mg alloys. Figure 4.21 displays the average hardness values of the Mg-Cu-Y, Mg-Cu-Zn, and Mg-Zn-Sm rapidly solidified alloys. For comparison, the hardness properties of cast Mg-Al-Zn and wrought Mg-Al-Si alloys are indicated. It is noteworthy that wrought alloys exhibit increased hardness values as they are prepared through 'work hardening' effect, i.e. the flowing stress rises with the increase of strain during deformation. It is suggested that work hardening improves the mechanical properties of the alloy as it can hinder the moving and slipping of the dislocations. Despite this effect, the mechanical properties of the all the designed alloys remain far superior because of a combination of refined microstructure, hard intermetallic phases, and possibly in some instances, an amorphous phase.

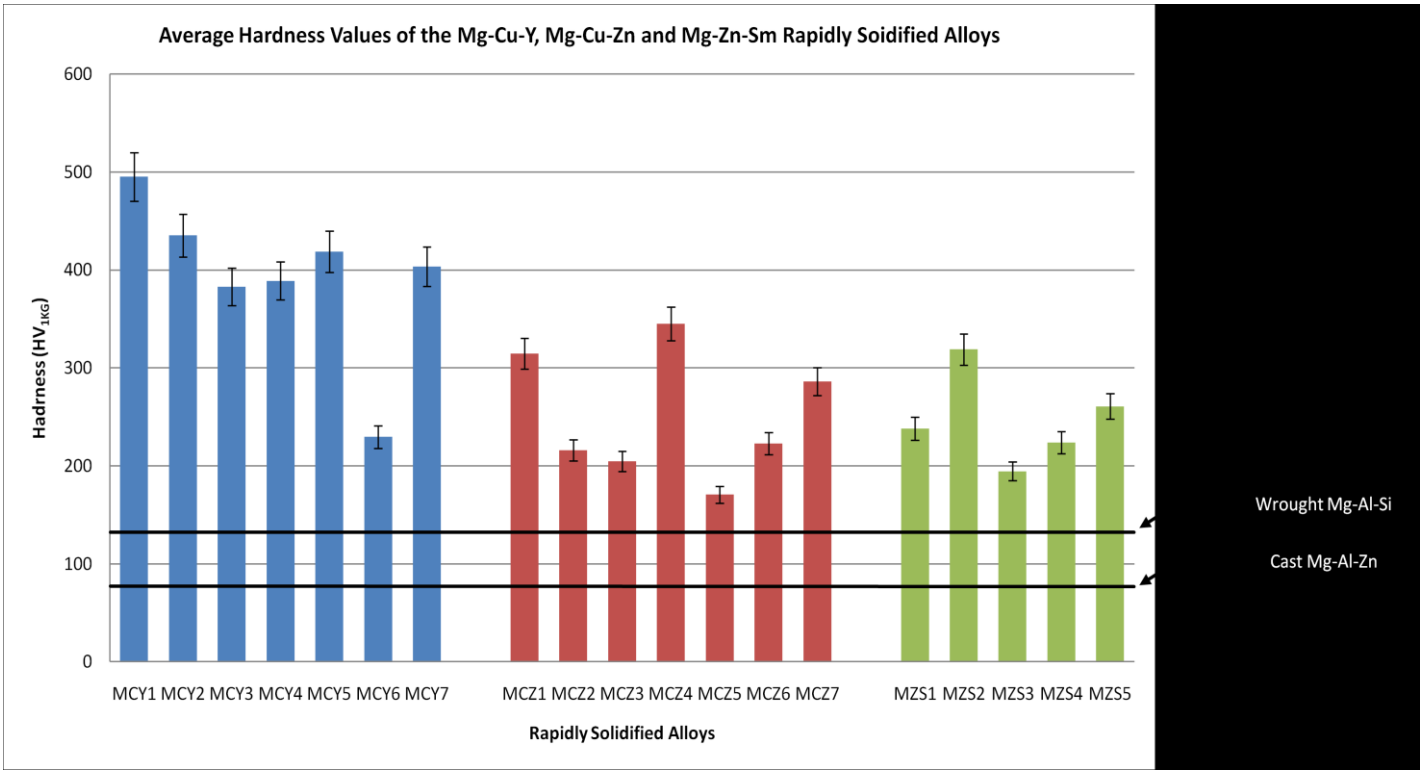

Figure 4.21 Average hardness values of the Mg-Cu-Y, Mg-Cu-Zn, and Mg-Zn-Sm rapidly solidified alloys. Error bars for these alloys are displayed with 5% value. For comparison, the hardness values of two commercial Mg-based alloys are shown.

References

[1] J. Cheney and K. Vecchio, Mater. Sci. Eng., A471(2007)135

[2] D. B. Miracle and O. N. Senkov, Mater. Sci. Eng., A347(2003)50

[3] J. Cheney and K. Vecchio, J. Alloys. Comps., xxx(2008)xxx-xxx

[4] M. Mezbahul-Islam, D. Kevorkov, and M. Medraj, J. Chem. Thermodynamics, 40(2008)1064

CHAPTER 5 DISCUSSION

5.1 The effect of substituting Y with Zn

This report primarily focused on the Mg-Cu-Y ternary system. This particular system has been extensively researched allowing an in-depth analysis of the correlation between existing experimental evidence and theories proposed in this report. Subsequently, the Mg-Cu-Zn system was investigated as this system was found to have low ternary eutectic temperature, which potentially offers GFA. Therefore, direct comparisons are able to be drawn between the two systems with particular consideration given to the effect of substituting Y with Zn on the GFA, thermal, and mechanical properties.

5.1.1 Predicting GFA

5.1.1.1 Empirical rules

According to early methodology for alloy design created by Inoue [1], in order to achieve high GFA for metallic alloys, the following three empirical rules should be satisfied: (1) have a negative mixing enthalpy among constituent elements, (2) contain large atomic size mismatches, and (3) be a multi-component alloy of three or more elements.

(1) Negative mixing enthalpy

The enthalpies of mixing among the major elements at the equiatomic composition, which is an important factor influencing on GFA and stability of the supercooled liquid region, for the Mg-Cu-Y and Mg-Cu-Zn systems, have been calculated with Miedema's semi-empirical method. According to the calculated values displayed in Table 5.1, negative heats of mixing occur between all elements within these systems, thus satisfying the first empirical rule.

	Cu	Mg	Y	Zn
Cu	-	-20	-117	-16
Mg	-20	-	-27	-13
Y	-117	-27	-	N/A
Zn	-16	-13	N/A	-

Table 5.1 The enthalpies of mixing among the elements present in the Mg-Cu-Y and Mg-Cu-Zn ternary systems.

(2) Atomic size mismatches

Inoue et al [2] deduced experimentally, in order to achieve high GFA, metallic alloys must contain atomic size mismatches with optimised ratios of between 12 and 21 %. It is thought that neither too small size ratios nor too big size ratios can construct a highly dense random packed atomic structure, thus restricting GFA. The differences in atomic size ratios between the solvent and the solute elements in the Mg-Cu-Y and Mg-Cu-Zn alloys are presented in Table 5.2.

	Cu	Mg	Y	Zn
Cu	-	20.1	N/A	N/A
Mg	20.1	-	11.1	16.5
Y	N/A	11.1	-	N/A
Zn	N/A	16.5	N/A	-

Table 5.2 Atomic size differences (%) between the solvent and the solute elements in the Mg-Cu-Y and Mg-Cu-Zn alloys.

It is obvious that the atomic radius mismatch between the solvent and solute elements is between 12 and 21 % in all circumstances with the exception of Mg and Y (although the atomic size difference between Mg and Y is 11.1 %, just 0.9 % outside the recommended value of 12 %). The dominant effect of the atomic size differences on the GFA indicates a predominant role of kinetic factor in BMG formation. This is because the appropriate large atomic size difference may induce highly dense packed microstructure and stabilise the supercooled liquid state of the alloy [3], resulting in a dramatic increase in the viscosity of the melt state. The more viscous melt would lead

to higher nucleation activation energies and slower growth rates for crystalline phase formation during the solidification, and thus resulting in higher GFA.

(3) Multi-component alloy

The entire alloy systems developed for this research consisted of three elements, thus satisfying the third empirical rule of alloy design. This rule is often referred to as the 'confusion' principle. The increased complexity and size of the crystal unit cell reduces the energetic advantage of forming an ordered structure of longer-range periodicity than the atomic interactions.

5.1.1.2 The α-parameter criterion

Chapter 4 graphically and numerically presented the α-parameter values for the Mg-Cu-Y and Mg-Cu-Zn systems. The highest value of 1.77 was calculated for the ternary MCY1 alloy. In addition, the six remaining alloy studied in the Mg-Cu-Y system also displayed values equal to or above 1.5. In comparison, the ternary MCZ1 alloy attributed a value of 1.33.

It has been confirmed through experimental evidence that MCY1 and MCY3 contain an amorphous phase, and that the MCZ alloys are all fully crystalline. This would indicate that the α-parameter is suitable for predicting GFA in ternary compositions. However, this is somewhat disputable. Despite alloys MCY2, MCY4, MCY5, MCY6, and MCY7 displaying α-values in excess of 1.5 (the value stated in the literature over which good glass-formers are found), experimental results have suggested that the microstructures for these alloys are fully crystalline, indicating a weakness in the model's glass-forming predictability. It could be suggested that the critical α-value may be higher for Mg-based alloys (e.g. >1.7), since the XRD trace for the MCY1 alloy shows an amorphous peak, whereas MCY3 shows a mixture of crystalline and amorphous peaks, suggesting MCY3 has limited GFA. In addition, it should also be noted that liquidus temperature calculations are primarily required in order to calculate the α-parameter, which restricts its application to all possible alloys as this data is not always readily available without experimentation.

5.1.1.3 The elastic strain criterion

Chapter 4 numerically presented the mean local strain values for the Mg-Cu-Y and Mg-Cu-Zn systems. Ternary plots are also provided showing the theoretically determined glass-formation ranges. The elastic strain criterion states that the mean local strain must exceed 0.054 in order to destabilise the crystal lattice formation and encourage amorphisation.

It is evident that the elastic strain criterion is met ($\geq$0.054) for alloys MCY2 and MCY5. It appears that the elastic strain criterion for vitrification is met when the Y content is increased to approximately 23 atomic percent. However, experimental evidence indicates alloys MCY1 and MCY3 produced an amorphous phase despite the Y concentration being below the necessary limit to generate a sufficient amount of elastic strain. This suggests the elastic strain criterion is less dominant that the α-parameter as alloy MCY1 has a ε value <0.054 and yet yields good GFA.

It is also noticeable that all of the MCZ alloys (with the exception of MCZ6) meet the elastic strain criterion ($\geq$0.054). Since experimental evidence indicates that the MCZ alloys are fully crystalline, this suggests that the elastic strain modelling approach has limited accuracy in assessing glass-forming ability. This maybe because the assumptions used to calculate elastic strains are not applicable.

However, it should be noted that the elastic stain of alloy MCY1 is only slightly below the value required in order to destabilise the crystal lattice and encourage amorphisation. In addition, as highlighted in section 5.1.1.2, an α value of 1.77 was calculated for this particular alloy, suggesting high glass-forming ability. Thus, it can be concluded that the compositions with the highest glass-forming ability represent a balance between the two effects: proximity to a deep eutectic and maximisation of elastic strain. Therefore, by essentially substituting Y for Zn, Mg-rich metallic glass could not be produced as the balance between the two modelling approaches was too much in favour of the elastic strain criterion.

5.1.1.4 The λ_n criterion

The λ_n criterion has been defined to evaluate the concentration dependence of glass-forming ability. According to this criterion, an alloy with a λ_n value of approximately 0.18 has improved glass-forming ability. It is suggested that glass structures have optimum defect concentration when $\lambda_n \approx 0.18$.

The λ_n values for the MCY1 and MCY3 alloys are 0.19 and 0.17, respectively. These values suggest increased glass-forming ability, which has been verified by experimental results. In addition, the λ_n values for all of the MCZ alloys (determined experimentally to be crystalline) are significantly lower than 0.18. This provides strong evidence for the consideration of this criterion when predicting glass-forming ability. However, despite alloy MCY6 generating a λ_n value of 0.18, X-ray diffraction results suggests that this alloy is predominantly crystalline. This again suggests that importance of optimising multiple criteria to evaluate the glass-forming ability of particular alloy systems.

5.1.1.5 Electronegativity difference and atomic size parameter

It is evident that ΔT_x can be effectively used to indicate glass-forming ability for some bulk metallic glass systems. According to experimental data found within the literature, ΔT_x has a strong correlation with two bond parameters. In detail, ΔT_x increases with the increase of electronegativity difference (Δx) and the atomic size parameter (δ). Feng et al [4] developed the following equation, referred to as size-electronegativty merit, specifically designed for Mg-based bulk metallic glasses:

$$\frac{\Delta x^2}{0.54^2} + \frac{\delta^2}{0.23^2} = \geq 1$$

Figure 5.1 plots δ against Δx for a broad compositional range of Mg-Cu-Y ternary alloys. The MCY alloys used in this study can be identified by the red points. The calculated Δ values, based on size-electronegativity merit, for Mg-Cu-Y alloys with

ΔT_x greater than 50 K have also been plotted. This arc indicates a critical value used to determine 'bulk' or not for Mg-based bulk metallic glasses [4].

It is obvious that all of the Mg-Cu-Y alloys fall below the critical value used to determine good glass-forming ability. In addition, it is interesting that the alloys used in this study have values below the critical level indicating reduced glass-forming ability, despite experimental evidence of alloys MCY1 and MCY3 suggesting otherwise. However, it should be noted that the equation used to determine Δ, and thus the critical value used to determine 'bulk' or not, is based on alloys achieving a ΔT_x greater than 50 K. Since alloys MCY1 and MCY3 have ΔT_x values of 42 and 24, respectively, this may limit the applicability of this equation to these particular alloys.

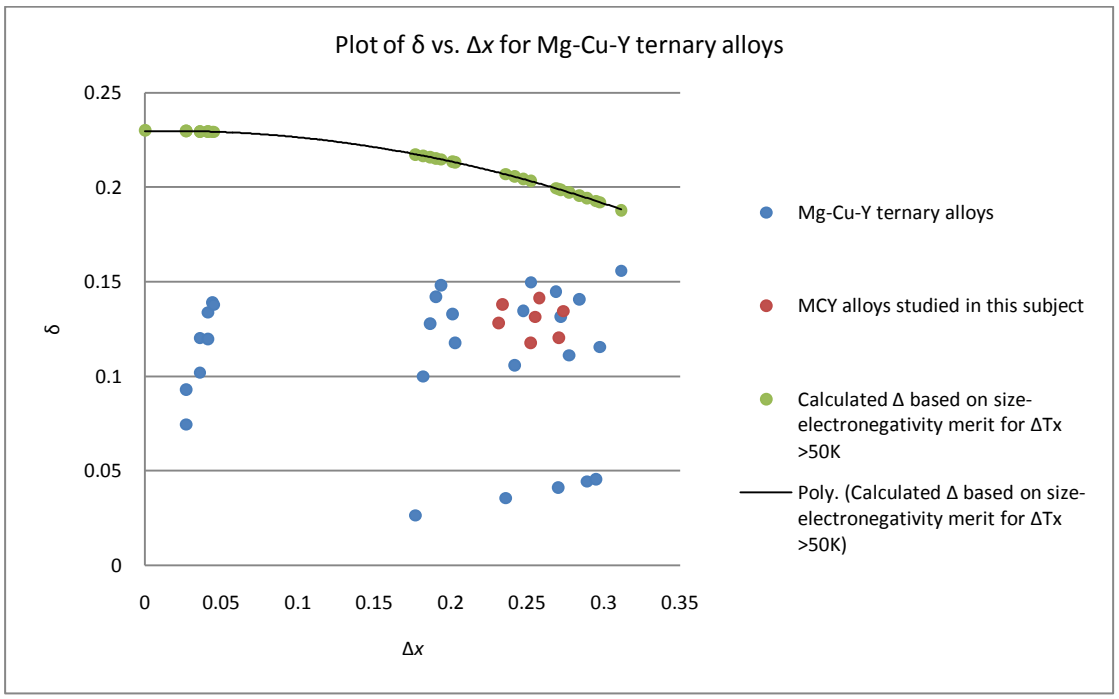

Figure 5.1 Plot of δ vs. Δ*x* for Mg-Cu-Y ternary alloys. The calculated Δ values, based on size-electronegativity merit, for Mg-Cu-Y alloys with ΔT_x greater than 50 K have also been plotted. The arc indicates a critical value used to determine 'bulk' or not for Mg-BMGs [4].

Figure 5.2 plots δ against Δ*x* for a broad compositional range of Mg-Cu-Zn ternary alloys. The MCZ alloys used in this study can be identified by the red points. The calculated Δ values, based on size-electronegativity merit, for Mg-Cu-Zn alloys with

ΔT_x greater than 50 K have also been plotted. This arc indicates a critical value used to determine 'bulk' or not for Mg-based bulk metallic glasses [4].

It is apparent that some of the Mg-Cu-Zn alloys lie above the critical value used to determine good glass-forming ability. It is also observable that the MCZ alloys studied in this research have values below the critical level indicating reduced glass-forming ability, which is supported with experimental evidence. This contradicts the earlier conclusions drawn regarding the limited application of this equation. However, the literature does suggest that the relative contributions of electronegativity difference and the atomic size parameter on the glass-forming ability are overtly different in different bulk metallic glass systems [4].

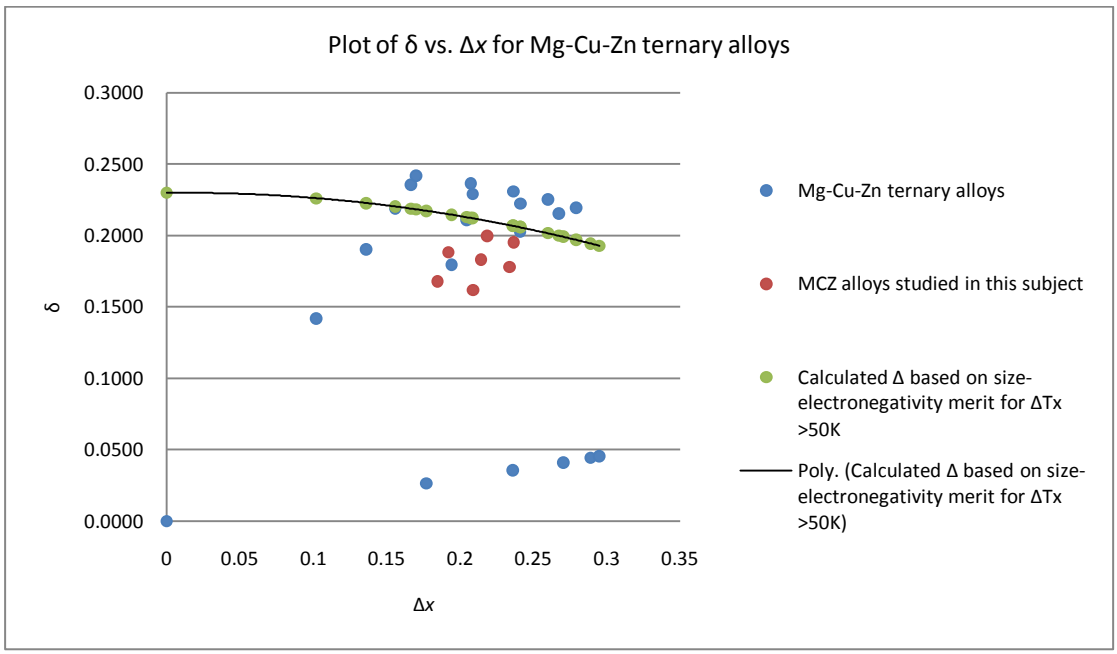

Figure 5.2 Plot of δ vs. Δ*x* for Mg-Cu-Zn ternary alloys. The calculated Δ values, based on size-electronegativity merit, for Mg-Cu-Zn alloys with ΔT_x greater than 50 K have also been plotted. The arc indicates a critical value used to determine 'bulk' or not for Mg-BMGs [4].

After learning there are some discrepancies with regards to the effect of electronegativty difference and atomic size parameter on glass-forming ability, further research was performed to clarify their reliability.

5.1.2 Thermal properties

The DSC traces of rapidly solidified alloys MCY1 and MCY3 compared to MCZ1 illustrate the significant effect of substituting Y with Zn on the thermal behaviour. It is apparent that the MCY alloys display exothermic reactions caused by crystallisation during continuous heating, typical of amorphous alloys. In contrast, the DSC trace for the MCZ1 alloy displays no exothermic reactions indicating a fully crystalline microstructure.

The verification of an amorphous phase present in the microstructure of alloys MCY1 and MCY3 was confirmed by thermal analysis. The GFA of an alloy has been associated with two simple parameters termed as the reduced glass-transition temperature, T_{rg}, and γ. According to previous literature, bulk metallic glasses are often reported when T_{rg} exceeds 0.6 and γ exceeds 0.41. The T_{rg} and γ values of alloys MCY1 and MCY3 were calculated to be 0.54 and 0.53, and 0.39 and 0.37, respectively. From these figures, it can be concluded that the values are very close to the critical values required for BMG formation. For comparison, Table 5.3 displays a list of amorphous Mg-based alloys published in the literature. It is evident that some Mg-based alloys form glass despite failing to achieve values for the T_{rg} and γ parameters in excess of the proposed figures.

Composition	T_{rg}	γ	D_{max} (mm)	Ref
$Mg_{58.5}Cu_{30.5}Y_6Gd_5$	0.59	0.42	7	[5]
$Mg_{65}Cu_{25}Sm_{10}$	0.59	0.41	5	[6]
$Mg_{65}Cu_{25}Y_{10}$	0.54	0.40	4	[7]
$Mg_{65}Cu_{25}Gd_{10}$	0.57	0.42	8	[7]
$Mg_{65}Cu_{25}Ho_{10}$	0.57	0.41	1	[7]
$Mg_{75}Ni_{15}Nd_{10}$	0.56	0.38	2.8	[7]

Table 5.3 Examples of T_{rg} and γ values for Mg-based amorphous alloys published in the literature.

In addition to the simple parameters discussed above, the ΔT_x value is also used as a measure of the GFA of alloys on the basis that a large ΔT_x value indicates a relatively

stable glass. However, the current results demonstrate that although the ΔT_x value of MCY1 is increased by 20 K compared with MCY3, the latter clearly shows evidence of an amorphous phase. In other words, it is not necessarily appropriate to judge the GFA by simple looking at the width of the supercooled liquid region in the calorimetric signal. The XRD results support this statement as the corresponding XRD trace suggests that alloy MCY3 is partially amorphous, despite the T_{rg} and α-values indicating that this alloy has inferior GFA compared to alloy MCY1. In addition, it should be noted that increased ΔT_x values do not always provide a good indication of improved GFA. [8]. Inoue et al. concluded that there is no direct correlation between ΔT_x and maximum sample thickness for ternary glassy alloys.

5.1.2.1 Enthalpy of crystallisation

The total enthalpy of crystallisation, ΔH_x, was obtained by integrating the areas under all exothermic peaks. The effect of substituting Y with Zn cannot be examined in relation to the enthalpy of crystallisation as no exothermic events were recorded for the MCZ1 alloy. However, when comparing the MCY1 and MCY3 alloys, the total enthalpy of crystallisation increased with greater Y content. The reduced enthalpy of crystallisation in MCY3 is due to only partial amorphous regions being present in the microstructure compared to the MCY1 alloy. This suggests that the MCY1 alloy has superior glass-forming ability compared to the MCY3 alloy, which has been verified by experimental results.

5.1.3 Mechanical properties

5.1.3.1 Hardness

The hardness values for all the rapidly solidified alloys are graphically presented in Chapter 4. It is obvious that the substitution of Y with Zn dramatically reduces the hardness values of the ternary alloys. With the exception of MCY6, all of the MCY alloys have higher hardness values compared to the MCZ alloys. Interestingly, MCY1 displays the highest average hardness of all the rapidly solidified alloys. This may be a direct result of the amorphous phase present within the alloy's microstructure.

Atomic bonds in the metallic glass can be broken and reform easily compared to covalent or ionic solids due to the rigidity of angles or balance of charges in the latter two respectively. Compared to dislocation movement in crystalline solids, rearrangement of atoms in the metallic glass is a high-energy and hence high-stress process. This is reflected by their high hardness compared to their crystalline counterparts. The exact nature of this atomic rearrangement process is still not fully understood. Nevertheless, there is a general consensus that deformation proceeds via local rearrangement of atoms to accommodate applied strain. However, how does one explain the difference in hardness between the MCY1 and MCY3 alloys? One would expect the hardness values for the MCY3 alloy to be equally as hard, although this is not evident. If both alloys have a fully amorphous phase, the difference in hardness between them may be attributed to the difference in chemical composition. More likely, the difference in hardness may be attributed to a lower amount of amorphous phase present in the microstructure of alloy MCY3 compared to alloy MCY1, as indicated by XRD results.

5.2 The effect of substituting Cu with Sm

The Mg-Cu-Zn system was investigated as it offers a cheaper alternative to the highly researched Mg-Cu-Y system, whilst maintaining optimised values for both α and ε. In parallel, innovative research into the Mg-Zn-Sm system was performed after it was discovered that this system also has low ternary eutectic temperature. This enables direct comparisons to be drawn regarding the effect of substituting Cu with Sm.

5.2.1 Predicting GFA

5.2.1.1 Empirical rules

According to early methodology for alloy design created by Inoue [1], in order to achieve high GFA for metallic alloys, the following three empirical rules should be satisfied: (1) have a negative mixing enthalpy among constituent elements, (2) contain large atomic size mismatches, and (3) be a multi-component alloy of three or more elements.

(1) Negative mixing enthalpy

The enthalpies of mixing among the major elements at the equiatomic composition, which is an important factor influencing on GFA and stability of the supercooled liquid region, for the Mg-Cu-Zn and Mg-Zn-Sm systems, have been calculated with Miedema's semi-empirical method. According to the calculated values displayed in Table 5.4, negative heats of mixing occur between all elements within these systems, thus satisfying the first empirical rule. However, the enthalpies of mixing values among Sm and the other elements present in these systems could not be found. Therefore, it cannot be said categorically that negative mixing enthalpies exist among all constituent elements present in these two systems.

	Cu	Mg	Sm	Zn
Cu	-	-20	*	-16
Mg	-20	-	*	-13
Sm	*	*	-	N/A
Zn	-16	-13	N/A	-

Table 5.4 The enthalpies of mixing among the elements present in the Mg-Cu-Y and Mg-Cu-Zn ternary systems. *Data not available.

(2) Atomic size mismatches

Inoue et al deduced experimentally, in order to achieve high GFA, metallic alloys must contain atomic size mismatches with optimised ratios of between 12 and 21 % [2]. As discussed in section 5.1.1.1 of this report, large atomic size differences often results in a dramatic increase in the viscosity of the melt, thus leading to higher glass-forming ability. The differences in atomic size ratios between the solvent and the solute elements in the Mg-Cu-Zn and Mg-Zn-Sm alloys are presented in Table 5.5.

	Cu	Mg	Sm	Zn
Cu	-	20.1	*	-16
Mg	20.1	-	12.6	16.5
Sm	*	12.6	-	*
Zn	-16	16.5	N/A	-

Table 5.5 Atomic size differences (%) between the solvent and the solute elements in the Mg-Cu-Zn and Mg-Zn-Sm alloys. *Data not available.

It is obvious that the atomic radius mismatch between the solvent and solute elements is between 12 and 21 % in all circumstances. This suggests that providing the other empirical rules are satisfied, the Mg-Cu-Zn and Mg-Zn-Sm alloys should achieve high glass-forming ability. However, experimental findings suggest the contrary, which may indicate that these rules cannot be generalised to these particular systems.

(3) Multi-component alloy

The entire alloy systems developed for this research consisted of three elements, thus satisfying the third empirical rule of alloy design. See section 5.1.1.1.

5.2.1.2 The α-parameter criterion

Chapter 4 graphically and numerically presented the α-parameter values for the Mg-Cu-Zn system. However, the α values for the Mg-Zn-Sm system were not listed. This is because these values cannot be calculated without liquidus temperatures, which are not available from the ternary phase diagram. Therefore, the effect of substituting Cu with Sm cannot be examined in relation to the α-parameter.

5.2.1.3 The elastic strain criterion

Chapter 4 numerically presented the mean local strain values for the Mg-Cu-Zn and Mg-Zn-Sm systems. Ternary plots are also provided showing the theoretically determined glass-formation ranges. The elastic strain criterion states that the mean local strain must exceed 0.054 in order to destabilise the crystal lattice formation and encourage amorphisation.

As discussed in section 5.1.1.3, it is clear that all of the MCZ alloys (with the exception of MCZ6) meet the elastic strain criterion ($\geq$0.054), thus indicating good glass-forming ability. However, as previously concluded, since experimental evidence suggests reduced GFA, the reliability of the elastic strain criterion is somewhat incredulous.

Conversely, the elastic strain values for the MZS alloys fail to exceed 0.54 in all cases. Since the experimental results indicate that the MZS alloys are crystalline, this adds weight to the elastic strain modelling approach and suggests it has a degree of accuracy in assessing glass-forming ability.

5.2.1.4 The λ_n criterion

The λ_n criterion has been defined to evaluate the concentration dependence of glass-forming ability. According to this criterion, an alloy with a λ_n value of approximately 0.18 has improved glass-forming ability.

It was suggested in section 5.1.1.4 that the λ_n criterion provides some evidence for its applicability when assessing the glass-forming ability of particular alloy systems. However, it was largely concluded that the λ_n criterion should be used in conjunction with other predicting parameters as it was shown not to be entirely accurate when compared to the experimental findings of the MCZ alloys. However, it is apparent that the MZS alloys do not have λ_n values in the region of 0.18 (the approximate value required to encourage amorphisation), which would support experimental evidence since both x-ray and thermal analysis indicate that these alloys contain crystalline microstructures.

5.2.1.5 Electronegativity difference and atomic size parameter

It has become apparent that the accuracy in predicting glass-forming compositions of the criterion researched in this report cannot be fully guaranteed when applied independently to the Mg-Cu-Zn and Mg-Zn-Sm systems. However, experimental results indicate that a combination of predictive criteria is more precise. Therefore, efforts were made to explore recently developed criteria to try to uncover an accurate, sole predictor of glass-forming ability in relation to the Mg-Cu-Zn and Mg-Zn-Sm systems.

As previously mentioned, Inoue et al. [1] proposed two empirical rules for exploring multicomponent bulk metallic glasses with high glass-forming ability and large supercooled liquid region. Recently, Fang et al. [4] have suggested two simple parameters to account for these two factors in multi-component Mg-based systems, i.e. the electronegativity difference, Δx, and atomic size parameter, δ, defined in Chapter 3. Interestingly, these authors have demonstrated that there is a linear equation between these parameters and bulk metallic glass thermal stability. Therefore, this report aimed at determining to what extent these parameters can be

utilised to measure the glass-forming ability of the Mg-Cu-Zn and Mg-Zn-Sm systems.

Figure 5.2 (see section 5.1.1.5) and Figure 5.4 plots δ against Δx for a broad compositional range of Mg-Cu-Zn and Mg-Zn-Sm ternary alloys, respectively. The MCZ and MZS alloys used in this report can be identified by the red points. The calculated Δ values, based on size-electronegativity merit have also been plotted. This arc indicates a critical value used to determine 'bulk' or not for Mg-based bulk metallic glasses [4].

Section 5.1.1.6 of this report has previously documented the accuracy of these parameters in predicting glass-forming ability in relation to the MCZ alloys. It was concluded that Δx and δ parameters accurately predict glass-forming ability since the MCZ alloys display values below the critical level used to determine 'bulk' or not and the experimental findings support this statement.

Figure 5.4 provides additional support for the use of these parameters in predicting glass-forming compositions. It is apparent that none of the Mg-Zn-Sm alloys have values above the critical level. In addition, the MZS alloys studied in this research also have values the fall below the critical level indicating reduced glass-forming ability. Since the effect of substituting Cu with Sm was experimentally concluded to provide little or no improvement in the glass-forming ability of these alloys, this theoretical evidence suggests electronegativity difference and the atomic size parameter are useful predictive tools when seeking to design glass-forming compositions.

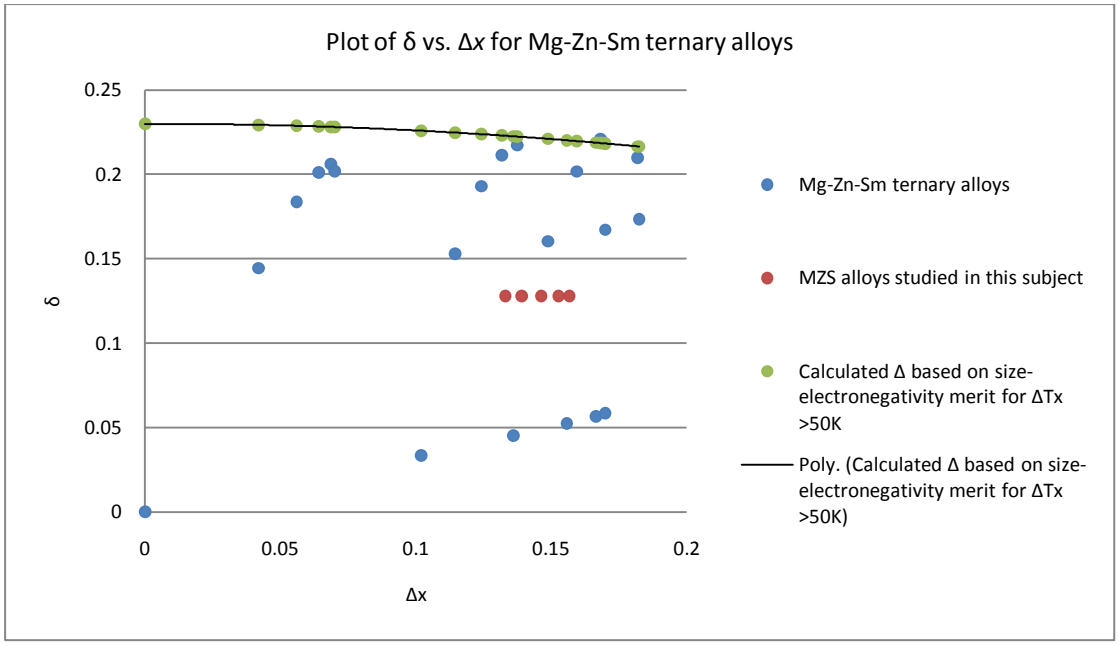

Figure 5.4 Plot of δ vs. Δ*x* for Mg-Zn-Sm ternary alloys. The calculated Δ values, based on size-electronegativity merit, for Mg-Zn-Sm alloys with ΔT_x greater than 50 K have also been plotted. The arc indicates a critical value used to determine 'bulk' or not for Mg-BMGs [4].

5.2.2 Thermal properties

The DSC trace of the rapidly solidified MCZ1 alloy compared to the traces of the MZS alloys illustrate the modest effect of substituting Cu with Sm on the thermal behaviour. According to thermal analysis, it is evident that the substitution of Cu with Sm does not help to achieve the formation of an amorphous phase.

The trace of the ternary eutectic MCZ1 alloy displays a single peak at 455 °C corresponding to the simultaneous melting of all the phases present in the microstructure and, therefore, indicates that this alloy is close to the ternary eutectic composition. In contrast, the trace of the ternary eutectic MZS1 alloy displays two endothermic peaks, which suggests this alloy is off-eutectic.

Other observations also conclude that the effect of substituting Cu with Sm on melting temperature is negligible. This may be attributed to the fact that the melting points of elemental Cu and Sm are remarkably similar (see Chapter 3, Table 3.3).

5.2.3 Mechanical properties

5.2.3.1 Hardness

The hardness values for all the rapidly solidified alloys are graphically presented in Chapter 4. It is noticeable that the substitution of Cu with Sm has little effect on the hardness values of the ternary alloys. Interestingly, all the MCZ and MZS alloys exhibit enhanced hardness values in comparison to the commercial wrought Mg-based alloy. It is suggested that the high hardness values may be attributed to a combination of refined microstructure and hard intermetallic phases.

References

[1] A. Inoue, in "Non-equilibrium Processing of Materials", ed. by C. Suryanarayana, Pergamon, 1999, p377

[2] A. Inoue, C. Fan, and T. Masumoto, Mater. Trans., JIM, 36(1995)1411

[3] Johnson, W. L., MRS Bull, 24(1999)42

[4] S. Fang, X. Xiao, L. Xia, Q. Wang, W. Li, and Y. Dong, Intermatallics, 12(2004)1069-1072

[5] J. Soubeyroux, S. Puech, and J. Blandin, Materials Science and Engineering A, 449(2007)253

[6] X. K. Xi, D. Q. Zhao, M. X. Pan, and W. H. Hang, Intermetallics, 13(2005)638

[7] Z. P. Lu, H. Bei, and C. T. Liu, Intermetallics, 15(2007)618

[8] A. Inoue, W. Zhang, T. Zhang, and K. Kurosaka, Journal of Non-Crystalline Solids, 304(2002)200

CHAPTER 6 – CONCLUSIONS AND FUTURE WORK

6.1 Conclusions

This research has proposed and evaluated both theoretically and experimentally, five criteria to assist in the design and development of new Mg-based systems. The criteria combine the effects of atomic or covalent ratios, the relative depth of a eutectic, concentration dependence, reduced melting temperatures and electronegativity mismatches. These criteria were utilised to evaluate the glass-forming ability, thermal stability and mechanical properties for Mg-based alloys. The findings of this research can be summarised as the following:

1. Of the rapidly solidified alloys, $Mg_{60}Cu_{22}Y_{18}$ (MCY1) is considered to have the best glass-forming ability. This is confirmed through SEM microscopy, thermal and XRD analysis

2. The α-parameter, which is an indicator of the relative depth of a eutectic composition (or at least the relative deviation of a calculated liquidus temperature form the temperature of an ideal solution), cannot be relied upon to predict compositions with good glass-forming ability in Mg-based systems. Despite some alloys displaying values in excess of 1.5 (the value stated in the literature over which good glass-formers are found), experimental results have suggested that the microstructures for these alloys are fully crystalline, indicating a weakness in the model's glass-forming predictability. Alternatively, it could be suggested that value of the α-parameter depends on the alloy system.

3. The elastic strain criterion cannot accurately predict glass-forming ability in Mg-based alloys. Experimental evidence indicates alloys MCY1 and MCY3 produced an amorphous phase despite the Y concentration being below the necessary limit to generate a sufficient amount of elastic strain.

4. The λ_n criterion can be used to successfully design glass-forming Mg-based compositions. The λ_n values for the MCY1 and MCY3 alloys are 0.19 and 0.17, respectively. These values suggest increased glass-forming ability, which has been verified by experimental results. In addition, the λ_n values for all of the MCZ and MZS alloys (determined experimentally to be crystalline) significantly fluctuate away from the optimum 0.18. This provides strong evidence for the consideration of this criterion when predicting glass-forming ability.

5. The cooling rate provided by the water-cooled Cu mould was insufficient to allow full vitrification of any composition. Despite an amorphous phase being present in the microstructures of alloys MCY1 and MCY3, SEM microscopy indicates the presence of small crystals

6. The hardness properties of the ternary crystalline MCY, MCZ and MZS alloys exceed those of wrought Mg alloys indicating a possibility for subsequent development of crystallised glassy alloys, which can be used for a wide range of applications.

6.2 Future work

1. It was concluded that the cooling rate provided by the water-cooled Cu mould was insufficient to allow full vitrification of any composition. If the temperature of the melt can be measured with reasonable accuracy then research into different melt temperatures during the rapid solidification process may provide a clearer understanding of glass-forming ability in Mg-based systems

2. This research has shown that rapid solidification of particular compositions in the ternary MCY system can result in the achievement of an amorphous phase. It would be interesting to see if increasing the complexity of one of the ternary MCY alloys, through adding additional elements, could enable full vitrification on rapid solidification.